University of Alberta

Simplified Modeling of the Human Spine

By

Mónika Elizabeth Toro Serrano ©

A thesis submitted to the Faculty of Graduate Studies and Research in partial fulfillment of the requirement for the degree of Master of Science

Department of Mechanical Engineering

Edmonton, Alberta

Spring 2002

National Library of Canada
Acquisitions and Bibliographic Services
395 Wellington Street
Ottawa ON K1A 0N4
Canada

Bibliothèque nationale du Canada
Acquisitions et services bibliographiques
395, rue Wellington
Ottawa ON K1A 0N4
Canada

Your file Votre référence

Our file Notre référence

The author has granted a non-exclusive licence allowing the National Library of Canada to reproduce, loan, distribute or sell copies of this thesis in microform, paper or electronic formats.

The author retains ownership of the copyright in this thesis. Neither the thesis nor substantial extracts from it may be printed or otherwise reproduced without the author's permission.

L'auteur a accordé une licence non exclusive permettant à la Bibliothèque nationale du Canada de reproduire, prêter, distribuer ou vendre des copies de cette thèse sous la forme de microfiche/film, de reproduction sur papier ou sur format électronique.

L'auteur conserve la propriété du droit d'auteur qui protège cette thèse. Ni la thèse ni des extraits substantiels de celle-ci ne doivent être imprimés ou autrement reproduits sans son autorisation.

0-612-69771-1

Canada

University of Alberta

Library Release Form

Name of Author: **Mónika Elizabeth Toro Serrano**

Title of Thesis: **Simplified Modeling of the Human Spine**

Degree: **Master of Science**

Year this Degree Granted: **2002**

Permission is hereby granted to the University of Alberta Library to reproduce single copies of this thesis and to lend or sell such copies for private, scholarly or scientific research purposes only.

The author reserves all other publication and other rights in association with the copyright in the thesis, and except as herein before provided, neither the thesis nor any substantial portion thereof may be printed or otherwise reproduced in any material form whatever without the author's prior written permission.

Mónika Toro S

Mónika Toro Serrano
3108 –47 Grier Place NE
Calgary, Alberta
T2k 5Y5

Date: 28 - January - 2002

University of Alberta

Faculty of Graduate Studies and Research

The undersigned certify that they have read, and recommend to the Faculty of Graduate Studies and Research for acceptance, a thesis entitled **Simplified Modeling of the Human Spine** submitted by **Mónika Elizabeth Toro Serrano** in partial fulfillment of the requirement for the degree of **Master of Science.**

Dr. Ken Fyfe (Supervisor)

Dr. Walied Moussa

Dr. Terry Hrudey

Date: 25 JAN 2002

Dedication

To

God, Toro Serrano Family and Ahmed El Abasiry

Abstract

Scoliosis is an abnormal curvature of the spine in the frontal plane associated with vertebral rotation. An understanding of the mechanical behavior of the human's spine is important to study the development and the corrections related with scoliosis. Using computer simulation and physical models of scoliotic spines, it is possible to create a pre-surgical tool. This tool would be able to predict the forces and moments that are necessary to apply during the surgery to obtain the correction.

The Finite Element Method was the mathematical tool employed in the present work. It employed a new technique called constraint equations. Constraint equations are linear equations that relate the degrees of freedom of a rigid body. The constraint equations minimized the global number of degrees of freedom in a system and greatly simplify the geometry of the model as well as the computational time. The technique also kept accuracy of the results for any number of degrees of freedom.

The present work employed experimental and computational displacement results to validate the modeling of the thoracic region of the human spine. Maximum displacements of the two-dimensional computational and experimental models were also compared, and the maximum percentage difference was 13%.

Acknowledgment

The author would like to express her deep gratitude to her supervisors Dr. Ken Fyfe and Mr. Jim Raso for their continues help and support in the course of this thesis.

Contents

Chapter 1 ..... **1**

1.1 Introduction **1**

1.1.1 Thesis Outline 2

1.2 Human Spine **2**

1.3 Components of the Spine **6**

1.3.1 Vertebra 6

1.3.2 Intervertebral Disc 7

1.3.3 Ligaments 8

1.3.3.1 Ligamentum Flavum 8

1.3.3.2 Transverse Ligament 9

1.3.3.3 Posterior and Anterior Ligaments 9

1.3.3.4 Supraspinous and Interspinous Ligaments 9

1.3.3.5 Facet Capsular Ligament 9

1.3.4 Tendons 10

1.3.5 Muscles 10

1.4 Geometry of the Human Normal Spine **11**

1.4.1 The Vertebra 11

1.4.2 Intervertebral Disc 13

1.5 Biomechanical Properties of the Human Normal Spine **13**

1.5.1 Properties of the Vertebra 13

1.5.2 Intervertebral Disc Properties 15

1.5.3 Ligaments and Tendons 18

1.5.4 Summary 20

1.6 Idiopathic Scoliosis **21**

1.6.1 Treatments of Scoliosis 23

1.6.1.1 Observation Treatment 24
1.6.1.2 Orthotic Treatment 24
1.6.1.3 Surgical Treatment 25
1.6.2 Complications of Surgical Treatments 26

1.7 Development of a Pre-surgical Tool 27

Chapter 2 28

2.1 Literature Review 28
2.1.1 Shultz A., Galante J. 28
2.1.2 Subbaraj K., Ghista D. N., Viviani G. R., ... 29
2.1.3 Dietrich, M. Kedzior K., Zagrajek T. 30
2.1.4 Steven Tong 31
2.1.5 Schultz, A. 32
2.1.6 Takemura, Yamoto and Tani T. 33

Chapter 3 34

3.1 Finite Element Method 34

3.2 Kinematics of Rigid Body Motion 34

3.3 Constraint Equations 36
3.3.1 Constraint Equations in Two Dimensions 36

3.4 Constraint Equations - Procedures 40
3.4.1 Collocation Overdetermination 41
3.4.2 Trial Solution Method 42

3.5 Geometrical Non-linearity 42
3.5.1 Frame with Horizontal Force 44
3.5.2 Frame with Horizontal and Vertical Force 46
3.5.3 Series of Blocks 48

3.6 ANSYS Elements and Constraint Equations 51

3.7 Meshing 52

Chapter 4 54

4.1 Spine Simulation 54

4.2 Probable Error 55

4.3 Experimental Model 57

4.3.1 Shear Test 59

4.3.2 Compression Test 63

4.3.3 Student T Test for Sample Means 68

4.3.4 Intervertebral Disc vs. Silicone Disk Material Properties 69

4.3.5 The Physical Functional Unit 70

4.3.6 Physical Model 72

4.4 Computational Model 77

4.4.1 Modeling of the Intervertebral Disc 77

4.4.2 Computer Model of the Physical Functional Unit 81

4.4.3 Computational Physical Model 85

4.4.4 Discussion 89

4.4.5 Thoracic Model 92

Chapter 5 97

5.1 Summary 97

5.2 Conclusions 100

5.3 Future Work 102

6.1 References 104

Appendix 1 ..... **110**
Nomenclature of the geometry of the vertebrae 110

Appendix 2 ..... **112**
Geometrical Analysis of Constraint Equations 112

Appendix 3 ..... **116**
Constraint Equations in Two dimensions with Rotations 116

Appendix 4 ..... **118**
Constraint Equations in Three dimensions with Rotations 118

Appendix 5 ..... **124**
Constraint Equations in Two dimensions with no rotations 124

Appendix 6 ..... **126**
Physical Functional Unit Displacements 126

Appendix 7 ..... **127**
Coordinate Measuring System Specifications 127

Appendix 8 ..... **128**
Physical Model Results 128

Appendix 9 ..... **132**
Computational Physical Functional Unit Results 132

Appendix 10 ..... **133**
Computational Results of Physical Model 133

List of Tables

Table 1-4-1-1 Flexion, extension, lateral flexion and axial rotation ranges 12
Table 1-5-1-1 Young's modulus of the vertebra (cortical bone) 14
Table 1-5-1-2 Average stiffness coefficients with forces of the vertebra 15
Table 1-5-1-3 Average stiffness coefficients with moments of the vertebra 15
Table 1-5-2-1 Young's modulus of the intervertebral disc 18
Table 1-5-2-2 Stiffness due to forces of the intervertebral disc 18
Table 1-5-2-3 Stiffness due to moments of the intervertebral disc 18
Table 1-5-3-1 Young's modulus and Poison's ratio of the ligaments 19
Table 1-5-3-2 Young's modulus and stiffness of each spinal ligament 20
Table 1-6-1-1 Treatment of scoliosis 23
Table 3-3-1-1 Final position in X, Y and Z coordinates of the selected point 38
Table 3-5-1 Results from linear and non-linear test of the cantilever beam 44
Table 3-5-1-1 Results from beam and CE frame models with horizontal force 46
Table 3-5-2-1 Results from beam and CE models with horizontal and vertical force. 47
Table 3-5-3-1 Results from beam and CE series model with one end fixed 50
Table 4-2-1 Probable error 56
Table 4-3-1-1 Stiffness and shear modulus of silicone 732 63
Table 4-3-2-1 Stiffness and compression Young's modulus of silicone 732 68
Table 4-3-3-1 Student T test for sample mean results 69
Table 4-3-4-1 Material properties of the intervertebral disc and silicone disk 70
Table 4-3-5-1 Thickness values of the physical functional unit 71
Table 4-4-1-1 Comparison between different models using CE, springs and plane element 81
Table 4-4-3-1 Percentage difference of the physical model 89
Table 1-1 Geometry of the Vertebra 111
Table 6.1 Experimental results from the physical functional unit 126
Table 8.1 Horizontal Forces in block 7 and 3 of the Physical Model 129
Table 8.2 Horizontal Force in block 7 of the Physical Model 129
Table 8.3 Horizontal Force in block 3 of the Physical Model 129
Table 8.4 Horizontal Force in block 4 of the Physical Model 130
Table 8.5 Horizontal Force in block 4 and angle force at block 7 of the Physical Model 130

Table 8.6 Angle Force of 4 degrees at block 7 of the Physical Model 130
Table 8.7 Moment at block 3 of the Physical Model 131
Table 8.8 Moment at block 7 of the Physical Model 131
Table 8.9 Vertical angle of 4 degrees at block 3 and Horizontal force at block 7 of the Physical Model 131
Table 9.1 Computational results from the physical functional unit 132
Table 10.1 Horizontal Forces in block 7 and 3 of the Computational Model 133
Table 10.2 Horizontal Force in block 7 of the Computational Model 133
Table 10.3 Horizontal Force in block 3 of the Computational Model 133
Table 10.4 Horizontal Force in block 4 of the Computational Model 134
Table 10.5 Horizontal Force in block 4 and angle force at block 7 of the Computational Model 134
Table 10.6 Angle Force of 4 degrees at block 7 of the Computational Model 134
Table 10.7 Moment at block 3 of the Computational Model 135
Table 10.8 Moment at block 7 of the Computational Model 135
Table 10.9 Vertical angle of 4 degrees at block 3 and Horizontal force at block 7 of the Computational Model 135

List of Figures

Figure 1-2-1 Regions of the human spine, sagittal view 3
Figure 1-2-2 Conventional planes and axis 4
Figure 1-2-3 XYZ spine axes 5
Figure 1-2-4 Local coordinates of the vertebra 5
Figure 1-3-1-1 Typical lumbar vertebra 6
Figure 1-3-2-1 Intervertebral disc 7
Figure 1-3-3-1 Ligaments of the spine 8
Figure 1-3-4-1 Typical Stress-strain graph of tendons behavior 10
Figure 1-5-2-1 Tensile and compressive stresses in the intervertebral disc 16
Figure 1-5-2-2 Bending of the spine 16
Figure 1-5-2-3 Horizontal and axial shear stresses in the intervertebral disc 17
Figure 1-5-2-4 Axial rotation between the vertebrae in the spine 17
Figure 1-6-1 Types of scoliosis, classification King Moe 21
Figure 1-6-1-1 Cobb's angle 23
Figure 3-3-1-1 Incremental angle values 38
Figure 3-5-1-1a Model with beam elements with horizontal force 45
Figure 3-5-1-1b CE frame model with horizontal force 46
Figure 3-5-2-1a Model with beam elements with horizontal and vertical force 47
Figure 3-5-2-1b CE model with horizontal and vertical force 47
Figure 3-5-3-1a Beam series model 49
Figure 3-5-3-1b CE series model 49
Figure 4-3-1 Stress-strain silicone DC 999 (from ASTM STP 1271,1996) 58
Figure 4-3-1-2a Stress-strain shear curve of silicone 732 cured 1 week 60
Figure 4-3-1-2b Stress-strain shear curve of silicone 732 cured 7 weeks 60
Figure 4-3-1-3 Hysterisis results for the shear test of silicone 732 61
Figure 4-3-1-4a Load-displacement shear curve of silicone 732 cured 1 week 62
Figure 4-3-1-4b Load-displacement shear curve of silicone 732 cured 7 weeks 62
Figure 4-3-2-1 Compression set up 64
Figure 4-3-2-2a Stress-strain compression curve of silicone 732 cured 1 week 65
Figure 4-3-2-2b Stress-strain compression curve of silicone 732 cured 5 weeks 66
Figure 4-3-2-3b Load-displacement compression curve of silicone 732 cured 5 weeks 67

Figure 4-3-5-1 Dimensions of the physical functional unit 70
Figure 4-3-5-2 Bending force applied to the physical functional unit. 71
Figure 4-3-5-3 Equivalent forces of the physical functional unit 72
Figure 4-3-6-1 Coordinate Measuring Machine 73
Figure 4-3-6-2 Horizontal force applied to the physical model 75
Figure 4-3-6-3 Combined forces applied to the physical model 75
Figure 4-3-6-4 Moment applied to the physical model 76
Figure 4-4-1-1 Crossed spring set model 78
Figure 4-4-1-2 Intervertebral disc using plane elements 80
Figure 4-4-2-1 Displacement results from physical functional unit 1 83
Figure 4-4-2-2 Displacement results from physical functional unit 2 84
Figure 4-4-2-3 Displacement results from physical functional unit 3 84
Figure 4-4-3-1 X displacement of the physical model case Horizontal 4 86
Figure 4-4-3-3 X displacement of the physical model of case Moment 7. 88
Figure 4-4-3-4 Y displacement of the physical model of case Moment 7 88
Figure 4-4-4-1 Intervertebral disc using solid elements 91
Figure 4-4-4-2 Intervertebral disc using plane elements 91
Figure 4-4-4-3 Intervertebral disc using spring set 91
Figure 4-4-5-1 CE represented by lines that form the vertebral body 93
Figure 4-4-5-3 Intervertebral discs, ligaments and tendons 94
Figure 4-4-5-3 Thoracic model 95
Figure 4-1 Rotation sequences for X Coordinate 118
Figure 4-2 Rotation Sequences for Y Coordinate 119
Figure 4-3 Rotation Sequences for Z Coordinate 119
Figure 4-4 True and Approximate Rotation Matrix Results for X and Y Coordinate 120
Figure 4-5 True and Approximate Rotation Matrix Results for Z Coordinate 120

Chapter 1

1.1 Introduction

Scoliosis is a lateral curvature of the spine in the frontal plane. It probably constitutes one of the most challenging and complex clinical problems in the field of orthopedic biomechanics. There are several treatments to correct spinal deformation depending on the severity of the curvature. The operative treatment for scoliosis and spinal fixation has not yet been satisfactorily clarified. Therefore, developing a model to describe the corrective forces and methods prior to surgery is necessary.

The vertebral column is a non-homogenous complex structure with a mechanical behavior that is difficult to analyze. Presently, researchers use the Finite Element Method with numerous simplifications with regard to the geometry and to the material behavior of the spine. This research was done using the Finite Element Method that incorporates constraint equations. The constraint equations are a set of linear equations that relate the degrees of freedom of the points in a rigid body.

The present work pursued three objectives. The use of constraint equations to represent the motion of the rigid body, the experimental and computational maximum displacement results have a maximum percentage difference in the order of 15%. Finally, the intervertebral disc was modeled in two dimensions.

The final product of the thesis was the modeling, in two dimensions, of the thoracic region of the human spine. The computational model was subjected to different loading conditions in order to verify the accuracy and short computational time of the Finite Element Method. The software tools used to develop this model are ANSYS® and MATLAB®. A physical model of the spine is used to validate the results of this computational model.

1.1.1 Thesis Outline

The first chapter provides an introduction to the thesis, an overview of the relevant anatomy and biomechanical geometrical information of the human spine and an explanation of idiopathic scoliosis. This chapter also explains the treatments for scoliosis to realign the deformity and reduce the pain of the motion segments and as well as discusses the most common failures in the treatment.

Chapter Two presents the literature review used in this work. Chapter Three explains the finite element method and the selection of the elements used in the present work. The chapter also discusses the constraint equations approach that is used in the analysis.

The fourth chapter presents the modeling of the spine. The modeling can be categorized into two parts: the physical model built with wood and silicone and the computational model of the spine performed in ANSYS. A comparison between the displacement results obtained from the computational model and the experimental one is discussed.

Finally, the fifth chapter presents the discussion, conclusions, and recommendations for future work. A bibliography and the appendices follow this.

1.2 Human Spine

The human spine is considered a mechanical structure of the human body because it supports the trunk as well as, protects the spinal cord and neural elements. The vertebral column the axis of this mechanical structure, rests on the pelvis at the lower end and at the upper end, supports and orients the head in space.

The spine has three fundamental biomechanical functions. First, it transfers the loads and the resultant bending moments coming from the head and trunk as well as any weight being lifted towards the pelvis. Second, it provides a structure to join the extremities, head and trunk with enough physiological energy to cause motion. Finally,

and most importantly, it protects the delicate spinal cord from potential damaging forces and motions from physiologic movement or trauma [11,22,54].

According to Kapandji, (1987) the general anatomy of the spine is divided into five regions the cervical, the thoracic, the lumbar, the sacrum and coccyx. Each section is composed of individual bones called vertebra. There are seven cervical vertebrae (C1-C7), twelve thoracic vertebrae (T1-T12) and five lumbar vertebrae (L1-L5). All these are mobile vertebrae. Below the lumbar region is a bone called the sacrum, which is composed of five fused sacral vertebrae. Its function is to transmit body loads to the pelvis. The last region, the coccyx, is a bone attached to the sacrum and contains four fused coccygeal vertebrae. Figure 1-2-1 shows a drawing of the human spine.

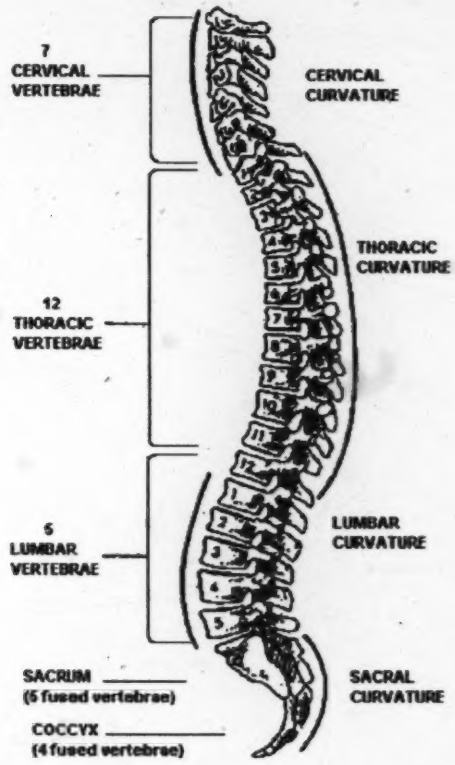

Figure 1-2-1 Regions of the human spine, sagittal view
(Modified from Zatsiorsky, 1998)

The spine in the sagittal view has four normal curves, cervical, thoracic (kyphosis), lumbar (lordosis) and sacral curvatures. These curves are convex anteriorly in the cervical and lumbar regions and convex posteriorly in the thoracic and sacral regions. The mechanical basis for the anatomic curves results from the curves increasing the flexibility while at the same time maintaining adequate stiffness and stability at the intervertebral joint level [22,51,54].

The conventional planes used in this study are: the frontal plane, transverse plane and sagittal plane with the correspondent axis as shown in Figure 1-2-2

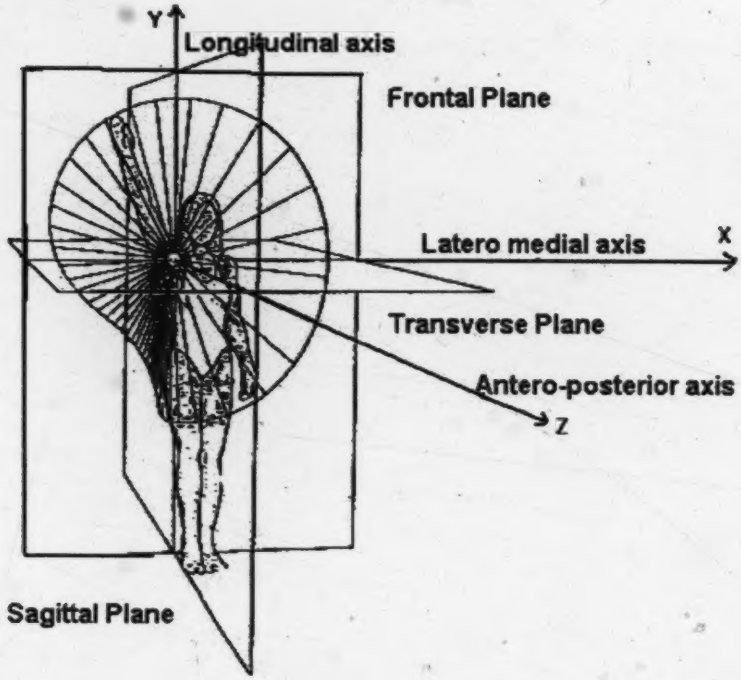

Figure 1-2-2 Conventional planes and axis
(Modified from Zatsiorsky, 1998)

The global coordinate system used in the present work is a XYZ right-handed system. The X-axis represents the Latero medial axis; the Y-axis represents the Longitudinal axis

and the Z-axis represents the Antero posterior axis. In similar way, the conventional planes are represented by the combination of the X, Y and Z-axes. See Figure 1-2-3. The local coordinate system of the vertebra is represented in Figure 1-2-4

Figure 1-2-3 XYZ spine axes
(Modified from Pope, et al., 1984)

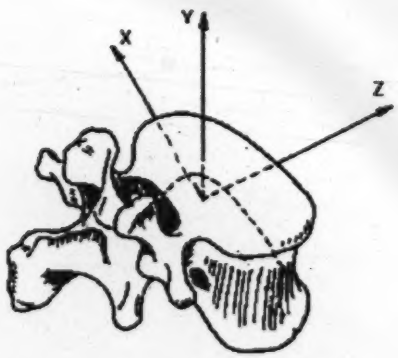

Figure 1-2-4 Local coordinates of the vertebra
(Modified from Pope, et al., 1984)

1.3 Components of the Spine

The primary components of the spine are: vertebrae, intervertebral discs, ligaments, tendons and muscles. Each of these elements plays an important role in the biomechanical behavior of the spine.

1.3.1 Vertebra

A typical vertebra consists of an anterior body and a neural or posterior arch. The arch bears seven processes: the spinous processes, two lateral transverse processes and four articular processes (two superior and two inferior) as shown in Figure 1-3-1-1.

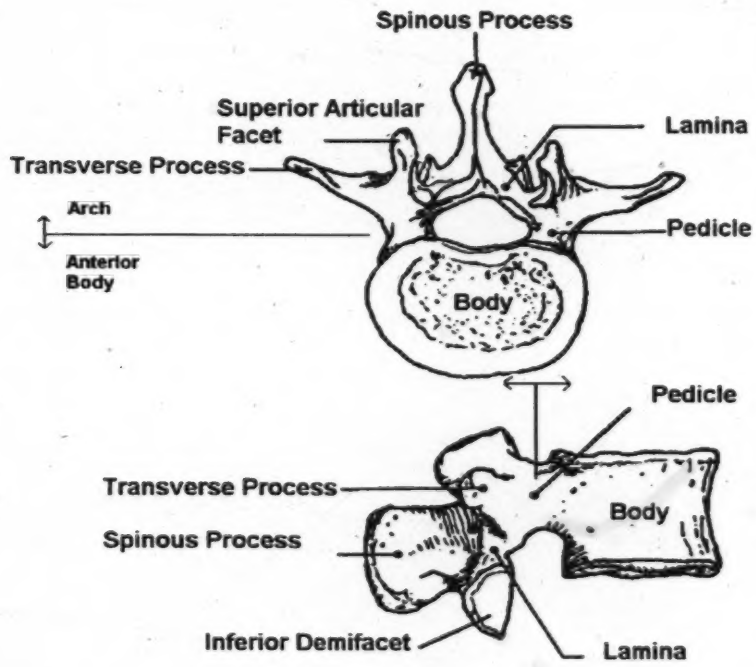

Figure 1-3-1-1 Typical lumbar vertebra
View from above (upper figure) and from right side (lower figure).
(Modified from Schultz, 1974)

The vertebral body is a kidney-shaped bone. The outer surface is a dense bony layer surrounded by a spongy marrowbone. The flat surface of the vertebral body is called an endplate. It is composed of hyaline cartilage. The posterior element of the vertebra is the vertebral arch and it is composed of the lamina and pedicle. A concavity and inferior vertebral notch on the inferior border of the arch provides a passageway for a spinal nerve.

The spinous process is a prominence at the posterior part of each vertebra. The paired transverse processes are oriented ninety degrees to the spinous processes and provide attachment for back muscles. There are four facet joints associated with each vertebra, one pair facing upward and the other facing downward [11,22,50,54].

1.3.2 Intervertebral Disc

The intervertebral disc is a fibro cartilage flattened disc between the bodies of vertebrae. It is subjected to different types of loads due to the physiologic motions such as flexion, extension and lateral bending. These loads are tension, compression, and torsion. Axial rotation of the trunk with respect to the pelvis causes torsional load that results in shear stresses in the lumbar discs. The Intervertebral disc consists of two parts. The first is the nucleus pulpous that is centrally located with a very loose mucoprotein gel, tightly bounded by fibrous tracks. Surrounding the nucleus pulpous is the annulus fibrous, which is a structure that contains fibrous in concentric laminated bands arranged in helicoidal manner [19,22,54]. Figure 1-3-2-1 shows the structure of the intervertebral disc.

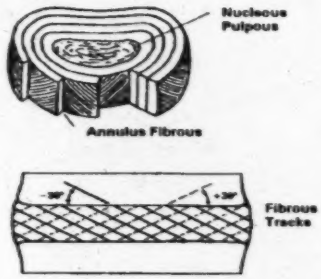

Figure 1-3-2-1 Intervertebral disc
(Modified from White and Panjabi, 1990)

1.3.3 Ligaments

Ligaments are elastic bands of strong fibrous connective tissue that attach the bones together and help stabilize the joint. There are seven ligaments attached to each vertebra as shown in Figure 1-3-3-1.

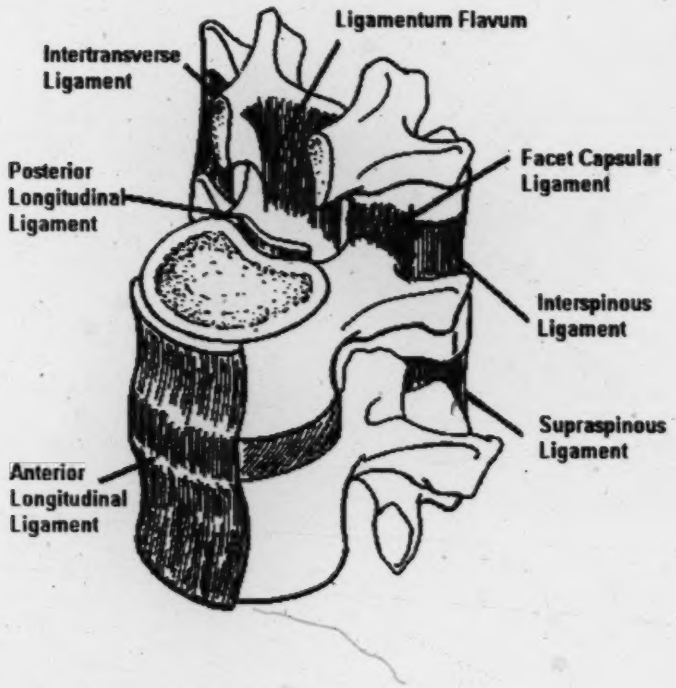

Figure 1-3-3-1 Ligaments of the spine
(Modified from White and Panjabi, 1990)

1.3.3.1 Ligamentum Flavum

Ligamentum flavum runs from the anterior and interior aspect of the lamina of the vertebra. There are a left and right ligamentum flavum that begin at the cervical vertebra C1 superiorly and end in the lumbar vertebra L5 inferiorly. The ligamentum flavum is the only one with elastin, an extra-cellular connective tissue protein. Elastin causes natural contraction; therefore in the case of the ligamentum flavum, its function is to prevent sagging into the spinal canal [19,22,51,54].

1.3.3.2 Transverse Ligament

The transverse ligaments connect the ends of the transverse processes of the vertebrae. The ligament consists of a thin membranous band that works during lateral flexion and at the same time leads to relaxation of the capsular ligaments. Relaxation occurs in viscoelastic elements when is applied a pre-stressed load and it tends to decreased gradually with the time [19,22,51,54].

1.3.3.3 Posterior and Anterior Ligaments

The posterior longitudinal ligament runs from the posterior aspect of the vertebral body from cervical vertebra C2 to the coccyx. It has a weak attachment to the vertebral body and a strong attachment to the intervertebral disc. The strong attachment helps to prevent intervertebral disc herniation and the weak attachment allows for the exit of the basi-vertebral veins.

The anterior longitudinal ligament is a wide fibrous band that covers the anterior aspect of the vertebra at the cervical level C1 to the sacrum. Contrary to the posterior longitudinal ligament, it has a rather strong attachment to the vertebral body but a rather weak attachment to the intervertebral disc. The function of the anterior longitudinal ligament is to limit the extension of the spine [19,22,51,54].

1.3.3.4 Supraspinous and Interspinous Ligaments

The supraspinous and interspinous ligaments run between the spinous processes from the cervical vertebra C2 to lumbar vertebra L5. The function of these ligaments is to limit the spinal flexion and control the rotation between neighboring vertebrae [19,22,51,54].

1.3.3.5 Facet Capsular Ligament

The facet capsular ligament is a heavy fibrous structure with a synovial (lubricant fluid) membrane that helps to minimize the friction among the facets and surrounding articulations. It controls the flexion and rotation between adjacent vertebrae. Another function of the capsules is to allow smooth and effortless motion between the facet

surfaces when axial compression or extension of the spine occurs. The facet joints also support a small portion of the compressive loads [14,19,22,51,54].

1.3.4 Tendons

The tendon is a composite material composed of connective fibrous protein and elastic tissue that attach the muscles with the bones. Tendons contain collagen fibers that give them mechanical properties, such as tensile strength, elasticity, viscosity, relaxation and creep. The mechanical response of these complex structures is non-linear and is characterized by J-shape dependence shown in Figure 1-3-4-1 [22,55].

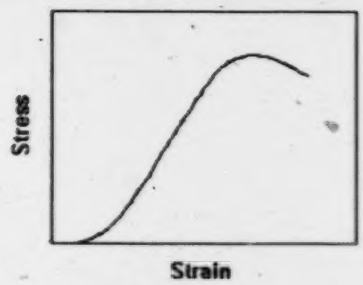

Figure 1-3-4-1 Typical Stress-strain graph of tendons behavior (J-shape dependence)

1.3.5 Muscles

The muscle is a wrapped package containing other smaller wrapped package of long, slender cells known as muscle fibers. Skeletal posterior muscles show sustained contraction when a person is awake and its action is essentially related to the extension of the lumbar vertical column. When the sacrum is fixed, the muscles powerfully extend the lumbar and thoracic column at the lumbrosacral joint (L5 and sacrum) and at the thoracolumbar joint (T12 and L1) respectively. In addition, the muscles accentuate the lumbar lordosis [22,51,54].

The functions of the back muscles are

- Extension of the vertebral column,

- Maintenance of the erect posture and head posture,
- Lateral bending,
- Stabilization of the vertebral column during flexion and
- Rotation

1.4 Geometry of the Human Normal Spine

The spinal column is like a tall radio tower made up of twenty four vertebrae, separated by the intervertebral discs that act as shock absorbers. The spine is unstable on its own, but due to the different elements attached to it such as ligaments, tendons and muscles it is very stable. In profile, the spine is curved in a faint S-shape to help to support different kinds of loading conditions. Therefore, the role of the tendons, muscles and ligaments in the human back is supporting the spine in its S-shape.

1.4.1 The Vertebra

The vertebra is composed of anterior and posterior elements [22]. The anterior element is the vertebral body and it plays the static role because it supports the whole structure. The posterior elements play the dynamic role because they allow the mobility of the vertebral column. The primary function of the vertebra is to support loads, including the body weight.

"As a whole the column from sacrum to skull is equivalent to a joint with three degrees of freedom: it allows flexion and extension, lateral flexion right and left and axial rotation. The range of these elementary movements at each individual joint of the column is very small but, in view of the many joints involved, the cumulative effect is quite significant". (Kapandji, 1987). The pattern of movements of the spine is dependent on the shape and positions of the articulating processes, the attached ligaments, thickness of the intervertebral discs and orientation of the facets.

Moving from top to the inferior position of the vertebrae (T1-S1) the range of motion of the individual motion segments increases in flexion and extension, but decreases in axial

rotation. In lateral flexion, the range of motion is almost constant. The motion segment or functional unit is considered to be two adjacent vertebrae and their interposed intervertebral discs of the spine; each segment has six degrees of freedom [57]. The lower vertebra is fixed while the upper one is subjected to different loading conditions.

As mentioned in Section 1.2, the spine has curves, and, therefore, the posterior elements are not oriented perfectly vertical. They are inclined. This causes more than one movement of the vertebrae at the same time, i.e., when lateral bending is performed the motion segment also rotates about its latero medial and longitudinal axis. As a result, the spinous processes in the upper portion of the thoracic region rotate to the convex side while the spinous processes of the lumbar region rotate toward the convexity of the spine. The following table summarizes the motion ranges in the different regions of the spine.

Movement	Region	Angle (Degrees)
Flexion	Lumbar	60
Extension	Lumbar	35
Flexion	Thoraco-lumbar	105
Extension	Thoraco-lumbar	60
Lateral Flexion	Lumbar	20
Lateral Flexion	Thoracic	20
Axial Rotation	Lumbar	5
Axial Rotation	Thoracic	35

Table 1-4-1-1 Flexion, extension, lateral flexion and axial rotation ranges (Kapandji, 1987)

The modeling of the vertebral column requires the dimensions of its components such as lengths, widths, and cross sections. In the literature, data is collected from different research sources. The geometry of the vertebra is shown in Appendix 1

1.4.2 Intervertebral Disc

The intervertebral disc is a combination of a center with fluid and an annulus with fibers that cause a different behavior according to the applied load. For instance, at low levels of load, the response is a soft or flexible disc. On the other hand when the load is large, approaching traumatic levels, the fluid in the core pressurized. The pressure makes the disc stiff or less flexible; therefore the intervertebral disc can become even stiffer than the vertebral bone [22,54].

The intervertebral disc thickness varies according to the region in the vertebral column. In the cervical region, it is 3 mm; in the thoracic region, it is 5 mm; and, in the lumbar region, it is 9 mm. These differences in thickness cause a different ratio of mobility. For instance, the cervical column is the most mobile, followed by the lumbar column and, finally, the thoracic column, which is the least mobile (Kapandji, 1987).

1.5 Biomechanical Properties of the Human Normal Spine

The human spine anatomically described is a set of vertebrae, intervertebral discs, ligaments, tendons and muscles. All these elements work together to transmit suitable loads towards the pelvis and keep the normal posture of a person. During normal activity, the spine can undergo flexion, extension, axial rotation and lateral bending. These movements subject the intervertebral discs, ligaments, tendons and muscles to a different set of loading conditions such as compression, tension, bending, torsion and shear.

1.5.1 Properties of the Vertebra

The vertebra is composed of a cortical shell, cancellous core, end plate, facet joints and neural arch. The vertebra may be considered as an engineering structure composed of a vertical column joining the two end plates and horizontal ties supporting the columns from the side. This structure can support compressive and shear loads [27,54].

The major physiological load on the column is axial, producing compression on each vertebra. The vertebral body carries most of the compressive load helped by the facets. An axial load produces compression on the vertebrae. This causes significant pressure on the nucleus. The compressive load is almost entirely transferred directly from one vertebra to the other by the annulus of the intervertebral disc. A small percentage of the compressive load is carried by the endplate. The failure of the vertebra is due to the fracture of the periphery of the endplate [54].

In the literature, the reported mechanical properties of the vertebra differ from one author to another. In this study the most representative results were used. The value used in the modeling corresponded to the mean value of the values found in literature shown in Table 1-5-1-1. Other important mechanical properties were found from Goel and Weinstein (1990), such as the tensile strength with a value of 1.18 N/mm^2, the compressive strength from 1.37 to 1.86 N/mm^2 and the shear modulus as 4,615 N/mm^2.

The consecutive tables, Table 1-5-1-2 and Table 1-5-1-3, contain the average stiffness coefficients of a representative functional spinal unit in different regions of the spine.

Author	Young's Modulus (N/mm^2)	Poison's Ratio
Goel and Weinstain, 1990	12000	0.3
White and Panjabi, 1990	8900 (Longitudinal)	0.3
White and Panjabi, 1990	4300 (Tangential)	0.3
White and Panjabi, 1990	3800 (Radial)	0.3
Suwito, et al., 1992	14500	0.3
Skalli, et al., 1993	12000	0.3
Yoganandan, et al., 1995	10000	0.39

Table 1-5-1-1 Young's modulus of the vertebra (cortical bone) (Different sources)

Region	Tension +Fy (N/mm)	Compression -Fy (N/mm)	Ant. Shear +Fz (N/mm)	Post. Shear -Fz (N/mm)	Lat. Shear Fx (N/mm)
Thoracic	770	1250	110	110	110
Lumbar	770	2000	121	170	145

Table 1-5-1-2 Average stiffness coefficients with forces of the vertebra (White and Panjabi, 1990)

Region	Flexion +Mx (Nmm/deg)	Extension -Mx (Nmm/deg)	Lat. Bend +Mz (Nmm/deg)	Axial Rotation -My (Nmm/deg)
Thoracic	770000	1250000	110000	110000
Lumbar	770000	2000000	121000	170000

Table 1-5-1-3 Average stiffness coefficients with moments of the vertebra (White and Panjabi, 1990)

1.5.2 Intervertebral Disc Properties

The intervertebral disc can resist forces and moments in many directions because of its structure. Along with the facet joints, it is responsible for carrying all the compressive loading to which the trunk is subjected. The compressive load is transferred from one vertebral end plate to the other by the nucleus pulposus and the annulus fibrous, creating internal pressure.

The fibers (annulus fibrosus) at ± 30 degrees arrangement absorb the tensile stresses. The situation is quite different when the nucleus is dry, because the nucleus is not capable of building sufficient fluid pressure and the loads are distributed more around its periphery.

During physiological movements such as flexion, extension, lateral bending and axial rotation, the annulus fibrosus are under axial tensile stresses in all directions see Figure 1-5-2-1.

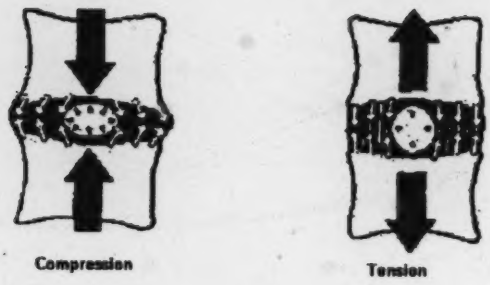

Figure 1-5-2-1 Tensile and compressive stresses in the intervertebral disc
(Modified from Kapandji, 1987)

Bending occurs when the spine is subjected to tension on its convex side and compression on its concave side during flexion, extension and lateral bending. Therefore, the effect on the disc is then a combination of compressive and tensile loads. The disc bulged anteriorly during flexion, posteriorly during extension and toward the concavity of the spinal curve during lateral bending [54]; see Figure 1-5-2-2.

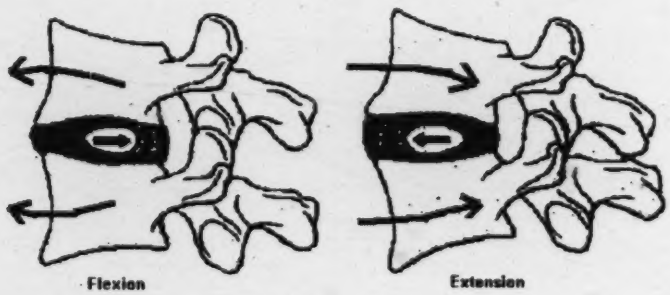

Figure 1-5-2-2 Bending of the spine
(Modified from Kapandji, 1987)

Axial rotation of the torso with respect to the pelvis causes torsional loads, which results in shear stresses in the disc. The disc is subjected to torsion when shear stresses appear in the transverse plane and the sagittal plane. The tension reaches to the central fibres of the annulus and causes compression in the nucleus increasing the internal pressure. This explains why flexion and axial rotation tend to tear the annulus and drive

the nucleus posteriorly through the tear in the annulus [54], as presented in Figure 1-5-2-3 and Figure 1-5-2-4

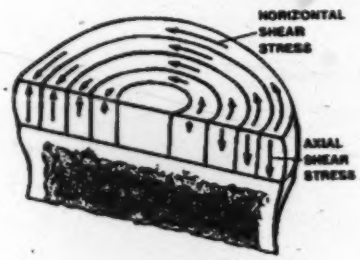

Figure 1-5-2-3 Horizontal and axial shear stresses in the intervertebral disc

Figure 1-5-2-4 Axial rotation between the vertebrae in the spine
(Modified from Kapandji, 1987)

During lateral flexion, the vertebral bodies rotate contralaterally. This automatic rotation of the vertebrae depends on two mechanisms: compression of the intervertebral discs and the stretching of ligaments. This rotation is normal, but in some cases the vertebrae are fixed in their position resulting in the development of abnormalities and the imbalance of the ligaments. The result is scoliosis, which combines fixed lateral flexion of the column with rotation of the vertebrae. This abnormal rotation can be demonstrated clinically [54].

The material behavior of the intervertebral disc is linear viscoelastic because of the high water content of the nucleus pulposus. Table 1-5-2-1 shows the mechanical properties of the intervertebral disc. The elastic modulus is independent of the spinal level. The shear modulus found is 1.6 N/mm^2 [56].

Author	Young's Modulus (N/mm^2)	Poison's Ratio
Goel and Weinstain, 1990	4.2 (annulus)	0.45
Suwito, et al., 1992	6.5 (annulus)	0.44
Skalli, et al., 1993	2 (annulus)	0.45
Skalli, et al., 1993	2 (nucleus)	0.499
Yoganandan, et al., 1995	3.4 (disc)	0.40

Table 1-5-2-1 Young's modulus of the intervertebral disc (Different sources)

Region	Tension +Fy (N/mm)	Compression -Fy (N/mm)	Ant. Shear +Fz (N/mm)
Thoracic	1000	1800	260
Lumbar	1000	1833	260

Table 1-5-2-2 Stiffness due to forces of the intervertebral disc (White and Panjabi, 1990)

Axial Rot. (Nmm/deg)	Flexion (Nmm/deg)	Extension (Nmm/deg)	Bending (Nmm/deg)
2000	2270	2270	2270

Table 1-5-2-3 Stiffness due to moments of the intervertebral disc (Modified from Tong, 1999)

1.5.3 Ligaments and Tendons

"Tendons and ligaments are soft connective tissues composed of closely packed, parallel collagen fiber bundles oriented to provide for the motion and stability of the musculoskeletal system. Ligaments connect bone to bone, whereas tendons connect

bone to muscle. Tendons generally have large parallel fibers that insert uniformly into bone. Ligaments have smaller-diameter fibers (70% dry weight), flattened elliptical cross section. These fibers can be either parallel or branching and interwoven" [27].

Physical and mechanical properties are a function of fiber arrangement, composition and microstructure. Tendon and ligament insertions to bone are functionally adapted to distribute and dissipate the forces, by passing through fibrocartilage to bone. Tendons and ligaments are well suited to the physiological movements. The parallel fiber arrangement of tendons and ligaments allows early tensile resistance once the "crimp pattern" is straightened [27].

Tendons are one of the soft tissues with highest tensile strength from 50 to 150 N/mm^2 and with Young's Modulus from 1200 to 1800 N/mm^2. Tendons are incompressible materials and exhibit small hysterisis; 90 to 96% of its energy is recovered. Tendons exhibit less viscoelastic behavior with respect to other soft tissues and the stress strain behavior is non-linear [27].

Ligaments are less strong and less stiff than tendons, due to lower collagen content, and more woven collagen structure compared to tendon's arrangement. However, ligaments have similar stress-strain behavior attributed to fiber straightening and stretching. Table 1-5-3-1 presents the stiffness values of the spinal ligaments.

Author	Young's Modulus (N/mm^2)	Poison's Ratio
Chazal, et al., 1985	45	0.3
Skalli, et al., 1993	10	0.3
Yoganandan, et al., 1995	1.5 – 30	0.3

Table 1-5-3-1 Young's modulus and Poison's ratio of the ligaments (Different sources)

Ligament	Young's Modulus (N/mm^2)	Stiffness (N/ mm)
Ligamentum Flavum (LF)	19.5	66.5
Transverse Ligament (TL)	3.7	58.7
Anterior Longitudinal Ligament (ALL)	164	12 – 44
Posterior Longitudinal Ligament (PLL)	164	11 - 37
Interspinous Ligament (IL)	41.5	11.6
Supraspinous Ligaments (SL)	55.1	62.7
Joint Capsule (JC)	49.7	32.9

Table 1-5-3-2 Young's modulus and stiffness of each spinal ligament (Modified from Goel and Weinstein, 1990)

1.5.4 Summary

The vertebral column consists of bones, intervertebral discs and various spinal tissues. The human spine is a strong, flexible rod that bends anteriorly, posteriorly and laterally, and it also rotates. In sagittal view, the human column shows four curves. This geometry provides increase in its strength, helps to maintain balance, absorbs loads and weights during the normal activities of a human, and helps to protect the human column from fracture.

The vertebra has a high Young's Modulus compared to the intervertebral disc, ligaments and tendons. Therefore in biomechanical studies, the vertebra is often considered as a rigid body with respect to the surrounding elements. One of the main tasks of the vertebra is to support most of the compressive loads and transfer them towards the intervertebral disc and then towards the pelvis. The lumbar vertebrae are the largest and strongest in the vertebral column, because the weight increases towards the inferior end of the spine. Therefore, their stiffness in the lumbar region is bigger than in the thoracic region.

The intervertebral disc is a complex structure that can support a variety of loading conditions. Therefore, it can be considered as the shock absorber in the spine and also the flexible attachment among the vertebrae. The stiffness coefficients for tension and

compression show that the intervertebral disc can be stiffer than the vertebra. This is possible because of the internal fluid pressure built in the nucleus of the intervertebral disc under the mentioned loading conditions.

The tendons and ligaments can be considered as elastic bands that provide attachment between bones and between bones and muscles. These connective tissues are the responsible for the adequate physiologic motion and fixed postural attitudes between vertebrae.

1.6 Idiopathic Scoliosis

Idiopathic scoliosis is an abnormal lateral curvature of the spine in the frontal plane for unknown reasons. There are two types of idiopathic scoliosis: structural scoliosis and functional scoliosis. Structural scoliosis is defined as a lateral curvature of the spine accompanied with the development of wedging and deformation vertebral rotation. Vertebral wedging or deformation does not accompany functional scoliosis. The present work is a study of structural scoliosis [2,3,21,40]. Figure 1-6-1 presents a classification of types of scoliosis.

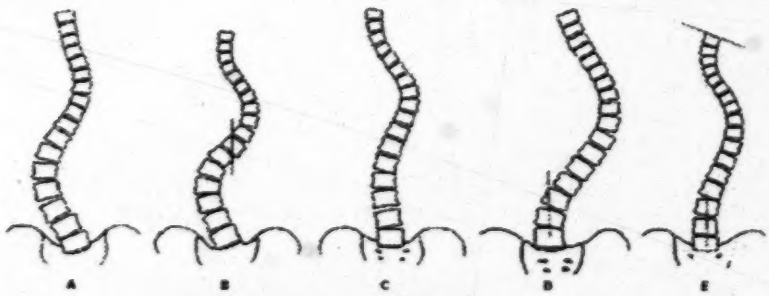

Figure 1-6-1 Types of scoliosis, classification King Moe
(Modified from King, et al., 1983)

A) S - shaped, Lumbar dominant
B) S – shaped, Thoracic dominant
C) Thoracic and Lumbar curve
D) Long Thoracic curve
E) Double Thoracic

There are several theories that explain possible causes of scoliosis. Those that are biomechanically based include Roaf, White and Ponsetti's.

Roaf (1966) suggested, "The basic problem in scoliosis is relative lengthening of the anterior components of the spine compared with the posterior components of the spine. The result is a lateral deviation of the spine and the subsequent development in scoliosis."

White (1971) mentioned that the coupling effects occur in lateral bending where the vertebra rotates along the longitudinal axis of the spine and the spinous processes point towards the convexity of the curve. "If some precarious balance of the normal thoracic motion should be disturbed, vertebrae in physiologic, right thoracic curve might somehow rotate too much into the convexity of the curve. Such occurrence could set off a chain of events leading to asymmetrical loads on the epiphyseal plates and muscles and ligamentous imbalance, with ultimate progression to scoliosis."

Ponsetti (1973) suggested, "a shift in the position of the nucleus pulpous towards the convex side of the curve might be a cause of scoliosis. The normal physiologic shift of the nucleus pulposus is toward the concavity of the curve."

As mentioned earlier, the spine supports, protects and gives mobility to the neural and human structures. The vertebral body, disc and ligaments provide the major support to the spinal column and absorb impact. The intervertebral, ligaments and muscles provide the mobility. In summary, normal spine functions depend on the reciprocal relationship among its structure, stability, flexibility, as well as the strength of its muscles and ligaments.

Any damage or alteration in the spinal system causes a disorder in its functions or shape. For example, scoliosis is a complex disease that damages muscles, ligaments, intervertebral discs and vertebrae. The next result is that scoliosis causes a sideways twisting and rotation of the spine.

1.6.1 Treatments of Scoliosis

Scoliosis treatment depends on the severity of the curve; this severity is defined by Cobb's angle. When the intervertebral discs are not deformed, the Cobb's angle is measured between the interception of the two perpendicular lines through the end plates of the most tilted vertebrae of the scoliotic curve. Usually the intervertebral discs are deformed in scoliosis; therefore, the Cobb's angle is the angle between the inflexion points of the scoliotic curve. Figure 1-6-1-1 shows how a Cobb angle can be found from a scoliotic spine.

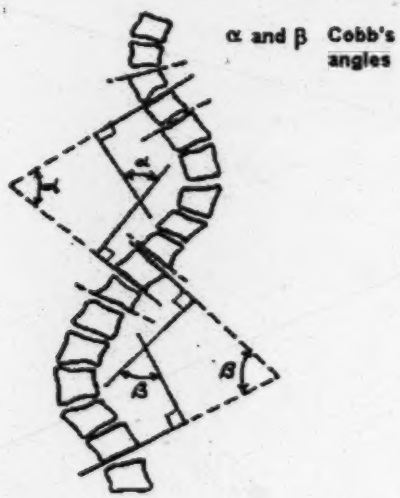

Figure 1-6-1-1 Cobb's angle
(Modified from Pope, et al., 1984)

The treatment of scoliosis can be divided into: observation, orthotic and surgical treatment. The following table summarizes a possible treatment to be followed.

COBB'S ANGLE (DEGREES)	TREATMENT
< 20	Observation
20 – 40	Orthotic
>40	Surgical

Table 1-6-1-1 Treatment of scoliosis
(Modified from Duke, 2001)

Clinically, scoliosis is detected as a rib hump while bending over. The symptoms vary with the person; some may experience headaches, back pain to dull back pain, hip and knee pain.

1.6.1.1 Observation Treatment

Once scoliosis has been identified, the treatment may start with observation. In the majority of cases, the prognosis is not well defined, and the patient needs to be observed for progression. The methodology consists of taking X-rays every four months during the first two years. After this stage, films every six to twelve months are appropriate once no further progression is seen. The routine consists of defining the position of each vertebra carefully measured to compare the location of the vertebra from a previous radiograph. It is essential to accurately measure the same spots on the same vertebra because the scoliotic curve may progress slowly and unpredictably [21,36,54].

1.6.1.2 Orthotic Treatment

Scoliosis is a deformity that occurs in the bones rather than in the soft tissues. Orthotic treatment consists of wearing braces where pressure is applied to strategic areas on the ribs, in hope of preventing further curve progression. A rational bracing program that involves dynamic bracing, muscle stimulation and strengthening with compatible exercise and nutritional therapy can achieve good results.

The Milwaukee Brace is constructed into a mold where the deformed patient is fit. The spine is supported by a rigid framework and stretched between the throat and occipital mold on one end and the pelvic girdle on the other. The method applies additional corrective forces using corrective pads attached in a vertical position of the brace. Some studies show that because of the localization of the pads and the exercises executed while wearing the vest, the Milwaukee brace provides both active and passive correction [54].

Boston brace studies reveal that the brace does not generate uniform distribution of forces. It does not correct the three-dimensional deformations of idiopathic scoliosis [12]. Although the brace reduces the Cobb's angle of the frontal plane, a negative effect appears in the sagittal plane. The negative result is the reduction of the thoracic kyphosis. This negative result is because the brace pushes the spine and the rib cage forward with no effects on the rib hump or vertebral rotation [24].

A traction head halter and/or ankle pelvic are two other corrective scoliosis methods. The method consists of distraction forces applied for long periods of time (about 3 weeks) to the skeleton [54]. The Halo traction can be combined with the pelvic hoop in order to straighten an oblique pelvis. It is advised to have a preoperative traction treatment in order to minimize:

- The risk of spinal cord damage.
- Minimized monitoring spinal responses and awakening the patient for the sensory functions.
- Reduce the possibility of failure in the lamina and pull out of the hooks from the rod.
- Help on the correction of double curves with different stiffness.

1.6.1.3 Surgical Treatment

Surgery is the most common treatment of severe or progressive spine deformities. For treatment of a Cobb's angle greater than forty degrees, surgery is recommended, because it will prevent further progression of the curve. Straightening of the spine is achieved with fusion combined in some cases with removal of the deforming growth potential on the convexity of the curve. It is accomplished using instrumentation that gives enough stability to keep the right position when fusion occurs [19].

Two instrumentation surgical treatments are commonly practiced:

- The Harrington instrumentation (HI)
- Cotrel-Dubousset instrumentation (CD)

HI consists of a distraction rod attached to the end of the curve in the concave side. The correction forces cause a lengthening in the spine, making the Cobb's angle smaller. The patient is able to move approximately one week after the surgery wearing a Milwaukee brace for six months [46].

In the case of CD surgical treatment, a rod is located along the spine and fixed with vertebra hooks for the correction. Rotation is applied to the rod from the frontal plane into the sagittal plane. The goal is to straighten the spine while restoring the thoracic kyphosis. The patient is able to move at the second or third postoperative day with out any external support [40].

The results from these two instrumentation procedures present no difference in the Cobb's angle correction. With respect to the sagittal profile, the thoracic kyphosis is better obtained from the CD method and, therefore, not necessary to remove spinal motion segments. However, the CD instrumentation could be dangerous while the rotation is occurring because of injury in the spinal canal.

1.6.2 Complications of Surgical Treatments

The risks associated with surgical treatment include: death, wound infection, gastrointestinal and genitourinary dysfunctions, pulmonary problems, and loss of blood. Therefore it is important to have preoperative and postoperative evaluations of the patient. The main complications are neurological, biological or mechanical [15].

Neurological problems are related to the approaching procedures to correct the spine. The main complication is stretching the nerve roots causing paralysis in the patient. Other complications are the damage in the aorta, vena cava, iliac artery, kidney, ureter and spleen [36]. The Biological complications result in failure of the bone mass to fuse so that the scoliosis collapses and the instrumentation may fracture due to fatigue failure. Osteroporotic bone is very fragile and it breaks easily, letting the hooks pull out of their place.

The main mechanical complication is hook pull out through the arch of the vertebrae, usually due to overloading or poor quality bone stock. In the case of the HI, the

mechanical complications are breakage of the rod and hook disengagement as well as hook force concentration-causing fracture in the lamina. The complications in the CD instrumentation are hook pulled out, prominent hardware, inadequate contouring of the rod and improper placement of the laminar or pedicle hooks [15].

After surgery, the greatest problem is lower back pain below the straightened curve. This problem appears in patients with fused lumbar vertebrae below the third one (L3). Thompson and Renshaw (1989) mention that a possible cause is the loss of lumbar lordosis and, therefore, the load transfer is increased and some segments have disc degeneration and facet colliding.

1.7 Development of a Pre-surgical Tool

Presently, the surgical treatment of scoliosis has a high degree of variability, because empirical and experiencential knowledge are involved. The surgical treatments involve the application of forces and moments to the spine or/and in the instrumentation. The creation of a pre-surgical tool will be a help to the medical doctors to analyze the applied forces to the scoliotic spine prior to the surgery. The computational program (i.e. pre-surgical tool) will simulate and predict the amplitude, location and direction of forces that are necessary to apply in order to obtain a desired correction.

Chapter 2

2.1 Literature Review

This chapter offers a background to understand the mechanics of the human spine and its congenital deformities. Three simulation-modeling categories, analytical, computational and experimental have appeared in the literature since 1970 to model the human spine. In general, analytical models attempt to demonstrate the geometrical relationship of the normal spine and its elements. The computational category based on numerical methods of mechanics pursues the simulation of the physiological motions of the spine. The experimental methods attempt to find the properties of the components of the spine.

Although each new model attempted to improve upon the previous ones, some limitations still remain. First, the lack of agreement in the experimental data from which accurate material properties may be assigned. Second, the lack of scoliotic spine models to predict the surgical correction in real time. The present models have incorporated a new finite element technique called constraint equations to minimize the computational costs.

Analytical studies:

2.1.1 Shultz A., Galante J.

A Mathematical Model for the Study of the Mechanics of the Human Vertebral, 1970 [44]

This model is a mathematical representation of the human vertebral column. It was done with a collection of equations expressing the mechanical relationships obeyed among its elements. The vertebra was idealized as a rigid body connected to other vertebrae and skeletal structures by deformable elements such as springs or any other element that can store mechanical energy. These deformable elements exerted forces that are functions only of their deformation. The vertebrae, rigid bodies, were interconnected by fixed length deformable elements representing the ligaments, intervertebral discs and muscles.

Cartesian coordinates and Euler angles were used to indicate the orientation of the body in the space. The simulation began with defining the position and orientation of one vertebra. Then, the next vertebra is found with geometrical relationships. Therefore, it is possible to find the position and orientation of consecutive vertebra using geometry. The results were validated with similar works done by others.

From this work is important to mention that it is possible to assume the vertebra as rigid body attached with deformable elements. The human spine is not geometrically constrained to have a pattern of motion; it can achieve many different configurations. Euler angles helped to describe the orientation of the body in three dimensions.

The main disadvantage of this model was the removing of some vertebral parts or shortening distances to obtain physiologic motion. The physiologic motion results from this study were lateral bending, flexion, extension and axial rotation.

Computational studies:

2.1.2 Subbaraj K., Ghista D. N., Viviani G. R.,

Presurgical Finite Element Simulation of Scoliosis Correction, 1989 [47]

A Scoliotic spine is modeled using Finite Element Method with deformable plane frame elements. The spine is considered as a beam column hinged at the bottom representing the sacrum and with free axial displacement at the opposite side representing the cervical end. The nodes of each element represented the centroids of each vertebra.

The spinal stiffness was determined *in vivo* applying incremental distraction forces to the head of the patients. The results were obtained from the displacement of the vertebral centroids located at the intersection of the diagonal lines that join the opposite corners of the vertebral body. The data were collected from X-rays of the patients' spines.

Small incremental sets of corrective forces in vertical and horizontal fashions were applied to the Scoliotic computational model, and linear deformation responses of the Finite Element Method were computed. The work was validated using instrumentation

designed for intraoperative monitoring of corrective forces and spinal deformations. During the surgery, both the distraction and the lateral forces were applied incrementally. At each stage those forces were compared with those predicted from the Finite Element Model.

From this work is important to consider the incremental loading fashion applied to the spinal deformity. The disadvantage of this work is that Scoliosis is a deformation in three dimensions and this work was only done in two dimensions.

2.1.3 Dietrich, M. Kedzior K., Zagrajek T.

A Biomechanical Model of the Human Spinal System, 1991 [13]

A three-dimensional biomechanical model of the spine using finite element method was programmed including: vertebrae, intervertebral discs, ligaments and back muscles. The model had 2,640 elements and 13,107 non-linear algebraic equations to be solved.

The vertebra was considered as a rigid body. The intervertebral disc contains finite elements with anisotropic elastic properties. The nucleus pulposus was considered as a liquid body in an incompressible space. The ligamentous system comprised the seven basic ligaments modeled with elastic elements with anisotropic properties. The back muscles system had linear anisotropic elements.

From this work it is important to point out how the muscle system kept the spine in an appropriate position and how the external influences acted on the spine. To keep the appropriate position, the muscle was supplied with minimum energy. This energy was proportional to the muscle elastic potential energy. External forces were treated as concentrated loads and transmitted to the spinal model through the shoulder girdle.

2.1.4 Steven Tong

A Mechanical Model of the Normal Human Spine, 1999 [50]

This model simulated and predicted the kinematic response of the normal thoracolumbar spine using Finite Element Method with 178 elements per vertebra and posterior elements.

The vertebra was modeled using solid brick elements with a very high Young Modulus, behaving as a rigid body. Ligaments and intervertebral disc were modeled with spring elements. The use of bi-linear spring elements in the Intervertebral disc structures and ligaments allowed for accurate modeling of spinal behavior during normal ranges of motion, but it yielded inaccurate responses during higher displacements. This is because this research work was done using the linear range only.

The work was validated using the functional unit through comparisons of stiffness values and displacements of existing studies conducted on excised spinal units. The functional unit consisted of two consecutive vertebrae and the associated interconnecting ligaments and disc. During testing, the inferior endplate perimeter on the inferior vertebra was constrained in all directions. Loads were applied to the superior vertebra to produce flexion, extension, lateral bending and axial rotation movements.

The model showed the coupling effects within the motion segments when lateral bending occurred. This effect happens when the vertebrae rotate along the longitudinal axis of the spine such that the spinous processes point towards the convexity or concavity of the curve in the thoracic or lumbar region respectively. In a scoliotic spine the opposite occurrence is noted.

This work highlights the importance of a simplified way to model the human spine using the intervertebral body, interconnecting ligaments and intervertebral disc. Some disadvantages are that the model works with small displacements and cannot be user defined for another type of geometry. The model takes a long computational time, in the order of seven to ten minutes per functional unit.

Experimental Studies:

2.1.5 Schultz, A.

Biomechanical Factors in the Progression of Idiopathic Scoliosis, 1984 [43]

This work studied the possible factors that might underlie the progression of idiopathic scoliosis. The study was done *in vivo* with adolescents of a mean age of 13.5 years and Cobb's angle of twenty-two degrees. Three biomechanical reasons were reviewed: the spine slenderness and flexibility, the strengths of the trunk muscles and the myoelectric activity in the trunk muscles.

From the study, slenderness and flexibility data obtained by the lateral clinical bending test did not show any dominant factor in the progression of scoliosis. The results from maximum voluntary trunk strengths presented no consistent differences between the structurally normal trunks and trunks with idiopathic scoliosis. These findings suggested that trunk muscles weakness in not a cause of progression of idiopathic scoliosis.

The study showed a significant variation between idiopathic scoliotic spine and normal spines when muscles contracted in response to electrical signals transmitted by the nerves. Patients with idiopathic scoliosis with curves more than twenty-five degrees had myoelectric asymmetrical signals than those of structural normal spines. The significant differences were found at lumbar level on the convex side of the erector spinae muscles while resisting flexion moment at the trunk.

Some other important findings were: at modest contraction and unilateral contraction of some trunk muscles can cause substantial increase in the Cobb's angle is noted. The internal abdominal obliques and the erector spinae increased the lumbar curve. The latissimus, intercostals and erector spinae can increase the thoracic curve. Application of weight on the upper body segments to a laterally curved spine can cause significant curve increase.

One possible source of progression of idiopathic scoliosis lies in defective neural system that control upright postures of the trunk. Therefore once the curve exists in a spine, any

weight on the body superior segment in the upright position creates a lateral bending moment that tends to increase the curve.

2.1.6 Takemura, Yamoto and Tani T.

Biomechanical Study of the Development of Scoliosis, Using a Thoracolumbar Spine Model, 1999 [49]

A physical thoracolumbar spine was modeled using synthetic vertebrae, silicon discs and nylon string. The vertebrae were joined with the silicon discs and nylon strings were attached to the spinal processes to the tip of the left transverse processes to simulate the back muscles. The spine was fixed at the sacrum and flexibly attached at the first thoracic vertebra in a metal frame.

In this model, ligaments and joint capsules were omitted to clearly see the deformation by the application of a force. The model did not consider the effects of the thorax, gravity or secondary deformation of the vertebral bodies from the muscular point of view.

It is important to emphasize how this biomechanical study attempted to clarify the development of the scoliosis related to the type of applied load. Lateral flexion, rotational and lordotic forces were simulated to evaluate the influence of them on the scoliotic deformation. This study found that the most severe scoliosis occurred when loading was done in the order of rotational force, lordotic force and lateral flexional force.

Takemura's study provided information of the silicone used in the thoracolumbar model. It suggested that the silicone is an element that may behave similar to the intervertebral discs under loads below 67 N. This study, also mentioned the way of the application of the forces in the model. Consequently, these ideas allowed me to use in the physical model silicone and wood to simulate the intervertebral disc and the vertebral body respectively. The physical model was built and tested with forces in the XY plane. Finally, the physical model was used to validate the computer model done in ANSYS for the present thesis work.

Chapter 3

3.1 Finite Element Method

In general, engineering problems are mathematical models of physical situations. Mathematical models are differential equations with a set of corresponding boundary and initial conditions. The ideal solution would be to solve every problem using analytical methods. However, for many practical engineering problems it is not possible to obtain exact solutions due to irregular boundary geometries, arbitrary boundary conditions, non-uniform material properties, non-linearity or coupling effects that appear. Finite Element Method (FEM) is one way to solve these kinds of problems [1,26].

FEM considers the body as a continuum, and it divides it into a number of discrete finite elements. In each element, the governing equations are algebraic. The complete solution is then generated by connection or assembling the individual solutions, allowing for continuity at the interelemental boundaries. For the present work, the ANSYS program is used. It is a comprehensive general purpose Finite Element computer program; it is capable of performing, static, dynamic, heat transfer, fluid flow and electromagnetism analyses [1,26].

3.2 Kinematics of Rigid Body Motion

A rigid body is defined as a system of mass points subject to holonomic constraints. In other words a rigid body is considered a system of particles in which the distances between them do not vary. Holonomic constraint means that the distances between all pairs of points belonging to the rigid body remain constant throughout the motion. A holonomic constraint can be expressed as equations connecting the coordinates of the particles (and possibly the time), (Goldstein, 1980) having the form:

$$f(r1, r2, \ldots\ldots, t) = 0 \qquad (3.2.1)$$

Examples:

Holonomic: the circle $(r_i - r_j)^2 - c_{ij}^2 = 0$ (3.2.2)

Non-holonomic: $r^2 - c^2 \geq 0$ (3.2.3)

A rigid body in space needs six independent generalized coordinates to describe its configuration and motion. These can be obtained by creating a moving Cartesian system of coordinates *x, y, z* fixed in the rigid body located relative to a fixed coordinate axis of the external space XYZ [20].

There are many ways to set forth the orientation of a Cartesian set of axes relative to another set with a common origin. One common procedure is to state the direction cosines of the moving system (x, y, z) relative to the fixed-system XYZ. The direction cosines are alpha (α), beta (β) and gamma (γ); These angles describe the instantaneous orientation of the body relative to a fixed coordinate system as can be seen in Equations 3.2.4 [20].

$$\begin{aligned} x &= \alpha_1 X + \alpha_2 Y + \alpha_3 Z \\ y &= \beta_1 X + \beta_2 Y + \beta_3 Z \\ z &= \gamma_1 X + \gamma_2 Y + \gamma_3 Z \end{aligned} \qquad (3.2.4)$$

These equations constitute a linear transformation from a set of coordinates X, Y, Z to a new set of coordinates x, y, z accomplished by orthogonal transformation. The array of transformation quantities, direction cosines, is called the transformation matrix. The transformation can be carried out from a given Cartesian coordinates system to another by means of three successive rotations performed in a specific sequence. Three successive angles of rotation performed in specific sequence are called Euler angles [20].

The most common convention used in applied mechanics and molecular and solid state physics is the XYZ convention or the nautical convention. The first rotation is the YAW angle (ϕ) about Z-axis, the second is the PITCH angle (θ) about the intermediate Y-

axis, and the third is a ROLL angle (φ) about the final axis X. Euler rotation matrix contains the above mentioned rotations. (See Equation 3.2.5.)

$$\begin{bmatrix} \cos\theta\cos\phi & \cos\theta\sin\phi & -\sin\theta \\ \sin\varphi\sin\theta\cos\phi - \cos\varphi\sin\phi & \sin\varphi\sin\theta\sin\phi + \cos\varphi\cos\phi & \cos\theta\sin\varphi \\ \cos\varphi\sin\theta\cos\phi + \sin\varphi\sin\phi & \cos\varphi\sin\theta\sin\phi - \sin\varphi\cos\phi & \cos\theta\cos\varphi \end{bmatrix} \quad (3.2.5)$$

The final position of the body after a known movement with respect to the fixed coordinate system is described by three angles (rotation matrix) plus a displacement (displacement matrix).

3.3 Constraint Equations

Constraint Equations (CE) are geometrical relationships among the points of a rigid body. The CE give the ultimate position of the points of the body after a known displacement and rotation.

One of the objectives of the present study is to use CE to replace the vertebral body. To do so, this study validates the CE in two dimensions, followed by generalization of the CE in three dimensions.

3.3.1 Constraint Equations in Two Dimensions

The CE for two dimensions is illustrated using geometrical drawing (see Appendix 2). A rigid plane is used and from it three points are selected. Two lines join the three points of the plane forming an angle. The angle-plane is subjected to a known translation and known rotation about one of the three points.

The vertex of the angle-plane is point number 1 and the rotation was done about this point. The initial and final coordinates of two points are known as well as the angle of

rotation, which was a small angle. A further analysis about small angles explains that the maximum allowed angle is 10 degrees.

The purpose of this geometrical procedure was to find the X and Y coordinates of the unknown point as a function of the geometry of the plane. It was found that the X and Y coordinate of the third point is a function of the point number one. The mathematical analysis of the geometry is given in Appendix 2.

The Finite Element Method involves small deflections in the order of 1 or 2% of the total length. The Euler rotation matrix is used to verify the results of the simplifications done with the geometrical results. The rotation matrix was tested for small angles. The purpose of this procedure is to find the maximum angle that can be considered the limit of the small angles to be used in the CE.

Displacement and rotation are given to the same three points of the mentioned rigid plane. The method consists of incrementing the rotation angle for three selected points. The points are subjected to different displacements and rotation in increments of one degree. Here one point of the three is presented that has an initial position: X = 10 mm, Y = 20 mm and Z =30 mm. The displacement applied is 20 mm in X direction, 10 mm for Y direction and 30 mm for Z direction. Figure 3-3-1-1 shows the final position of the point with the incremental angle value.

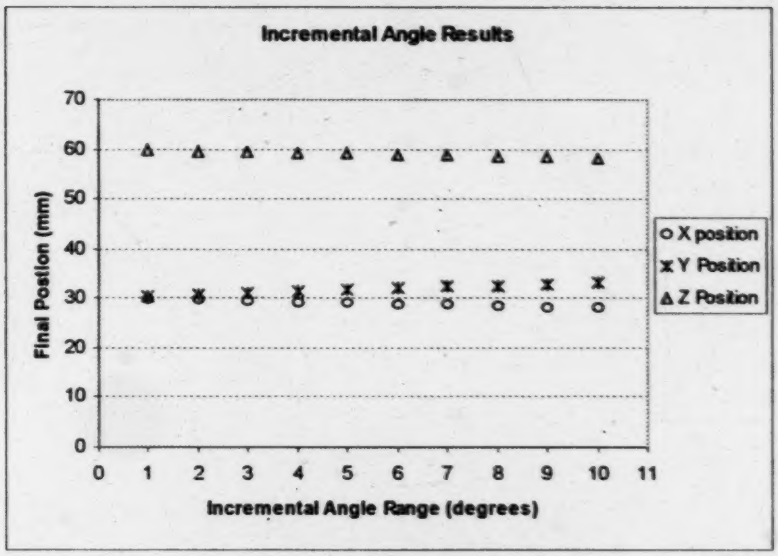

Figure 3-3-1-1 Incremental angle values

The criterion to choose this point is checking for the final results that give the major differences among the other results. Table 3-3-1-1 shows the three Euler angles psi (φ), theta (θ) and phi (Φ), and the resultant coordinates for each case.

Angles	X Coordinate	Y Coordinate	Z Coordinate
1-1-1	29.82	30.34	59.82
2-2-2	29.63	30.68	59.65
3-3-3	29.44	31.02	59.47
4-4-4	29.25	31.34	59.30
5-5-5	29.04	31.67	59.12
6-6-6	28.83	31.99	58.95
7-7-7	28.61	32.30	58.77
8-8-8	28.38	32.61	58.60
9-9-9	28.15	32.91	58.42
10-10-10	27.90	33.21	58.25

Table 3-3-1-1 Final position in X, Y and Z coordinates of the selected point

Table 3-3-1-1 represents the final position of the selected point in the X, Y and Z coordinate, using the incremental angle values. As is mentioned previously, each point was subjected to a 1-degree combination until the three Euler angles reached the value of 10 degrees of rotation. The first combination (1-1-1) of the Euler angles was assumed as the reference. Because the modeling was done in FEM, the test looked for a maximum value of small angles.

The previous table shows that when the combination is 10 degrees (10-10-10) of Euler angles, the percentage difference with respect to the reference (1-1-1) was in the order of 3.4% for the X coordinate, 5.4% for the Y coordinate and 1.5% for the Z coordinate. As a consequence, small angles can be considered less than 10 degrees for the present study. The present study established that the maximum accepted error was in the order of 15%. Therefore, the previous percentage results are accepted. A further study of the probable error is presented in Chapter Four.

Small rotation angles were used to simplify the final equations obtained from the geometrical results in Appendix 2. The final results using these simplifications are shown in the following equations:

$$U X_3 - U X_1 - C_1 + C_2 \, Rot Z_3 = 0 \qquad (3.3.1.1)$$

$$U Y_3 - U Y_1 + C_3 - C_4 \, Rot Z_3 = 0 \qquad (3.3.1.2)$$

$$Rot Z_1 - Rot Z_3 = 0 \qquad (3.3.1.3)$$

Where:

UX and UY represent the displacements in X and Y respectively for points 1 and 3.

Rot Z is the rotation about the Z-axis and

C_1, C_2, C_3, C_4 are constant that depending on the geometry of the rigid body.

The three equations represent the relationship between two points of any rigid body. As is mentioned before, the CE will give the ultimate position of the points of the body after displacement and rotation. The derivation of these equations is presented in Appendix 3.

The CE in three dimensions were derived from the Euler rotation matrix plus the displacement matrix. The rotation Euler matrix is manipulated with the same procedures mentioned before. The derivation of these equations is shown in Appendix 4.

To visualize the effectiveness of these equations two models were constructed in ANSYS. The models consisted of a frame of three elements using beams and CE. The beam model contains two vertical beams and one horizontal. The horizontal beam is very stiff compared to the other two beams and may be considered rigid. The CE model contains two vertical beams, and the CE replaced the horizontal element. The models were subjected to the same loading conditions, and the results were compared with the analytical solution. Figure 3-3-1-2 shows both models before and after the application of a load.

On the right side of the drawing the CE model is presented; the left side, the beam model is presented. The results are satisfactory proved between the two models with an overall error of 0.024% in displacement. This error includes the displacements in the X and Y direction and rotation about the Z-axis.

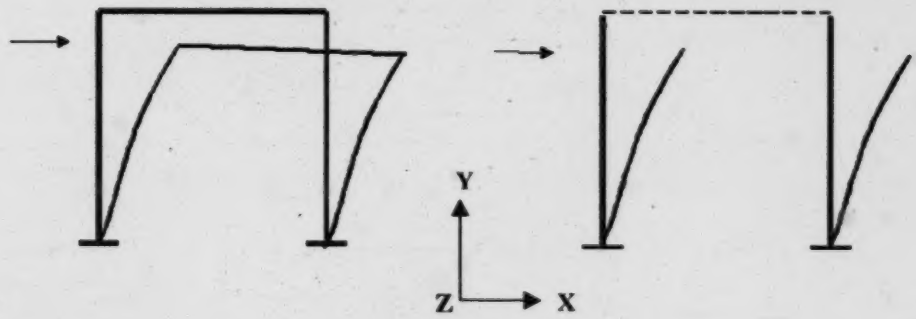

Figure 3-3-1-2 Beam model and CE model

3.4 Constraint Equations - Procedures

The stiffness matrix in the Finite Element Method contains the degrees of freedom of the analyzed body with its corresponding constraints. In this work, CE are used to model the movement of a rigid body. There are two commonly used procedures to apply CE; these are the collocation overdetermination and the trial solution method. When there are few degrees of freedom, these procedures may readily be performed manually, otherwise it is better to program the mentioned procedures.

3.4.1 Collocation Overdetermination

To solve an overdetermined system of equations, one method is to use the so-called penalty form of the matrix, which is related to the Lagrange multipliers technique. Using this method the CE are considered as the overdetermined factors. The solution of the system will give rise to the ultimate position of a rigid body after a displacement and rotation.

To begin with, the original FEM of equations without overdetermination as:

$$[A]\{x\} = \{b\} \qquad (3.4.1.1)$$

The overdetermined equations have the following form,

$$\begin{bmatrix} A_{nxn} \\ A^{o}_{mxn} \end{bmatrix} \{X_{nxl}\} = \begin{Bmatrix} b_{nxl} \\ b^{o}_{mxl} \end{Bmatrix} \qquad (3.4.1.2)$$

Where A^{o} and b^{o} are the overdetermined elements.

The above two system of equations are written in penalty form:

$$\begin{bmatrix} A_{nxn} & A^{oT}_{nxm} \\ A^{o}_{mxn} & -1/\alpha_{mxm} \end{bmatrix} \begin{Bmatrix} X_{nxl} \\ \lambda_{mxl} \end{Bmatrix} = \begin{Bmatrix} b_{nxl} \\ b^{o}_{mxl} \end{Bmatrix} \qquad (3.4.1.3)$$

$$-1/\alpha_{mxm} \quad set\ to \quad \begin{bmatrix} 0 & & \\ & \max(A^{0})/10^{6} & \\ & & 0 \end{bmatrix} \qquad (3.4.1.4)$$

As an approximation, it is solved the above square system with the diagonal submatrix:

Solving this penalized system yields the unique solution X (rotation and displacement).

3.4.2 Trial Solution Method

This method basically consists of eliminating rows and columns, when substituting the constraint degrees of freedom in the system. The system is established with nodes that have constrained degrees of freedom. These constrained nodes are related with the other degrees of freedom of the body by linear equations. From these linear equations the degrees of freedom are chosen and substitute in the system of equation. The system of equations begin with the original FEM system:

$$[A]\{x\} = \{b\} \qquad (3.4.2.1)$$

Using a constraint equation (CE):

$$C_1 A_1 + C_2 A_2 + C_3 D_3 = d \qquad (3.4.2.1)$$

where A are the degrees of freedom, and Ci and d are constants.
We now select one degree of freedom, and put it as a function of the others.

$$A_3 = \frac{d}{C_3} - \frac{C_1}{C_3}(A_1) - \frac{C_2}{C_3}(A_2) \qquad (3.4.2.2)$$

This value is then introduced into the system of equations. The substitution is done in each column. Once this is complete, the equation relating to the substituted degree of freedom, may then be eliminated. The final product is a simplified system of equations that has one less degree of freedom. This procedure is done continuously until all the CE are substituted in the system of equations.

3.5 Geometrical Non-linearity

Publications using orthotic treatment or surgical procedures for scoliosis have reported a large amount of correction to which a spine is subjected. In surgical procedures the reduction is bigger, starting with Cobb's angles greater than 40 degrees, so the relationship between the applied load and the resultant correction is non-linear [19].

According to linear Hooke's law, when assuming linear behavior, loads are in direct proportion to the displacement, while in geometrical non-linear behavior, loads are not. "Geometric nonlinearities refer to the nonlinearities in the structure or components due to the changing geometry as it deflects. That is, the stiffness matrix [K] is a function of the displacements {u}. The stiffness changes because the shape changes and/or the material rotates" [1].

For non-linear analysis, the tangent stiffness matrix assumes the role of the stiffness matrix in linear analysis. However, now the matrix (tangent stiffness) relates small changes in load to small changes in displacement. When calculating geometrical non-linear cases, Hooke's law is enforced at every stage when creating the stiffness matrix [1].

Geometrical non-linearity can be solved using analytical techniques or the FEM. Section 3.4 showed two procedures of how to apply CE in the system of equations used by the FEM. These procedures can be done in a generalized form (using large number of equations) when the method is programmed. Since the CE are directly involved with the stiffness matrix, the above-mentioned CE methods would not work with geometrical nonlinearities. This is because the methods used in Section 3.4 do not include any procedure to update the tangent stiffness matrix when the load is applied by increments. However, the present work studied the possibility to use CE for non-linear problems that consider geometric non-linearity.

To define what deflection corresponds to the linear or non-linear behavior, it was necessary to determine when non-linear modeling became important. The solution of a cantilever beam was used for this purpose. A cantilever beam, 1000 mm in length and 5 mm per side, was taken as the test model, and it was subjected to varying loading from 1000 to 8000 Nmm as shown in Table 3-4-1. The cantilever beam was modeled in ANSYS with and without non-linear option.

The displacements obtained from the non-linear model in ANSYS are determined in order to verify the results of the analytical linear solution. When small loads are applied, the linear analytical and the non-linear results should be identical. From this study, the limit between the linear and non-linear field was found. The limit was defined as the

diverging point between the results from the analytical linear and non-linear ANSYS model. In the Table, it occurred when the load is more than 8000 N with a percentage difference of 1.7%

Moment (Nmm)	Deflection ANSYS linear	Deflection ANSYS non-linear	Percentage Difference %
1000	48	47.9	0.2
2000	96.01	95.9	0.1
3000	144.01	143.6	0.3
4000	192.01	191.2	0.4
5000	240.01	238.5	0.6
6000	288	285.4	0.9
8000	384	377.7	1.7

Table 3-5-1 Results from linear and non-linear test of the cantilever beam

Since the purpose of this study was to use CE in the finite element analysis, CE were tested in three general cases presented in the following sections. The three general cases are done for the two-dimensional case. For the three-dimensional case, a cantilever beam is modeled using three-dimensional elements and subjected to the same loads as in two-dimensional cases. The results between the 3D and 2D models are compared, and the difference in the results is in the order of 2%. A possible reason for this difference might be due to the value of G (Shear Modulus) that is included for the three dimensional analysis only.

3.5.1 Frame with Horizontal Force

This model is done with three beams: two vertical and one horizontal. The vertical beams had one end fixed and the other connected with the horizontal beam in a fixed way. For the second model, the CE replaced the horizontal beam. The mechanical properties of the frame models are the mean values of the vertebral and intervertebral disc properties from the lumbar region.

Length of vertical beams (intervertebral disc height) = 20 mm

Length of the horizontal beam (width of the vertebra) = 40 mm

Area = 25 mm^2

Width of the beam = 5 mm

Height of the beam = 5 mm

Young's Modulus of the vertical beams = 4 N/mm^2

Young's Modulus of the horizontal beam = 12000 N/mm^2

Non-linear behavior for the frame model started with deflections greater than 2.8 mm corresponding to a load of 1.4 N. Representative values of load are shown in Table 3-5-1-1 in order to compare the results from the model that uses only elements with the model with CE. Figure 3-5-1-1a and 3-5-1-1b show the maximum deflection of the frame for both models.

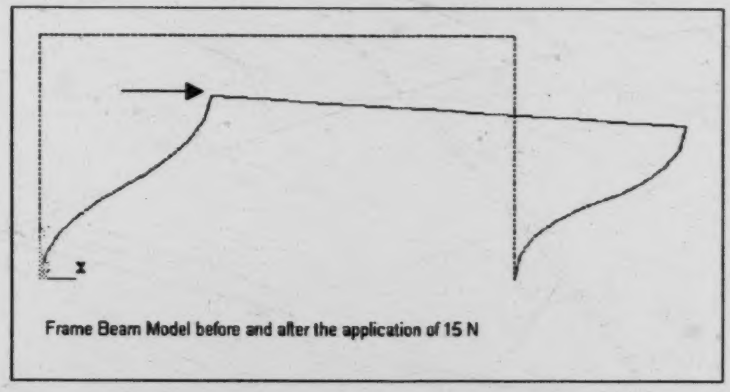

Figure 3-5-1-1a Model with beam elements with horizontal force

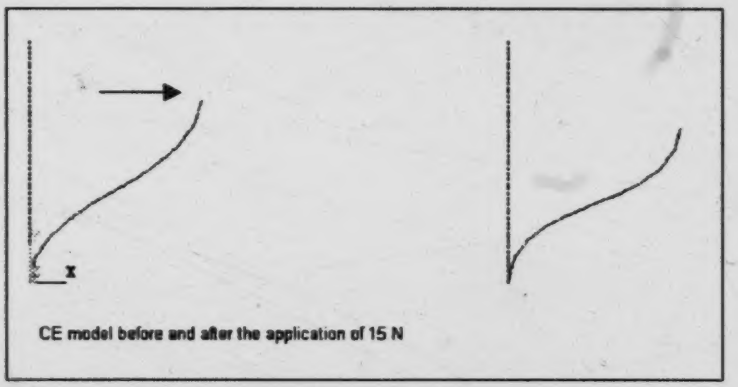

Figure 3-5-1-1b CE frame model with horizontal force

The percentage in the table represents the overall percentage error difference between the beam and CE models for all load cases.

	Load (N)	Ux (mm)	Uy (mm)	Rotz (rad)
Beam	3	4.6	-0.7	-0.3
	7	9.3	-2.8	-0.7
	15	14.4	-7.3	-1.2
CE	3	4.6	-0.7	-0.3
	7	9.2	-2.7	-0.7
	15	14.1	-6.9	-1.1
Mean +STDV	%	1.1 + 1	3 + 2.8	2.8 + 4.8

Table 3-5-1-1 Results from beam and CE frame models with horizontal force

3.5.2 Frame with Horizontal and Vertical Force

This case used the same mentioned model as in 3-5-1 with an additional vertical force applied to the top left corner. Table 3-5-2-1 shows representative load values with the respective displacement of both models. Figures 3-5-2-1a and 3-5-2-1b show that maximum deflection of the frame in both cases.

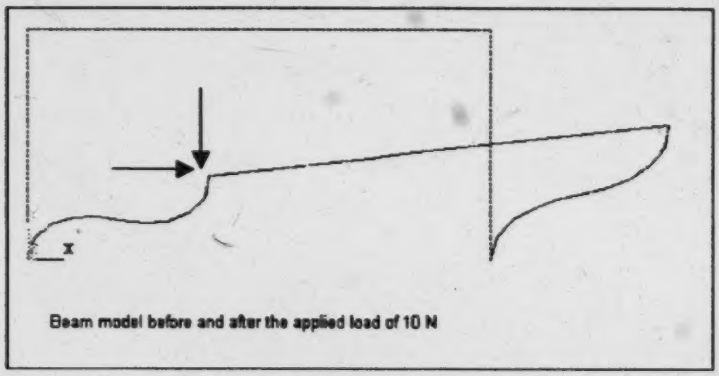

Figure 3-5-2-1a Model with beam elements with horizontal and vertical force

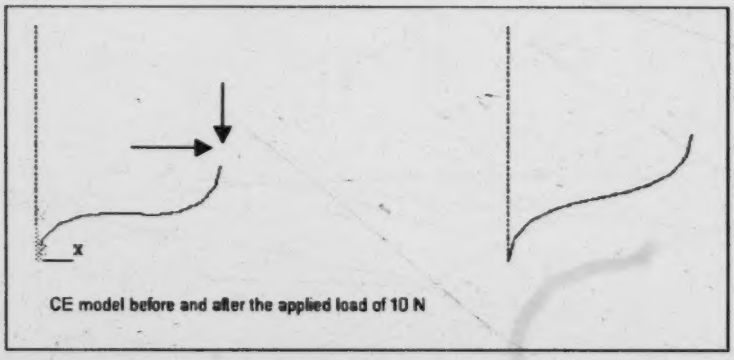

Figure 3-5-2-1b CE model with horizontal and vertical force

	Load in X and Y (N)	Ux (mm)	Uy (mm)	Rotz (rad)
Beam	3	5.8	-1.4	-0.4
	7	13.1	-7	-1.1
	10	15.6	-12.7	-1.7
CE	3	5.8	-1.4	-0.4
	7	13.1	-6.8	-1.1
	10	15.5	-11.6	-1.5
Mean + STDV	%	0.2 + 0.3	3.8 + 4.4	3.9 + 6.8

Table 3-5-2-1 Results from beam and CE models with horizontal and vertical force

3.5.3 Series of Blocks

A third case composed of a series of square areas formed by beam elements connected by two vertical beams was modeled. This model had the shape of a twelve-floor tower with the bottom fixed and the top end free. The model was a representation of a cantilever beam in vertical fashion, which was the way that the present work analyzed the non-linear case. Also, the idea behind this shape was to represent the spinal column composed of vertebrae and intervertebral discs.

Width of the block (thoracic spine width) = 32 mm
Height of the vertical beams (intervertebral disc) = 6 mm
Height of the square block (vertebra) = 18 mm
Number of floors in the tower with vertical beams (Number of intervertebral discs)=13mm
Number of floor with square blocks (number of vertebrae) = 12 mm
Width of the beam = 5 mm
Height of the beam = 5 mm
Young's modulus of the vertical beams (disc) = 4 N/mm^2
Young's modulus of the square areas (vertebrae) = 12000 N/mm^2

The model with beams used beams to build a square area that represented the vertebral body and two pillars that represented the intervertebral discs. The model with CE used the vertical beams as the intervertebral disc, and the CE replaced the vertebral body. The geometry and mechanical properties were mean values of the thoracic spine taken from Appendix 1. The modeling of the simulated vertebral column was done first with linear behavior for both cases.

The resultant displacements, X, Y and rotation about Z- axis, between the two models were compared. The error differences in the linear field for X was 0.63% , Y was 0.88% and rotation about the Z-axis was equal to 1.25%. Therefore results from the non-linear case are expected to have similar behavior. Non-linear behavior started when the load is bigger than 1 N.

Figure 3-5-3-1a shows the deflections of the models composed of beams, and Figure 3-5-3-1b shows the model using CE. Table 3-5-3-1 presents the deflection of both models under different values of load.

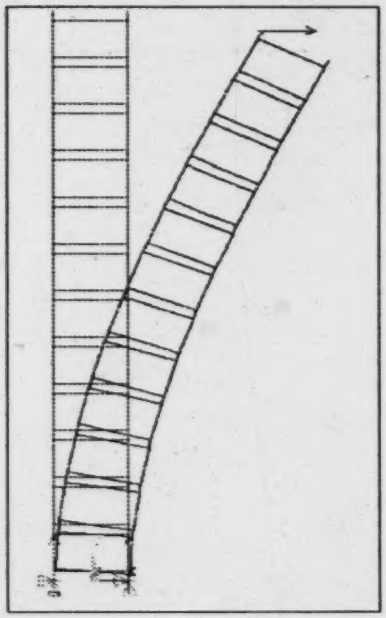

Figure 3-5-3-1a Beam series model

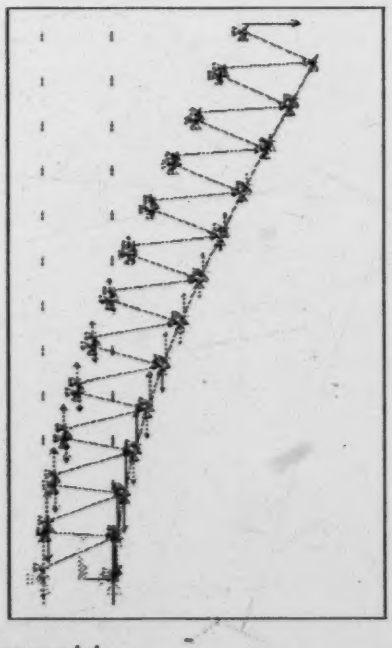

Figure 3-5-3-1b CE series model

	Load in X (N)	Ux (mm)	Uy (mm)	Rotz (rad)
Beam	1.5	65.5	-13.3	-0.3
	2	85.6	-20.7	-0.4
	2.5	103.9	-28.9	-0.5
	3	120.6	-37.6	-0.6
CE	1.5	65.7	-7.3	-0.3
	2	87.3	-10.8	-0.4
	2.5	108.7	-14.7	-0.5
	3	129.7	-19.1	-0.6
Mean + STDV	%	3.6 + 21.2	47.8 + 3.6	0+0

Table 3-5-3-1 Results from beam and CE series model with one end fixed

Table 3-5-3-1 presents the results from the beam and CE models. These results show that the model using CE does not have the same behavior when using elements. The table also verified what was mentioned in Section 3.5, where CE methods (Section 3.4) do not work for the non-linear case. It is because the CE methods do not include the change of the stiffness matrix when the load is applied in an incremental way. This difference is more noticeable in the third case (series of blocks) where the displacements in the Y direction are close to 48%.

Also, it is important to mention that for every run performed in ANSYS using CE in the non-linear cases, the program showed a warning message saying, "Constraint Equations may not be valid for elements that undergo large deflections." The results obtained from the last case showed that CE do not work with non-linear behavior.

Thus, a recommendation would be to continue the work using linear and non-linear field with elements, but when using CE only use the linear field or increments in linear behavior as is suggested by Subbaraj, et al., 1989.

3.6 ANSYS Elements and Constraint Equations

To develop a computational model that represents the human spine, each element of the spine needs to be selected according to its biomechanical behavior. The intervertebral disc is a complex structure that supports compression, tension, bending and torsion. On the other hand, tendons and ligaments have a cable-like structure capable of supporting only tensile but not compressive loads.

A beam is a uniaxial element with tension, compression and bending capabilities. A 2-dimensional beam element has three degrees of freedom at each node, displacement in the X, Y and rotation about the Z-axis. However, a beam element may not represent the real behavior of the intervertebral disc, tendons or ligaments, because the beam in the previous models behaves as a pillar supporting compression, bending or buckling.

To successfully model the spine using finite element techniques, it is essential to understand the behavior of each element in ANSYS. The intervertebral disc can support different loading conditions. Thus, elements that can represent its behavior closely are a set of springs used by Tong, 1999 or plane element used by Subbaraj et al, 1989. For the case of tendons and ligaments, a link element seems to be the best choice.

The spring or link element in ANSYS is a two dimensional element with uniaxial tension-compression properties which has two degrees of freedom at each node: translation in X and Y directions. Tong, (1999) used a set of forty-nine crossed spring elements with the idea of building a truss structure containing 17 vertically oriented and 32 diagonally oriented springs. A stiffer center spring in the structure, acting as a swivel joint between the adjacent superior and inferior endplates, simulates the function of the nucleus pulpous.

The plane element in ANSYS was another two-dimensional element with two degrees of freedom per node. The plane element can behave as plane stress or a plane strain element. To simulate the intervertebral disc the model had thickness, in other words used the plane stress option. The model was defined by four nodes having two degrees of freedom: translation in X and Y directions. Subbaraj, et al., 1989 used plane elements

to model the spine considering it as a beam column hinged at the bottom and having free axial displacement at the top.

The aforementioned work by Tong and Subbaraj has been validated; therefore springs or planes were used in the modeling. The use of these new elements, such as springs or planes, involves a change in the CE, because the actual CE involve rotations. A new setup for equations that replace the rigid body motion without rotations was carried out.

The new setup of CE with no rotation is found with the same concept used in the three dimensional CE. Rotational matrix and displacement matrix of two points from a rigid body was used, and the CE with no rotations was derived. The derivations are in Appendix 5. The resultant equations were:

$$\Delta UX_2 - UX_2\left(\frac{\Delta X}{L}\right) + UX_1\left(\frac{\Delta X}{L}\right) + UY_2\left(\frac{\Delta Y}{L}\right) - UY_1\left(\frac{\Delta Y}{L}\right) - Udx_1 = 0 \qquad (3.6.1)$$

$$\Delta UY_2 - UY_2\left(\frac{\Delta X}{L}\right) + UY_1\left(\frac{\Delta X}{L}\right) - UX_2\left(\frac{\Delta Y}{L}\right) + UX_1\left(\frac{\Delta Y}{L}\right) - Udy_1 = 0 \qquad (3.6.2)$$

Where ΔX, ΔY and ΔZ are local coordinates of the points 1 and 2 in the rigid body and L is the absolute length between the points 1 and 2. The CE with no rotation (CEN) were tested against models using elements, and the results were the same.

3.7 Meshing

Meshing is the process to form the nodes and elements to be used in the Finite Element Method. Meshing can be performed by two methods: mapped messing and free meshing. Mapped meshing is performed by defining a number of element divisions along the edges of the geometry. Therefore, the model usually require opposite edges. Free meshing, on the other hand, defines the outer region of the geometry and fills in the enclosed area or volume of the model.

As previously mentioned, constraint equations were used to modeling of the human spine. This method does not require any meshing as it simply relates the degrees of freedom of existing nodes that surround the vertebral body.

Chapter 4

4.1 Spine Simulation

The spine is a complex structure to model. As a result, most investigators use FEM with numerous simplifying assumptions to model it. The simplifications refer to the geometry and material data used to build the spine. The vertebra in the present work was considered as a rigid body in relation to the surrounding elements. The vertebra body was built in the frontal plane with constraint equations. To simplify the geometry, the vertebra was considered a rectangle. The material properties of the model were averaged values taken from experimental tests and/or published literature.

An experimental model was built to validate the results of the two-dimensional computational spine model. The experimental model consisted of blocks of wood attached with silicone. The wooden pieces in the experimental model represented the vertebral body, and the silicone represented the intervertebral discs. As is mentioned in Chapter Three, the intervertebral discs act as cushions between the bones. Hence, silicone was used to simulate this behavior, and two experimental tests were carried out in order to obtain its properties.

Based on the product information of the silicone, the expected error in the properties of this material falls in the range of 5%. Another ten percent more was attributed to the geometrical problems and measurement procedures. Therefore, a total value of 15% difference is expected between the theoretical and the experimental results. Displacement measurements of the specimens were done using accurate measurement tools, such as dial gauges, calipers, and metallic rulers.

The mechanical properties for the silicone material (as stated in literature) were not used in the present study because they referred to a different silicone. However, these properties gave a reference of how much the expected values of the experimental tests should be.

4.2 Probable Error

Probable error in measurements is called uncertainty. It defines an interval about the measured value within which the true value is expected to fall. Although no general discussion of errors can be complete in listing the elements contributing to error in a particular measurement, a certain generalization for error sources can be made to help in their identification. As a consequence, it is possible to make an estimate of the error of a variable based on the error of the other variables involved with it in an equation.

The probable error of a sum or difference is the square root of the sum of the squares of the individual probable errors. The probable error of a product or quotient is necessary to convert the probable error to a percentage. Then the probable error is equal to the square root of the sum of the individual probable percentages of errors. The probable error of a measurement multiplied or divided by a pure number is the probable error of the measurement multiplied or divided by the number. The probable error of a measurement raised to a power is the probable percentage error of the measurement multiplied by the power [15]. For example, a purely multiplicative equation is

$$Q = A_1 * F^a * G^b * H^c \qquad (4.2.1)$$

where A_1, a, b and c are constants that can be either positive or negative. To find the effect of errors in F, G and H on the function Q, the equation has to be differentiated with respect to each variable, and, therefore, the constant A_1 is eliminated. The product of these steps leads to the following equation:

$$\left(\frac{eQ}{Q}\right)^2 = a^2\left(\frac{eF}{F}\right)^2 + b^2\left(\frac{eG}{G}\right)^2 + c^2\left(\frac{eH}{H}\right)^2 \qquad (4.2.2)$$

The square of the fractional or the percentage error or probable error in each variable is weighted by the square of its exponent.

The following table contains some variables that affected the behavior of the experimental models (silicone disk) with their correspondent errors. The probable error

for the height and width was calculated using the probable error from the metrical measurements obtained by the caliper for inside the silicone disk. The probable error of the area was obtained using the equation 4.2.2 with the height and width of each face in the silicone disk. The probable error of the Young's modulus was obtained using the equation 4.2.2 from the deflection of a beam. The known values of the deflection equation were the applied load, the height, the area and the deflection of the silicone disk. In the same way, the probable error of the maximum deflection of the physical model was calculated. Finally, the probable error of machine design was calculated from the repeatability, resolution and linearity of the coordinate measuring machine.

Case	Variable	Value	Probable error
PFU-1	Height of silicone disk	6-7 mm	0.72 mm (11%)
PFU-1	Width of the silicone disk	25 mm	0.70 mm (2.8%)
Shear test	Load	907.25 gr	5.11 gr (0.5%)
PFU-3	Area	200 mm^2	5.85 mm^2 (2.9%)
PFU-2	Area	112 mm^2	12 mm^2 (10.7%)
Compression	Young's Modulus	2.54 N/mm^2	0.23 N/mm^2 (9%)
Physical Model	Max. Deflection	8 mm	0.796 mm (9.9%)
Coordinate Measuring System	Design	406 mm	0.0073 mm

Table 4-2-1 Probable error

The maximum error obtained from the different variables was in the order of 11%, due to the geometrical problem (height and width of the silicone disc). Another 9% was attributed to the material properties (Young's modulus). Finally, a maximum error in the order of 9.9% was due to the deflection results from the physical model. If these errors were related in an equation similar to 4.2.1, the total maximum errors would be 11%.

The maximum percentage error difference accepted in this study was 15%. This percentage was considered the maximum value among the results from computer simulation, theoretical analysis and experimental tests. In Chapter Three, the 15% difference accounted for simplifications and the order sequence of rotation done in the rotation matrix to obtain the constraint equations. A value of 11% accounted for

geometrical differences in thickness, height and depth as well as in material properties – 4% more from irregularities in the silicone disk, human error when taking measurement as well as uncertainty concerning procedural or instrument calibration and repeatability.

4.3 Experimental Model

Takemura, et al., (1999) found a relationship between the physical spine model in their study with the human spine. Their biomechanical study attempted to clarify the development of scoliosis related to the type of applied load. Based on their study, the idea to build a physical model seems effective because of the possibility to obtain deflection with different loading conditions similar to the ones supported by the human spine.

The physical model consists of square pieces of wood with dimensions that are the geometrical average values of the vertebra in the thoracic region. The area of the block is also the average value of the endplates of the vertebra with a value of 625 mm^2. Mechanical properties of the wood were found in [6] and in the material properties of the intervertebral disc from experimental tests.

The silicone used in the present study was multi-purpose Sealant 732 from Dow Corning®. This sealant is designed for a number of diverse sealing and bonding applications with metal, fabric, wood and glass. It cures at room temperature by reaction with moisture in the air to produce a durable, flexible silicon rubber. The silicone was recommended for this experiment because it is a deformable element suitable at the point of stiffness to maintain the disc height [49].

Only one study was found in literature [4A] of the material properties of the Sealant DC999 from Dow Corning®. The study presented an experimental investigation of the material under different ASTM[1] standard tests, such as bending, shear and tension. The specimens in this study were prepared with conditioning standards during 7 weeks.

[1] American Society for Testing and Materials

Figure 4-3-1 presents the published Stress – strain curves for tension and shear for silicone DC999.

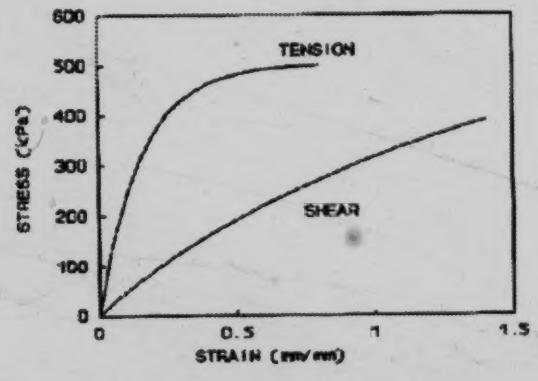

Figure 4-3-1 Stress-strain silicone DC 999 (from ASTM STP 1271,1996)

A Young's modulus of 2.54 N/mm^2 was determined from the stress-strain curve in Figure 4-3-1 in the range of 0-0.06 N/mm^2. A shear modulus of 0.461 N/mm^2 was determined as well in the linear range from 0-0.06 N/mm^2 from the shear curve. Based on this ASTM study, silicone 732 has close values of the material properties as silicone DC999.

The product information for silicone 732 gave the tensile strength value of 2.24 N/mm^2, which when compared with the silicone DC999 is smaller. Hence, the mechanical properties of silicone 732 would have smaller values than those of silicone DC999. In order to know the values of the mechanical properties of silicone 732, two tests were carried out.

Data from these tests were used to find the shear modulus and the stiffness of the silicone. Stress-strain and load-displacement graphs show that the material has a linear behavior in the tested range. Data from ASTM experimental tests show that the material has a non-linear behavior when the load is more than 1000 N for the tension test and 500 N for the shear test.

4.3.1 Shear Test

Four blocks made of silicone 732 were molded between pieces of wood during seven days at room temperature according to the specifications of the product. The specifications providing the cure time information for 1/8 inch (3.175 mm) bead are 24 hours exposure to air at 25°C and 50% RH. The dimensions of the silicone blocks were as follows: length = 35 mm, width = 35 mm and depth = 12 mm. Figure 4-3-1-1 shows the set up of the test.

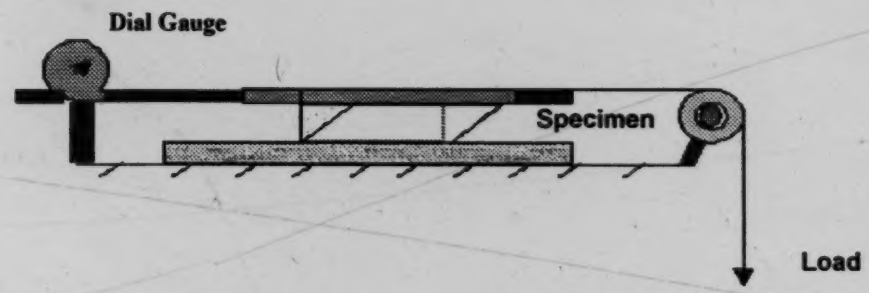

Figure 4-3-1-1 Set up for the shear test

The test consisted of hanging different weights from one end of the top wooden piece and, from the other side, recording the readings with a dial gauge each time that the weight changed. Thus, the shearing stresses act tangentially to the surface of contact and do not change the length of the sides of the volume. On the other hand, the volume changes the angle between the faces and the length of the diagonal. Two pairs of shearing stress intensities must act together; therefore, the lower wooden piece is constrained. The specimens were tested twice: the first test with 7 days of curing and the second test with 7 weeks of curing at room temperature.

All the following graphs present a line that fits the data using the least squares method. The slopes of the curve represent the Young's modulus or shear modulus for the stress-strain curves as well as the stiffness in compression and in shear for the load-displacement curve. The following figures show the graphs obtained from the shear test. Figures 4-3-1-2a,b present the stress-strain curves for 1 and 7 weeks of curing.

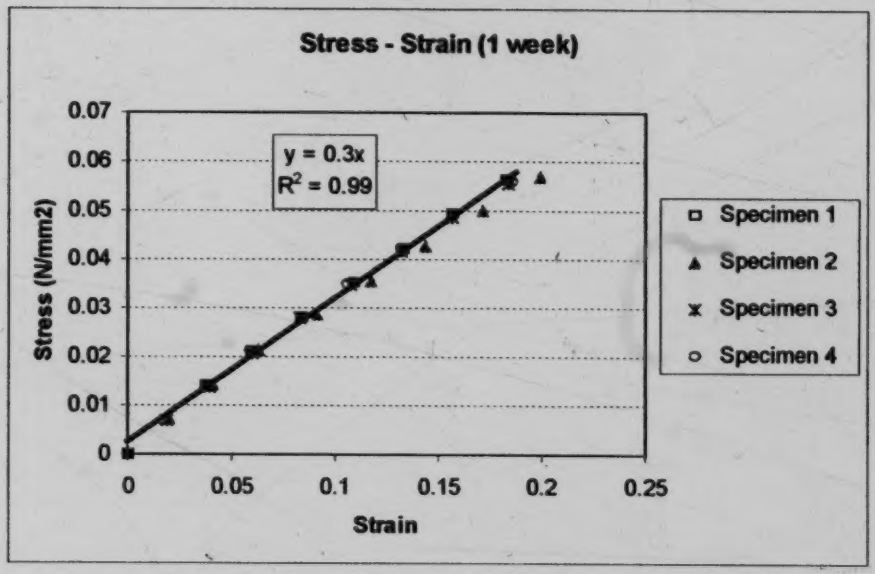

Figure 4-3-1-2a Stress-strain shear curve of silicone 732 cured 1 week

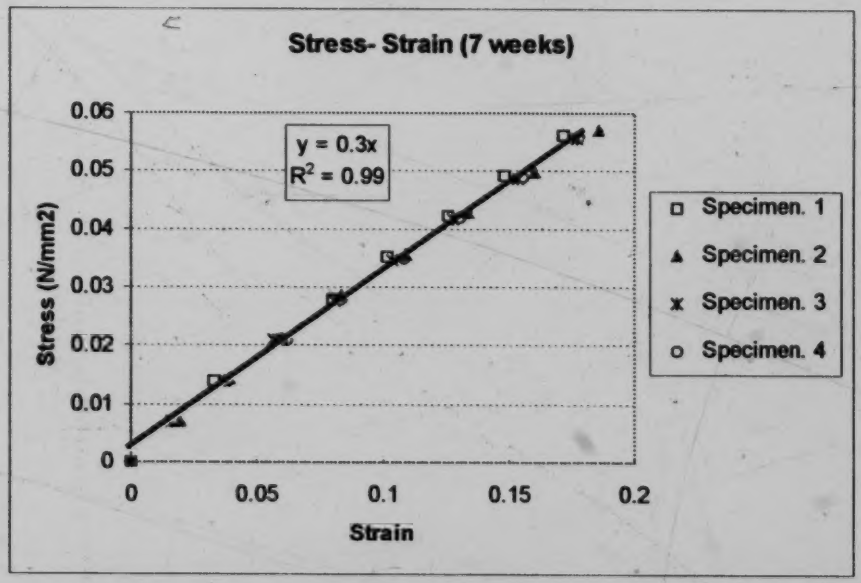

Figure 4-3-1-2b Stress-strain shear curve of silicone 732 cured 7 weeks

It can be seen that the material properties did not significantly change the pattern of the linear behavior between the two periods of time. The specimens were checked for

hysterisis, and it was noticed that the material completely recovered its original shape. The hysterisis error is presented in equation 4.3.1.

$$eh_{max} = \left(\frac{Y_{up\,scale} - Y_{down\,scale}}{Full\ scale\ output\ range} \right) * 100 \qquad 4.3.1$$

eh_{max} = 12.5%

The meaning of this percentage is the amount the material loses in energy during the recovery of its original shape. The results presented below were for the specimens for one week of curing.

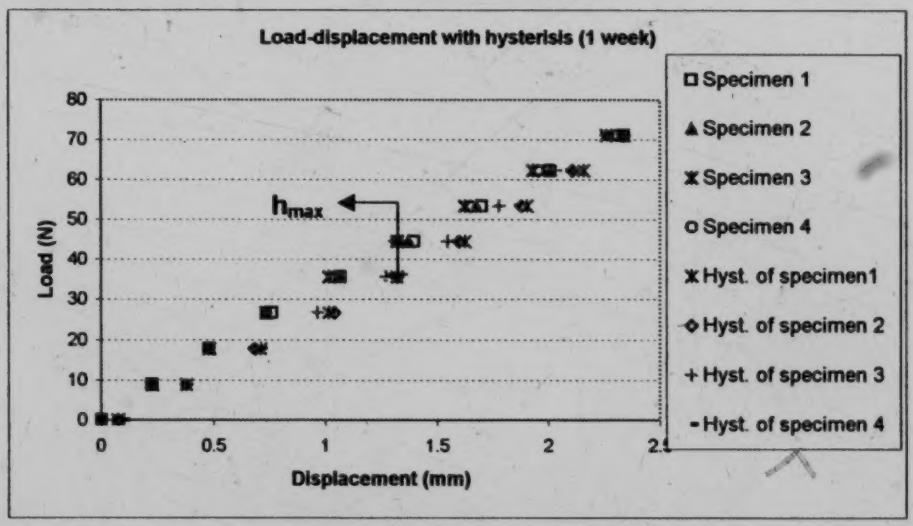

Figure 4-3-1-3 Hysterisis results for the shear test of silicone 732

As mentioned before, the ASTM test had a shear modulus of 0.461 N/mm^2 while the shear modulus for the present test is 0.304 N/mm^2. This value of shear modulus in fact showed that silicone 732 has lower mechanical properties than silicone DC999 as mentioned before.

Another material characteristic obtained from the experimental shear test was stiffness. The slope of the curve represents the stiffness in shear of the silicone. Using the least squares method, the data obtained by the four specimens were fitted with a line. Figures

4-3-1-4a,b present the load-displacement curves for one and seven weeks of curing time.

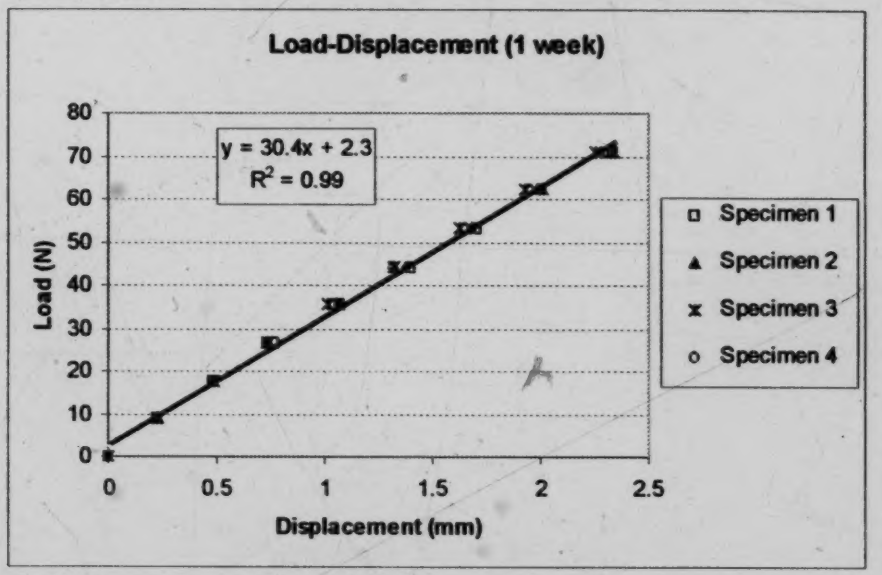

Figure 4-3-1-4a Load-displacement shear curve of silicone 732 cured 1 week

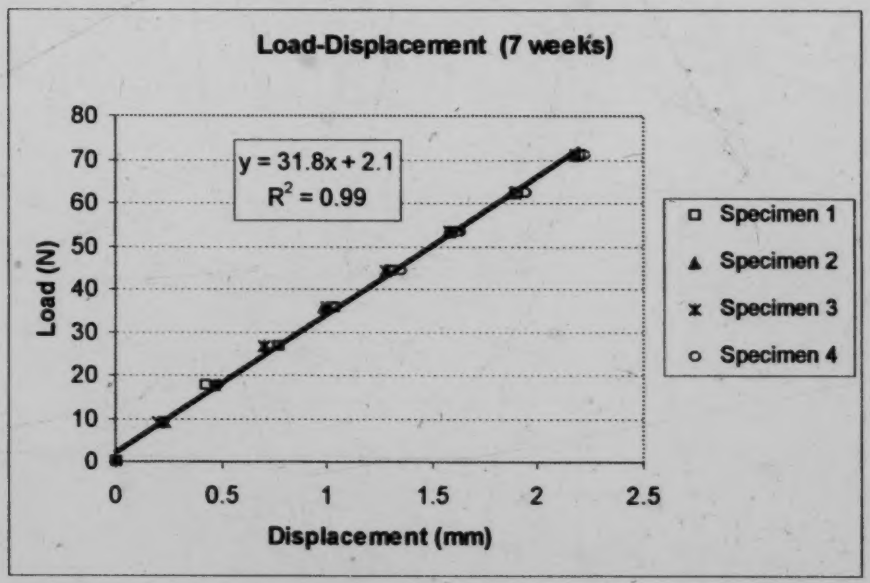

Figure 4-3-1-4b Load-displacement shear curve of silicone 732 cured 7 weeks

Table 4-3-1-1 presents the stiffness and shear modulus at different curing times for the four specimens. At the end of each curing time, the mean value among the four specimens is recorded with the respective standard deviation.

Cured Time (Weeks)	Specimens	Stiffness (N/mm)	Shear Modulus (N/mm^2)
1	1	29.9	0.3
	2	30	0.2
	3	31.2	0.3
	4	30.6	0.3
Mean + STDV		30.4+0.6	0.2+0.01
7	1	31.7	0.3
	2	32.2	0.3
	3	32	0.3
	4	31.4	0.3
Mean + STDV		32+0.3	0.3+0.0

Table 4-3-1-1 Stiffness and shear modulus of silicone 732

A student T test was done using the stiffness information provided in the above table. The test is presented in Section 4.3.3.

4.3.2 Compression Test

According to ASTM, silicone is considered as rubber or elastomer, Consequently, Designation D395-98 [5] is used as a reference for the compression test. The compression specimens are cylindrical disks with ½ in. (12.7 mm) thickness and 1 ½ in. (38.1 mm) diameter. The cure time was specified by the information of the product, and the conditioning temperature was 23 ± 2 °C. Four silicone cylindrical specimens were molded during one week, and another set of four specimens was molded during five weeks.

The ASTM experimental study presented the tensile test. The present thesis work chose to use the compression test to obtain the compressive properties, since the vertebra and intervertebral disks are mostly loaded under these conditions. The compressive stress-strain curve is similar to the tensile stress-strain curve up to the tensile strength. Thereafter, progressively increasing specimen cross-section causes the compressive stress-strain curve to diverge from the tensile curve.

The test consisted of placing the specimen in the center of a flat surface and subjecting it to continued compression force using the Instron machine with a velocity of 1.27 mm/min (0.05 in/min) [5]. The load is applied slowly enough so that all parts of the specimen are in equilibrium at any instant. The machine gave the results as a curve: loading versus deflection. Figure 4-3-2-1 illustrates the set up for the compression test.

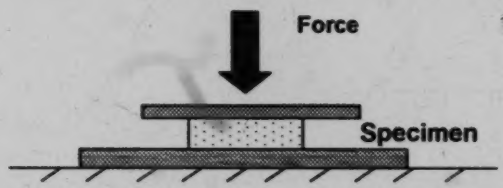

Figure 4-3-2-1 Compression set up

Similar to the previous section, the properties obtained from this test were Young's modulus and stiffness. The maximum load applied was 200 lb (890 N) for the 1 week curing time specimen and 220 lb (980N) for the 5 weeks curing time specimen. According to the properties of sealant DC999 for more than 1000 N in load, the material starts to behave non-linearly. Because the information obtained from the shear test presented little difference between the results from the one and seven week tests, the second test was done with 5 weeks of curing.

Two different sets of compression specimens were tested. The following figures show the graphs obtained from these tests. The results given by the four specimens were fitted with a straight line using the least squares method. The slope of the curve stress-strain represents the Young's modulus for compression, and the slope of the curve load-displacement is the stiffness of the material for compression. The graphs represent the

stress-strain and load-displacement curves. Figures 4-3-2-2a,b depict the stress-strain compression curves for 1 and 5 weeks.

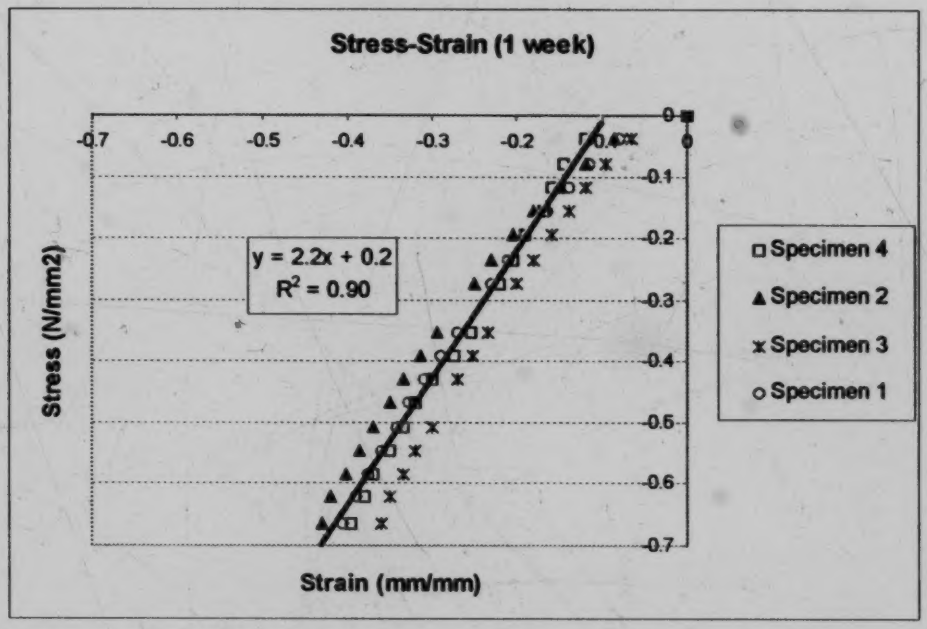

Figure 4-3-2-2a Stress-strain compression curve of silicone 732 cured 1 week

It is shown in the figure below that the results in the second test with five weeks of curing present a convergence between the results of the specimens. The specimens were checked for hysterisis, and, the material recovered its original shape. The hysterisis was done unloading the specimen straight from the last loading value up to zero value of load. The hysterisis error in this test for 1 week of curing was 10%, which is a smaller value than the one obtained by the shear. The hysterisis value also means that the material has a linear behavior, and it recovered its initial height in less time than in the shear test. The Young's modulus given by the compression test in the present study was on average 2.28 N/mm^2; while, for the ASTM tension-test, the Young's modulus is 2.54 N/mm^2.

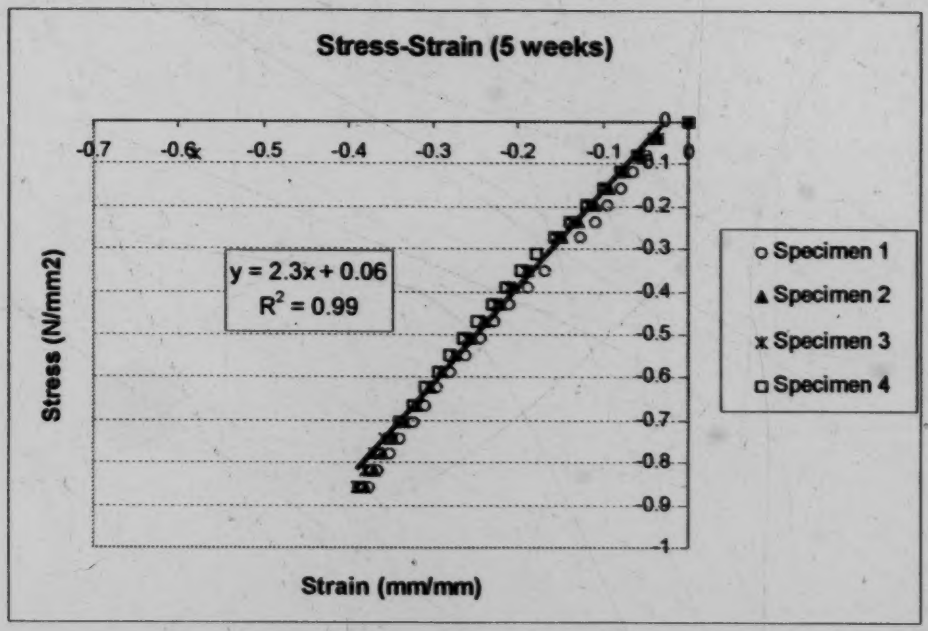

Figure 4-3-2-2b Stress-strain compression curve of silicone 732 cured 5 weeks

The stiffness in compression was another property obtained from this test. In the case of the stress-strain curve, the slope of the first test had a slightly different value from that of second. The value of the slope in stress-strain curve for the one-week test was 2.25, and the value for 5 weeks was 2.31. This small difference means that the material has become stiffer during that time. As was mentioned before, due to the irregular geometry that the first set presented, the second test used another set of four specimens. However, the results obtained from both tests were consistent.

The difference between the slopes also is attributed to the stiffness increase with the time. In this case, 192.5 was the value for one week and 208.8 for five weeks. The second figure of load-displacement presents a noticeable convergence between the specimens. This pattern is not noticeable in the curve stress-strain. All results given by the specimens sustained the prevalence of the linear behavior at any time of testing.

Figures 4-3-2-3a,b present the load-displacement curves for one and five weeks of curing time.

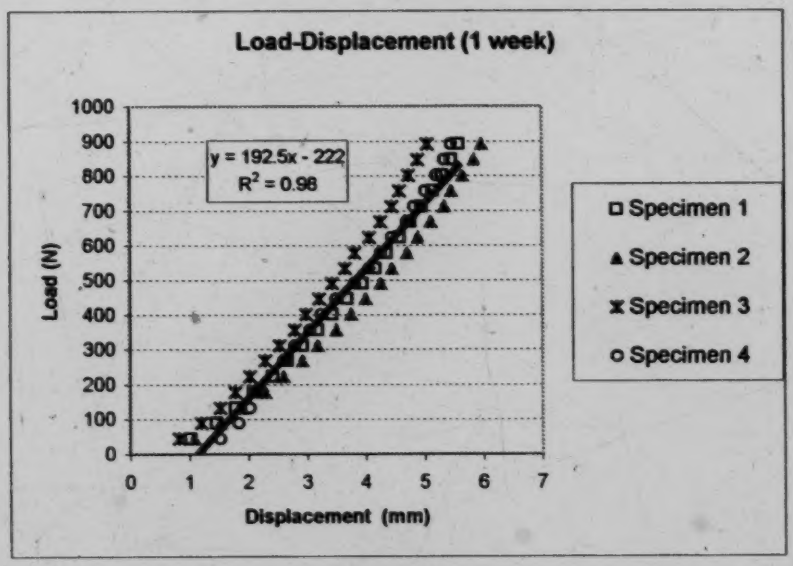

Figure 4-3-2-3a Load-displacement compression silicone 732 cured 1 week

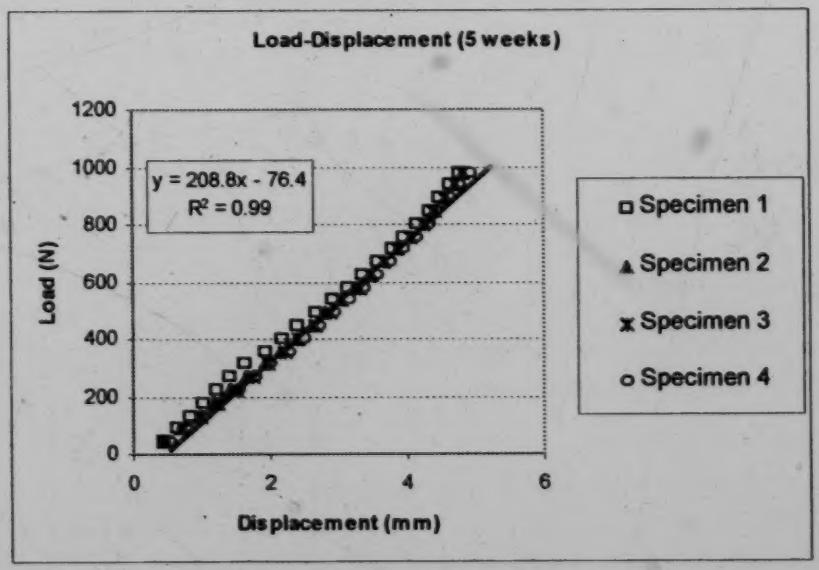

Figure 4-3-2-3b Load-displacement compression curve of silicone 732 cured 5 weeks

Table 4-3-2-1 presents the stiffness and shear modulus at different curing times for the four specimens. At the end of each curing time, the mean value between the four specimens is recorded with the respective standard deviation.

Cured Time (Weeks)	Specimens	Stiffness (N/mm)	Young's Modulus Compression (N/mm^2)
1	1	186.1	2
	2	174.3	2.3
	3	202.6	2.2
	4	207.2	2.3
Mean + STDV		192.5+15	2.2+0.1
5	1	205	2.2
	2	207.7	2.3
	3	211.3	2.3
	4	210.9	2.3
Mean + STDV		208.7+2.9	2.3+0.02

Table 4-3-2-1 Stiffness and compression Young's modulus of silicone 732

4.3.3 Student T Test for Sample Means

To determine the standard deviation of the mean in terms of the standard deviation of the population, the T distribution test results are presented in Table 4-3-3-1. This test allows one to determine if two different means come from the same population or not.

X_{sA} = Sample mean of the first test at one week.

X_{sB} = Sample mean of the second test at five or seven weeks.

S = Standard deviation.

N = Number of degrees of freedom.

Case	X_S	S	N	T test
Shear stiffness	30.4	0.6	4	95 %
	32	0.3	4	
Compression stiffness	192.5	15	4	8%
	208.7	2.9	4	

Table 4-3-3-1 Student T test for sample mean results

As is shown in the previous table, the first case represents the probability that X_{SA} and X_{SB} are from the same population. On the contrary, the second case (compression) shows that the X_S values are from different populations. This is a fact since the compression specimens for the first time were different than the ones used in the second test. However, the results obtained from the two compression tests matched the expected value in the Young's modulus. The expected value was 2.54 N/mm^2 with 15% error; the value found from the experiments was 2.28 N/mm^2.

4.3.4 Intervertebral Disc vs. Silicone Disk Material Properties

Once the material properties of the silicone were set, the next step was to compare them with the mechanical properties of the intervertebral disc. Table 4-3-4-1 presents the material properties of the intervertebral disc and the silicone disk.

It can be seen that the Young's modulus for compression of the silicone was the only property close to the intervertebral disc one. On the other hand, the other three properties are many times smaller than the intervertebral disc properties. This, is justified due to the composite structure of the intervertebral disc, the intervertebral disc properties have maximum or traumatic load involved. The orientation of the fibers and the internal pressure built up under compression or axial torsion creates a structure with high properties, even bigger than the vertebral body. Chapter One discusses the biomechanical behavior of this complex structure.

Element	Shear Stiffness (N/mm)	Young's Modulus (N/mm^2)	Shear Modulus (N/mm^2)	Compression Stiffness (N/mm)
Intervertebral	260	3.62	1.6	1833
Silicone	31	2.2	0.3	200

Table 4-3-4-1 Material properties of the intervertebral disc and silicone disk

4.3.5 The Physical Functional Unit

The physical functional unit consisted of two pieces of wood glued with silicone. This experimental model is called the physical functional unit, because it represents the same idea as of the functional unit in the spine biomechanical studies. Three physical functional units were molded during 2 weeks with different thickness of the silicone disks. The different thickness in the silicone disks is due to the scoliosis problem with irregular shapes in the intervertebral discs. Figure 4-3-5-1 depicts the geometry of the physical functional unit:

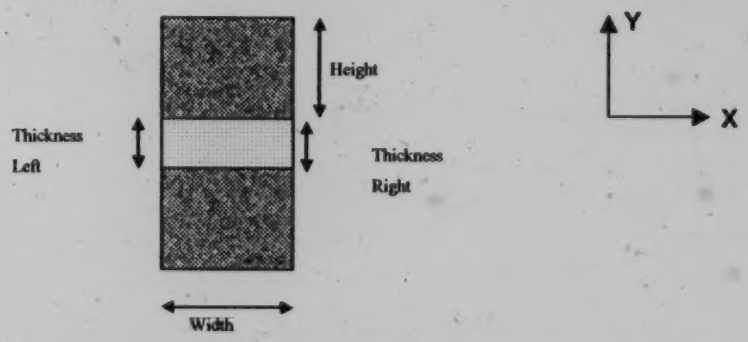

Figure 4-3-5-1 Dimensions of the physical functional unit

The thickness of the silicone disks of the three functional physical units is presented in Table 4-3-5-1 along with their standard deviations.

Specimen	Thickness Right (mm)	Thickness Left (mm)
1	7.1 + 0.1	6.2 + 0.04
2	3.8 + 0.6	6.8 + 0.3
3	7.7 + 0.02	7.7 + 0.02

Table 4-3-5-1 Thickness values of the physical functional unit

The physical functional unit was subjected to a bending force as many researchers have done to find the displacements of the vertebra. The test was performed using an arm made of aluminum that holds the upper wooden block. The load was applied at the end of the arm as shown in Figure 4-3-5-2. The lower wooden block was fixed, and the upper one was free to move.

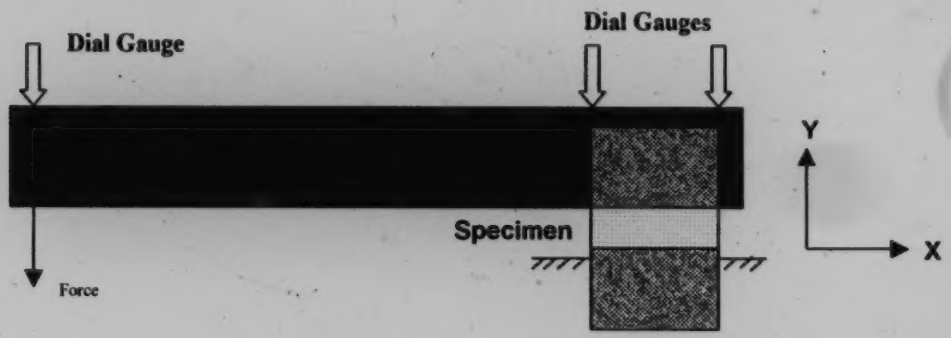

Figure 4-3-5-2 Bending force applied to the physical functional unit.

The maximum load applied to the specimens was 10 N; this load created a moment of 875 Nmm. The readings of the displacement were obtained from three dial gauges located at selected points. These points were along the line that is parallel to the right and left edges of the wooden block. Another dial gauge was located on the aluminum arm where the load is applied. In order to have repeatability, the test was performed three times for each loading condition.

The purpose of this study was to compare the experimental and computational results of the different models. Therefore, the physical functional unit was modeled in ANSYS in three dimensions with the same geometry and material properties of the experimental

model. Also, it was modeled in two dimensions using equivalent forces. The equivalent forces replaced the aluminum arm, and this is depicted in the figure below. The displacement results from ANSYS and from the experimental tests were compared. The results and the discussion about them are presented in the following Section 4.4.2. Raw data from the experimental tests are presented in Appendix 6.

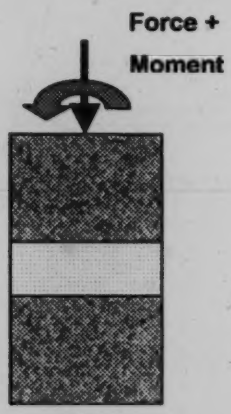

Figure 4-3-5-3 Equivalent forces of the physical functional unit

The next step was to build a sequence of functional units similar to the human spine. This was built as a physical model with 10 wooden blocks glued by silicone disks.

4.3.6 Physical Model

The physical model was built with equal thickness of silicone disks. This test used the Coordinate Measuring Machine made by Brown and Sharpe. The machine is designed to meet production needs, as well as accurate and economical verification of a variety of work pieces. The Coordinate Measuring Machine features a granite worktable that provides a stable, precise measuring and measuring surface, air bearings for frictionless movement of all axes, as well as, a bridge that moves in X, Y and Z directions. Fully counterbalanced columns infinitely adjust for varying probe weights [58]. Appendix 7 shows the specifications of the machine, and Figure 4-3-6-1 shows a picture of it.

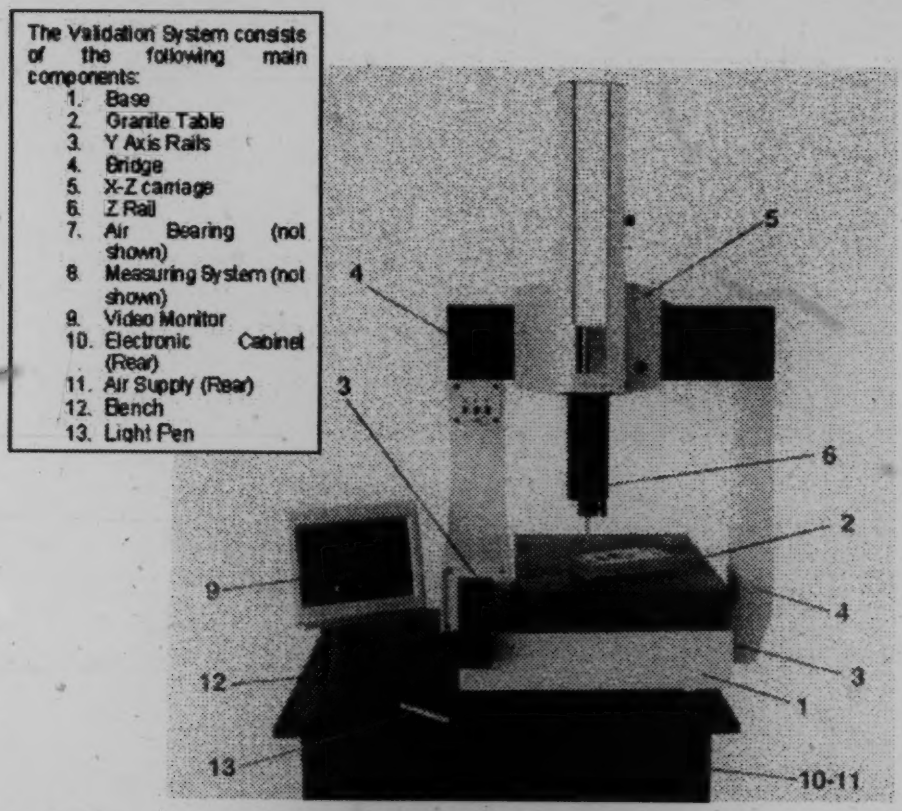

Figure 4-3-6-1 Coordinate Measuring Machine

To operate the machine, it is necessary to turn on the air supply and regulate the pressure to 55 ± 1 Psi. Pushing or pulling on the bridge leg, the X-Z carriage or the Z Rail accomplishes the movement of each axis through the measuring device. Stops are provided at both ends of the axes to prevent over-travel, and each axis is provided with a locking system. The physical model is located on the worktable of the machine using clamps in order to fix its position [58].

The first step, before measuring the displacement of the physical model, is to qualify the machine. For the qualifying test, a probe was used. It was a sphere of radius of 1/8" (3.175 mm). Once, the qualification is passed, the physical model is mounted on the table and aligned. The physical model is aligned with the reference system of the local coordinate axis. Special holders were built for the physical model to fix the ends and

apply the forces to any wooden block. The holders can be appreciated in Figures 4-3-6-2,3,4.

The physical model was tested twice to obtain repeatability and also confidence in the method used. The first time the displacements were measured using a needle that touched the vertices of the wooden blocks. To reach any target of the wooden block required great ability to coincide the needle with the vertices. These targets became difficult to reach because the vertices might have contained a small layer of silicone that was not noticeable. The vertices are points, and, therefore, the surface of contact has very low probability of being touched in the exact place. In addition, a steady hand is required for the bridge leg and rail in order to move the coordinate system to measure the displacement of the vertices of the blocks. Nevertheless, the test was done, and the results had big differences in the order of 60% in error difference.

Another method of measuring the displacements was used, instead it consisted of a spherical probe. The displacements expected with this procedure are around 8 mm; this value is given by the computational results using the properties of the experimental tests. The resolution of the coordinate measuring machine is in the order of 0.002 mm, and the accuracy is 0.006 mm. It was found that the probable error for the present experimental tests is in the order of 0.073 mm; this value was calculated in Section 4.2.

The measurement procedure consisted of touching the probe three times with the extension arms that are localized in each vertebra block. These arms protruding from the vertebrae blocks are the ones that provide the displacement after the application of the loads. The three measurements were done at the same height level of the protruding arms. This procedure was useful to obtain more accuracy with the measured displacements since the minimum values obtained were in the order of 0.1 mm.

The protruding arms were localized parallel to the Y-axis on the surface of each wooden block. The displacement results were divided into two regions: the right and left region; these can be seen in the next figures. The working plane was XY and the protruding arms were in the Z direction as shown in the figure of Appendix 8.
The physical model was subjected to different sets of loads such as horizontal, angle and combined forces. Figure 4-3-6-2 shows the horizontal forces applied to the physical

model. Figure 4-3-6-3 presents a combination of angle and horizontal forces (combined) and finally Figure 4-3-6-4 presents the angle forces causing a movement applied to the physical model.

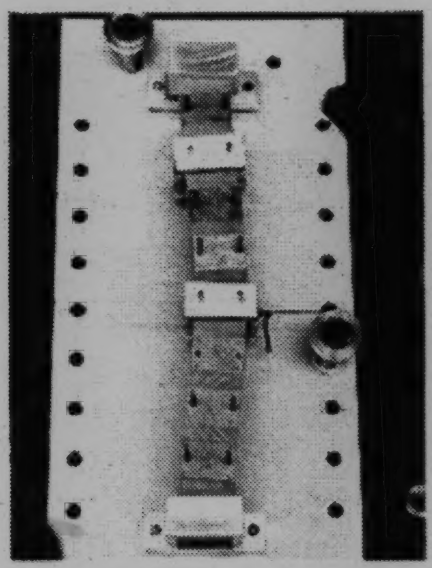

Figure 4-3-6-2 Horizontal force applied to the physical model

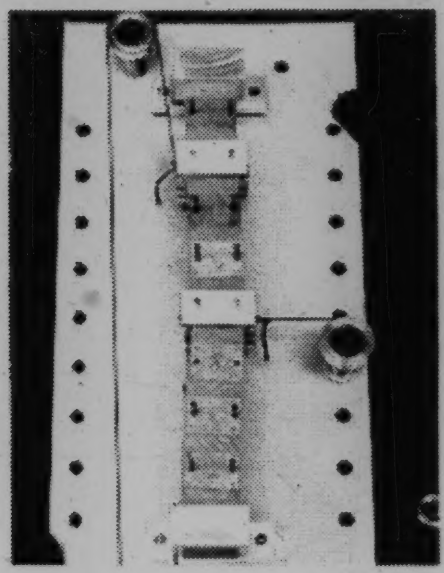

Figure 4-3-6-3 Combined forces applied to the physical model

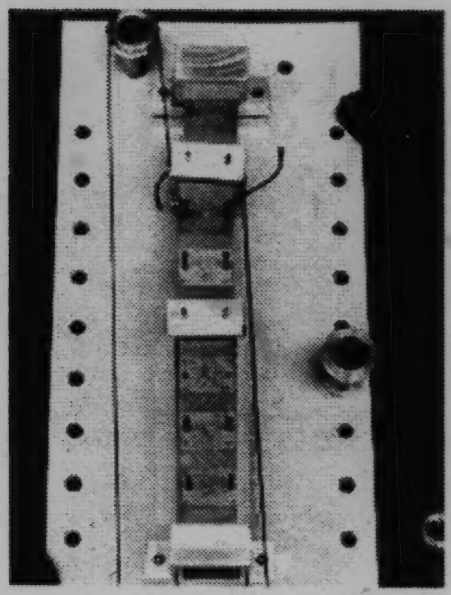

Figure 4-3-6-4 Moment applied to the physical model

There were nine loading cases applied to the physical model. The first case called *double horizontal* consisted of two pulling horizontal forces towards the right on block number 3 and to the left on block number 7. The second case called *single horizontal 7*, was a pulling force towards the left on block number 7. The third case called *single horizontal 3*, again, was a pulling force towards the right on block number 3. The fourth case called *horizontal 4* was another pulling force towards the right on block number 4. The numbering of the blocks is presented in Appendix 8.

The fifth case called *combined 7-4* was a horizontal pulling force towards the right on block number 4 and an angle pulling force of 95° on block number 7. The sixth case called *angle force 7* was an angular pulling force of 266° on block number 7. The seventh case called *moment 3* was a couple of angular pulling forces with 93 and 274° applied on block number 3. The eighth case called *moment 7* was a couple of angular pulling forces with 266 and 85° applied on block number 7. Finally, the ninth case called *combined 7-3* was a pulling horizontal force to the left on block 7 and an angular pulling force of 274° on block number 3.

The physical model was cured for 5 weeks. The maximum load applied was 19.6 N that produced a displacement of 7.1 mm in the X direction and 0.84 mm in the Y direction, when the load was horizontal. It was observed that the model has very small displacements when angle force and moment forces were applied. The maximum value of displacement obtained with a load of 19.6 N was in the order of 1.3 mm in the X direction and 0.3 mm in the Y direction. A discussion about the results between experimental and computational model appears in Section 4.4.3. Raw data from this experiment are presented in Appendix 8.

4.4 Computational Model

The objective of the present work was to use the constraint equation method in computational modeling. The experimental models were built in ANSYS using the mechanical properties and geometry from the experimental tests (Table 4-3-3-1) and/or literature. The modeling was two-dimensional using beams or CE for the vertebral body and a crossed spring set or plane elements for the intervertebral disc.

4.4.1 Modeling of the Intervertebral Disc

The experimental test results were set up to yield only two-dimensional coordinates. Thus, the three-dimensional silicone disk was represented by a simplified two-dimensional set of springs or plane elements.

The intervertebral disc is a combination of fluid and fibers; as a result, its mechanical behavior is diverse, supporting different loading conditions. The set of crossed springs constitute a simple way to obtain similar mechanical characteristics of the three-dimensional silicone disk. This model is able to support bending, compression, extension and shear loads. The search for an equivalent stiffness between the set of springs and the silicone disk is developed.

A model was established with four springs of different stiffnesses. Two vertical springs supports the compression and tension loads, two crossed ones support the shear loads and the set of four springs supports the bending loads. These four springs were

connected to a horizontal rigid body. Since it was an indeterminate problem, the finite element method was used to solve it. The unknowns for this problem were the stiffnesses of the four mentioned springs. Figure 4-3-1-1 depicts the crossed spring set model:

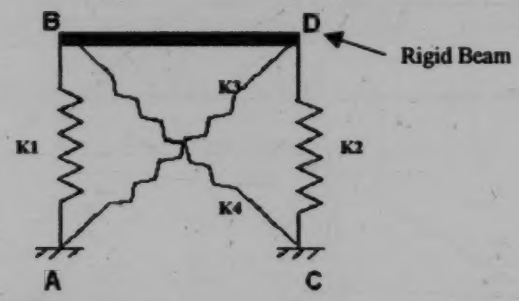

Figure 4-4-1-1 Crossed spring set model

To solve any mechanical problem (system of equations) using the FEM, the stiffness matrix, displacement matrix and load vector are defined [26A]. The stiffness matrix, [K], contains the stiffness values of each element of the problem. The displacement vector, {x}, contains the degrees of freedom of the problem. Finally, the load vector {b}, contains the loads that are applied to the problem. These entities are related by the following system of equations:

$$[K]\{x\} = \{b\} \qquad (4.4.1.1)$$

The present purpose was to model the intervertebral disc in two dimensions. Therefore, the model required an equivalent stiffness that had the same behavior as the silicone disk in two dimensions. As a consequence, the stiffness values of the spring model became the unknowns of the spring set problem. The solution of this problem was similar to the usual FEM procedure.

The method consisted of establishing the stiffness matrices for each spring as a link element. Once the stiffness matrices for each element were set, an assembly procedure was done for the whole system. Usually, FEM solves for displacements, but, in this particular case, it solved for the four springs' stiffnesses. The known data in the problem were the displacement and the forces applied to the model obtained from the silicone

disk model of the physical functional unit. Consider a simplified example with two degrees of freedom:

$$\begin{bmatrix} K_1 & K_2 \\ K_3 & K_1 \end{bmatrix} \begin{Bmatrix} X_1 \\ X_2 \end{Bmatrix} = \begin{Bmatrix} b_1 \\ b_2 \end{Bmatrix} \qquad (4.4.1.2)$$

Let us assume that K_1 is known, while K_2 and K_3 are unknown stiffnesses. X_1 and X_2 are the known displacements and finally, b_1 and b_2 are the known applied loads. Expanding the system, the resulting equations are:

$$\begin{aligned} K_1 X_1 + K_2 X_2 &= b_1 \\ K_3 X_1 + K_1 X_2 &= b_2 \end{aligned} \qquad (4.4.1.3)$$

The next step was to solve for K2 and K3. These values were derived from the known data:

$$\begin{aligned} b_1 - K_1 X_1 &= K_2 X_2 \\ b_2 - K_1 X_2 &= K_3 X_1 \end{aligned} \qquad (4.4.1.4)$$

The new system is:

$$\begin{aligned} K_2 &= \frac{b_1}{X_2} - \frac{K_1 X_1}{X_2} \\ K_3 &= \frac{b_2}{X_1} - \frac{K_1 X_2}{X_1} \end{aligned} \qquad (4.4.1.5)$$

In this way, the stiffness of each spring was found and its value was tested in models done in ANSYS with similar geometry of the physical functional units. The results from each case were satisfactory, because the same displacement values were obtained with the spring set model. The stiffness of each physical functional unit was different due to the different geometry of each model.

The second option to use was the plane element. This element was used to model the intervertebral disk. It was noticed that the plane element supports compression, tension, and shear when it is treated as plane stress element. As a consequence, the element was modeled in two dimensions having thickness. The element was tested against the three-dimensional modeling of the different physical functional units. It was found that it had similar results to the solid three-dimensional model of the silicone disk.

Figure 4-4-1-2 depicts the intervertebral disc using a plane element with 8 divisions per intervertebral disc. The total number of degrees of freedom of this element is 30, two degrees of freedom at each node.

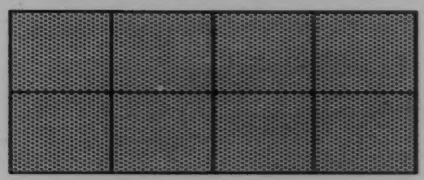

Figure 4-4-1-2 Intervertebral disc using plane elements

Since the present study found two options to model the intervertebral disc, a test was performed to see what option was better for the modeling of the spine. The test consisted of comparing the displacement results from the model using the spring set and the plane element. The model consisted of a series of blocks forming a 12-floor structure. Each floor was made of beams or constraint equations attached with the spring set or the plane element. The plane element used in the test had only one element; in other words, it was not meshed as is depicted in Figure 4-4-1-2. The results of this test are presented in the following table:

Case	Elements	# DOF	Mechanical properties	Max. Δx
1	Beams and spring set	228	K= 47 N/mm	83.8 mm
2	Beam and plane elem.	228	E= 2.28 N/mm^2	87.8 mm
3	CE and plane elem.	200	E= 2.28 N/mm^2	87.4 mm
4	CE and spring set	200	K = 47 N/mm	83.4 mm

Table 4-4-1-1 Comparison between different models using CE, springs and plane element

The intervertebral discs were modeled with equal thicknesses. The stiffness value was 47 N/mm for a thickness of 8 mm. The results from the four models using CE with plane element, CE with spring set, Beams with plane element and Beams with spring set were compared against the experimental models of the physical functional units (See Table 4-4-1-1). From these results, it was concluded that the spring set with a stiffness value of 47 N/mm and the model with the plane element and Young's modulus of 2.28 N/mm^2 has a similar behavior to the experimental model of the silicone disk. The silicone disk in the experimental model has 25 mm in thickness and the Young's modulus of 2.28 N/mm^2.

4.4.2 Computer Model of the Physical Functional Unit

A computational model with similar geometry to the experimental model was built. The intervertebral disc used the plane element or spring set and the vertebral body either beams or constraint equations. The model was tested for convergence and final displacements.

The physical functional unit was modeled in three dimensions using solid squared elements for the metallic arm, wooden blocks and silicone disk. The material properties used were found in literature for the case of the metallic aluminum arm and wooden blocks. The silicone properties were from the experimental tests in Section 4.3.4. The loading and constraint conditions were applied to the model as closely to the real test as possible.

In a similar manner, a two-dimensional computational model was built, but the loading conditions were the equivalent forces in three dimensions converted into two dimensions. In other words, the moment and the reaction loads were transformed into vertical forces applied to the surface of the wooden block. This was explained in Section 4.3.5. The percentage difference in displacement between the two computer models in three-dimensional with the two-dimensional case was in the order of 2%. The reference was the three-dimensional model, because it gave similar results to the experimental model.

The following figure presents the maximum displacement in Y direction for the physical functional unit one (FPU-1; see Table 4-3-5-1). The three dimensional case was under the application of the moment load and the two-dimensional case under the equivalent load. Figure 4-4-2-1 also presents the displacements of the experimental model. The results for the three models started with almost equal values, but as the load increased, the values from the experimental test diverged from the ANSYS values. The difference was explained because the ANSYS models had a perfectly linear behavior. In the experimental, test the silicone disk had geometrical irregularities, material property differences, different dimensions, not perfectly straight structure, and among others did not permit the perfectly linear behavior. Section 4.2 presented a discussion of the possible reasons of the difference between the experimental tests and the computational models.

The error difference between the experimental model and the three dimensional model was in the order of 10% and between the experimental and the two-dimensional case 2%. These percentages differences were considered acceptable for the analysis error in the present thesis.

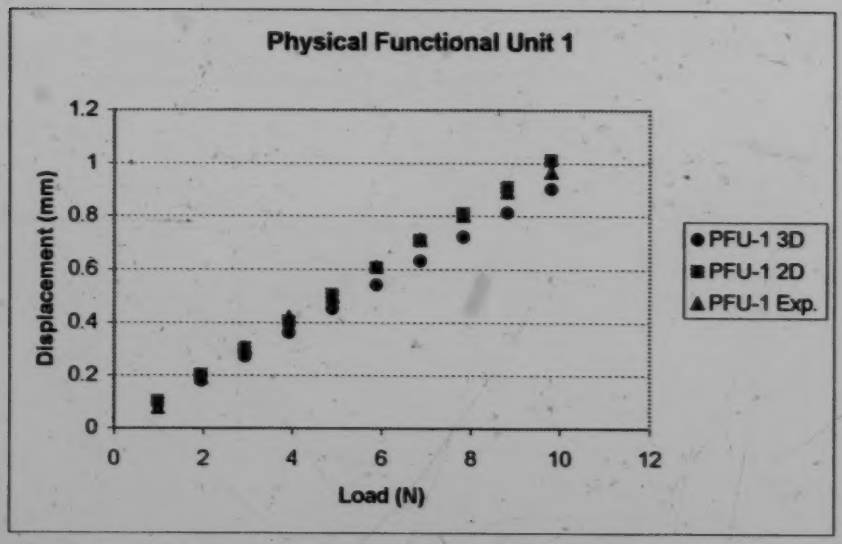

Figure 4-4-2-1 Displacement results from physical functional unit 1

Similarly, the displacements from the functional unit 2 (PFU-2; see table 4-3-5-1) were plotted. As is shown in Figure 4-4-2-2, the experimental results diverged from the models done in ANSYS as in the previous case. The percentage difference between the experimental model and the three-dimensional case was 16%, and 5% between the experimental model and the two-dimensional case. This percentage was greater than the ones for PFU-1. Therefore, another factor must be influencing in the results.

In fact, the geometry of the second model had imperfections in the thickness of the silicone disk, it was different in each face of the body. The probable error value for this specific case was 10.7%; this value is presented in Section 4.2. The irregularities in the silicone disk, plus the imperfections in geometry, caused the greater difference between the computational models and the experimental ones. However, this model was accepted because of the displacement results given by the two-dimensional ANSYS model; that agreed with the experimental test results as 95%.

Figure 4-4-2-2 depicts the maximum displacements of the physical functional unit two for the experimental and ANSYS models.

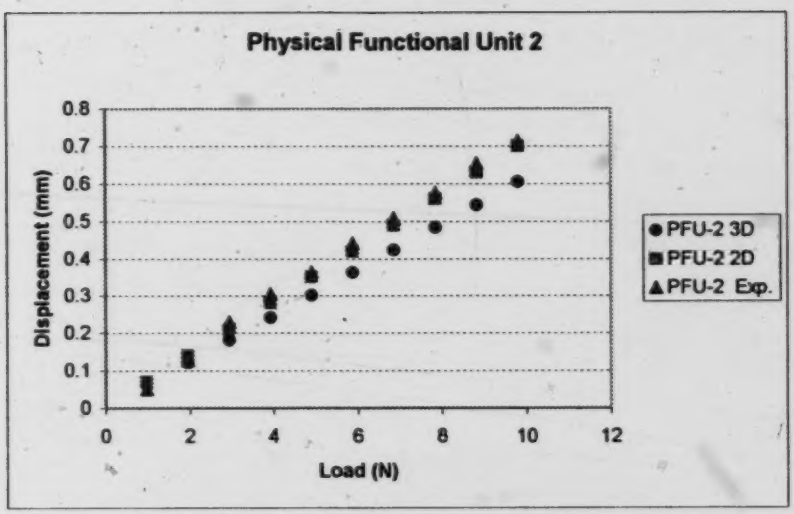

Figure 4-4-2-2 Displacement results from physical functional unit 2

Following the same procedure, the physical functional unit three (PFU-3; see table 4-3-5-1) was tested and modeled. The results in this case presented better convergence throughout the test. The error difference between the experimental test and the three-dimensional case was 8% and 3%. Figure 4-4-2-3 presents the maximum displacement for the physical functional unit three.

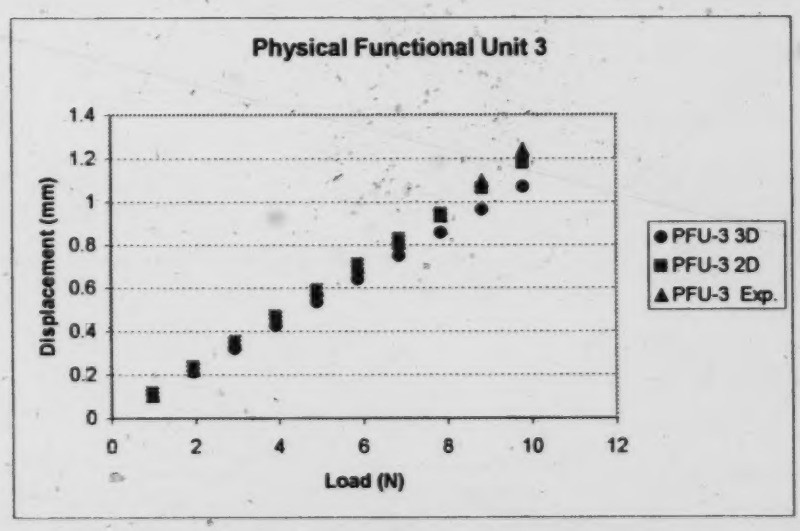

Figure 4-4-2-3 Displacement results from physical functional unit 3

PFU-3 is the model that had the same thickness over all its faces. The results from these specimens provided more confidence of the experimental tests. As a result, for the physical model, it was decided to use the same thickness in all the silicone disks.

In summary, the experimental and computational models had similar results. The overall error difference between the experimental and three-dimensional models is in the order of 11% and 4% between the experimental and the two dimensional model. As was mentioned at the beginning of this thesis, one of the purposes is to find a way of simplifying the three-dimensional model of the silicone disk into a two-dimensional model. Hence, the two-dimensional modeling fulfills this purpose.

It was found that when using constraint equations with a spring set or plane element in two dimensions, the results between the experimental and computational model have a small error. This error is in the order of 4%. Therefore, the two-dimensional modeling with the actual properties and elements was considered for the modeling of the physical model. Maximum displacements from ANSYS are presented in Appendix 9.

4.4.3 Computational Physical Model

The physical model was programmed, and it simulated the two dimensional response under different loading conditions. Likewise, the model was tested for convergence and for displacement results when using constraint equations and beams. The mechanical properties used in this modeling were the same as in the physical functional unit.

In the previous section, the displacements in the three and two-dimensional models were found for each physical functional unit. In the present study, a three-dimensional model was not necessary because the previous section showed that two-dimensional modeling better represents the experimental results.

The vertebral body was modeled as a set of rectangular boxes made up with 4 rigid beams or constraint equations. The intervertebral disc is modeled with the plane elements, as discussed in Section 4.4.1. The geometry of the computational model was based on the measurements of the physical model as a straight model. The constraints of the model were applied in the X and Y directions at both ends. The forces were

applied directly on the vertices of the rigid bodies equivalent to the one applied in the experimental test.

The nine arbitrary loading conditions mentioned in Section 4-3-6 were modeled in ANSYS. The displacements for each block were obtained and compared with the respective experimental case. The results, in general, fulfilled the expectations of the study (expected value 8 mm). The smallest error difference between the nine cases was obtained from the horizontal forces applied to the block number 4 (4th case). The displacement results given by the protruding arms on the wooden block at the right or left side were recorded. The following figures depict the results between the experimental and ANSYS models for the left case only because similar values are obtained with the right side. Figure 4-3-6-2 presents the loading picture of the horizontal 4 case.

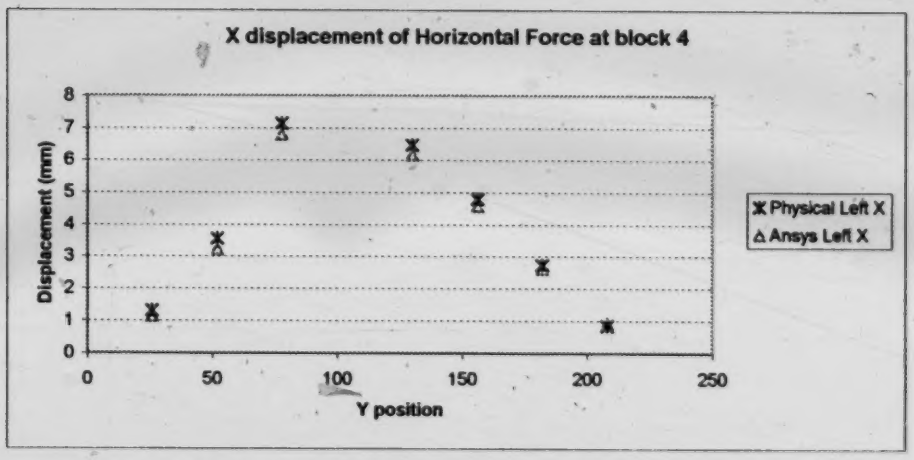

Figure 4-4-3-1 X displacement of the physical model case Horizontal 4

The error difference for the 4th case is in the order of 5% in the X direction while, in the Y displacement, the percentage difference was 14%. It was suspected that the Y coordinate had a bigger error than the X coordinate due to a small motion in the Y direction at the constrained ends. Similar results were obtained with the first five cases. The first five cases correspond to the application of the load in a horizontal and combined fashion. The horizontal force is along the X-axis for the local coordinate shown

in Appendix 8. The combined force represents one along the X-axis and the other almost parallel to the Y- axis.

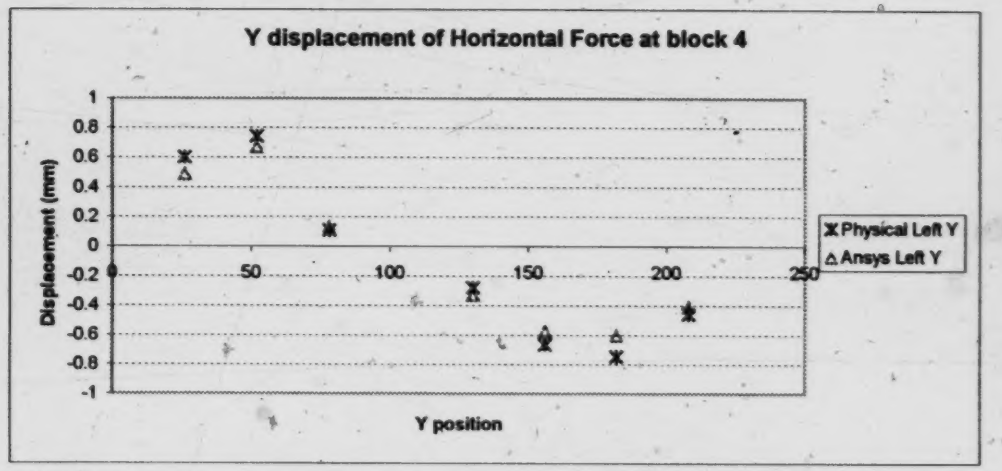

Figure 4-4-3-2 Y displacement of the physical model of case Horizontal 4

The last four cases had the angled forces and moment fashion forces applied to the blocks. The angle force is a load with an angle close to 90 or 270° measured anticlockwise. The values of these angles were between 90 or 270° ± 5°. The moment load has two angle forces applied to the same block in opposite directions. In other words, this loading reproduce force couple on the block. The values obtained from these four cases were far from what was obtained from the ANSYS models. The following figures depict these large differences.

According to the information given by the computational model, the displacements obtained from the last four cases were very small in the order of 0.3 to 1.3 mm. These values were difficult to measure using the experimental chosen procedure. As was mentioned previously, the ends of the physical model were not completely fixed; as a result, some displacement in the X and Y direction might happen during the tests. Consequently, the displacement results obtained by the experiment were bigger than the computational ones. Figure 4-3-6-4 presents the loading picture of the Moment 7 case:

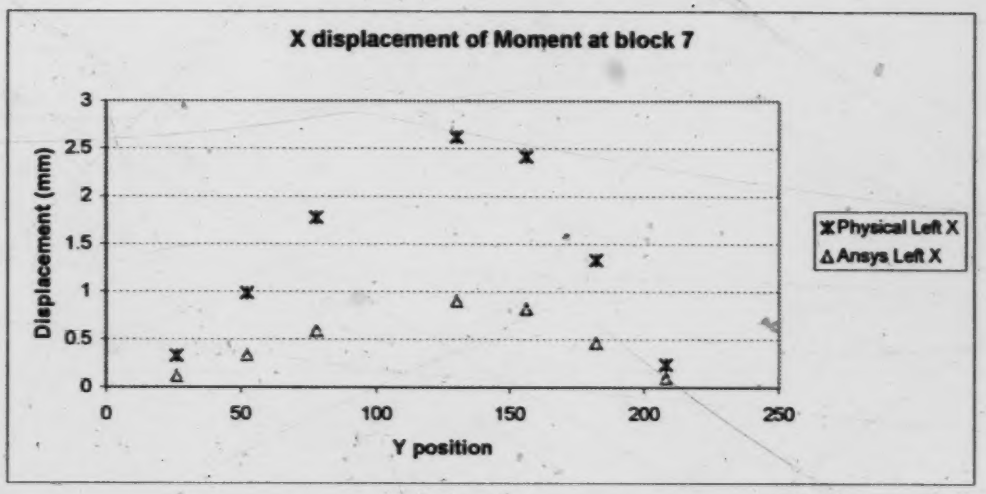

Figure 4-4-3-3 X displacement of the physical model of case Moment 7.

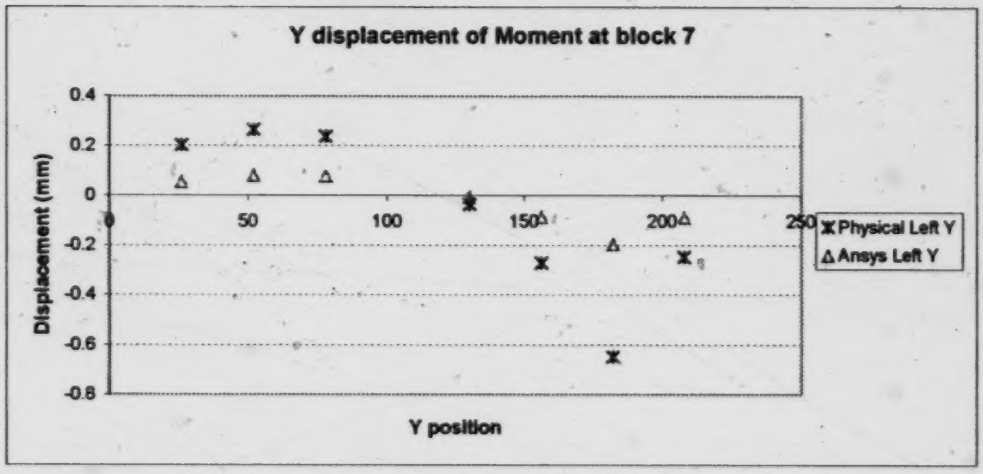

Figure 4-4-3-4 Y displacement of the physical model of case Moment 7

The maximum displacements from both models (experimental and computational) differed on average 67% in direction X. The possible reasons that could affect the resultant displacements were due to the irregularities in the silicone disks, imperfections in its geometry and in the overall geometry of the body and boundary conditions. The

following table is a summary of the nine cases with the individual percentage errors among the models. The computational results from this model are found in Appendix 10.

Case	X (Left) %	Y (Left) %	X (Right) %	Y (Right) %
Double Horizontal	9	15	8	16
Single Horizontal 7	10	21	11	23
Single Horizontal 3	6	16	6	14
Horizontal 4	5	14	5	16
Combined 7-4	15	8	16	9
Angle Force 7	83	59	36	89
Moment 3	65	57	65	65
Moment 7	65	72	64	66
Combined 7-3	12	32	11	390

Table 4-4-3-1 Percentage difference of the physical model

As is shown in the first five cases the mean value of the difference is 13%, which is inside the range of the percentage difference error accepted by this study. In contrast, the last four cases present a mean value of 77% in the X and Y direction.

4.4.4 Discussion

Since computer simulation is used in this thesis to create the spine model various problems related with geometry, boundary conditions and material properties appeared. These problems caused the simulation to yield inconsistent results. This was especially seen in the four last experimental cases (Section 4.3.6) and their correspondent computational cases (Section 4.4.3) of the physical model when the boundary conditions greatly affected the displacement results. To avoid such problems for the experimental model dimensions, geometry and silicone disks properties were measured carefully. These measurements were done in order to reproduce the experimental case in the simulation program as closely as possible.

The experimental tests used silicone. It was suitable at the point of stiffness for maintaining disc height between the wooden pieces and for maintaining elasticity while

applying the forces. The mechanical properties found from these tests agreed with the expected values from the ASTM information in Section 4.3.

The probable error study from Section 4.2, gave the maximum percentage error in which the experimental and computational tests should differ. The probable error of 11% was obtained, and it was less than the one expected (See Table 4-2-1). It was justified because some errors do not usually contribute to the final error in accumulative manner. In other words, some of the errors may act in different directions, and, hence, the error from one factor may cancel the error caused by another factor. Therefore, 4% more was added due to the internal and not counted errors. A total of 15% was established as the maximum error between the experimental and computational models for the present study.

The computational model in ANSYS was validated by experimental tests. The first validation was done with the intervertebral disc of the physical functional unit. The displacement results from these comparisons gave a percentage difference of 4% shown in Section 4.4.2 that, according to this study, is in the range of acceptance. The second validation was done with the displacement results of the physical model. Despite that fact that the last four cases did not match as closely did the computational predictions; the first five cases accomplished the expected displacements given by the computational modeling as shown in Table 4-4-3-1. The maximum expected displacement was 8 mm, and the maximum displacement obtained was 7.1 mm with a maximum percentage difference in 9% in the X direction (see Figure 4-4-3-1).

The intervertebral disc in the computational model was built using plane elements or a spring set. The stiffness of the spring set was computed using the finite element method as explained in Section 4.4.1. The stiffness values were found based on the properties of the silicone disk of the physical functional unit. In other words, the stiffness depended on the geometry (thickness and height) and material properties of the disk.

Intervertebral discs, vertebrae, ligaments and tendons are frequently modeled using elements, such as solids, planes or links. In order to obtain solutions from a model constructed with elements, it is required to mesh them. The meshing procedure creates more degrees of freedom in the system, and, therefore, computational time is increased.

Figure 4-4-4-1 shows a typical three-dimensional representation of an intervertebral disc, while Figure 4-4-4-2 show a simplified two-dimensional model. Both of these models exhibit a relatively large number of degrees of freedom.

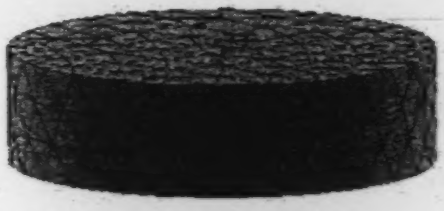

Figure 4-4-4-1 Intervertebral disc using solid elements

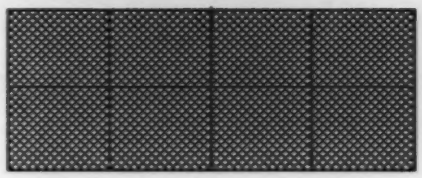

Figure 4-4-4-2 Intervertebral disc using plane elements

To decrease the number of degrees of freedom in the intervertebral disc, this thesis lead to the use of a two-dimensional spring set. Figure 4-4-4-3 depicts the intervertebral disc model using the spring set. There are only 8 degrees of freedom in this model.

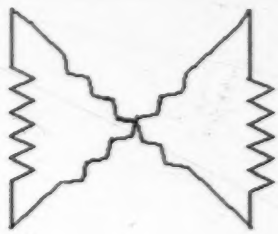

Figure 4-4-4-3 Intervertebral disc using spring set

The previous figures show the advantage of using the spring set in the modeling of the intervertebral disc due to the decrease in the number of degrees of freedom.

For modeling the vertebra, constraint equations are used in the present work to provide a new technique that decreased the number of degrees of freedom keeping the same accuracy in the calculations. The accuracy of the system was the same when using CE instead of the two-dimensional or three-dimensional elements. As a result, the CE technique also offers a substantial decrease in the computational time due to the great simplification in the model's geometry.

4.4.5 Thoracic Model

Modeling the spine is difficult due to its very complicated nature. A two-dimensional finite element model of the normal thoracic region in the frontal plane was built. The geometry of the region was obtained from Table 1-4-1-2 and the mechanical properties from Table 4-3-4-1. The thoracic region was chosen since it is where the majority of the scoliotic problem appears.

The model consisted of trapezoidal shapes that represented the vertebrae bodies built with constraint equations. The CE in the simulation program (ANSYS) appeared as lines that express the linear equations. These lines join the vertices of the rectangular intervertebral discs. Two horizontal lines appeared from the upper part of the trapezoidal shape, representing the transverse processes of the vertebra as is shown in Figure 4-4-5-1. Figure 4-4-5-2 presents a close view of the vertebral body formed by constraint equations in the ANSYS program.

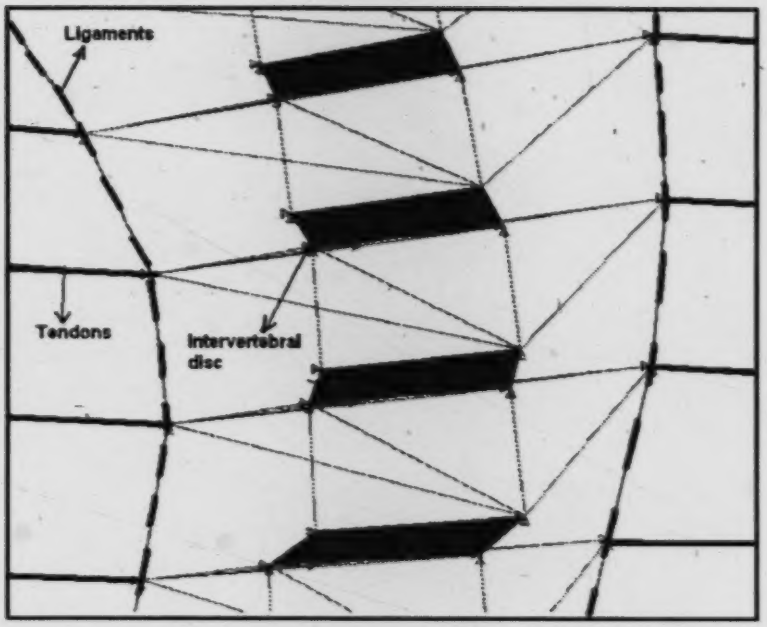

Figure 4-4-5-1 CE represented by lines that form the vertebral body

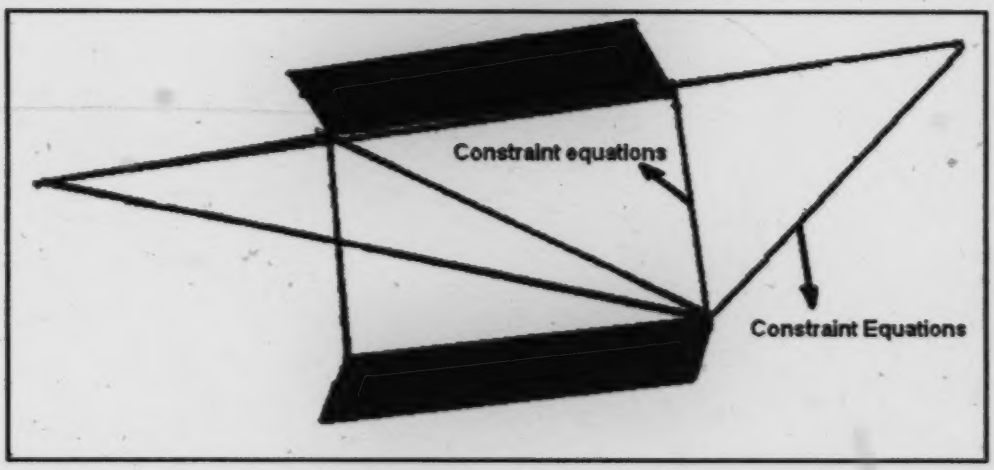

Figure 4-4-5-2 Vertebral body represented with constraint equations

The intervertebral disc was made of a plane element with one division in order to keep the number of degrees of freedom similar to the spring set while maintaining modeling

accuracy. The following figure shows the intervertebral discs as deformed rectangles in the computational model when using CE. The rectangles appeared without any link or joint because the model is using CE.

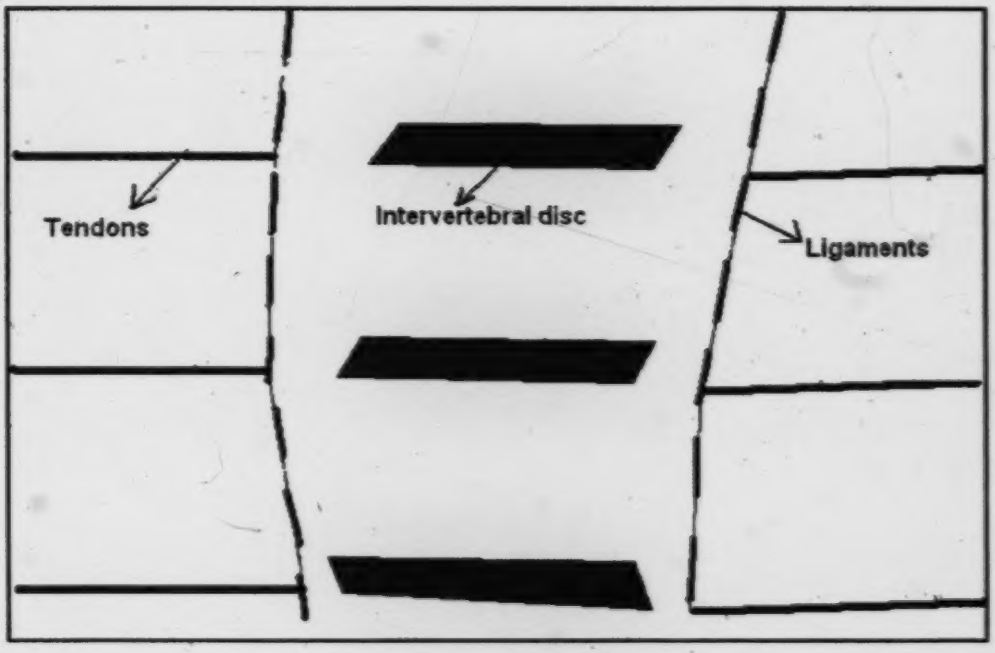

Figure 4-4-5-3 Intervertebral discs, ligaments and tendons

The above figure shows the horizontal thick elements represent the tendons, and the vertical dashed lines joining with the horizontal are the ligaments. The tendons and the ligaments are elastic bands, which was modeled with link elements mentioned in Section 4.4.1.

The complete model after the application of the load is shown in the next figure.

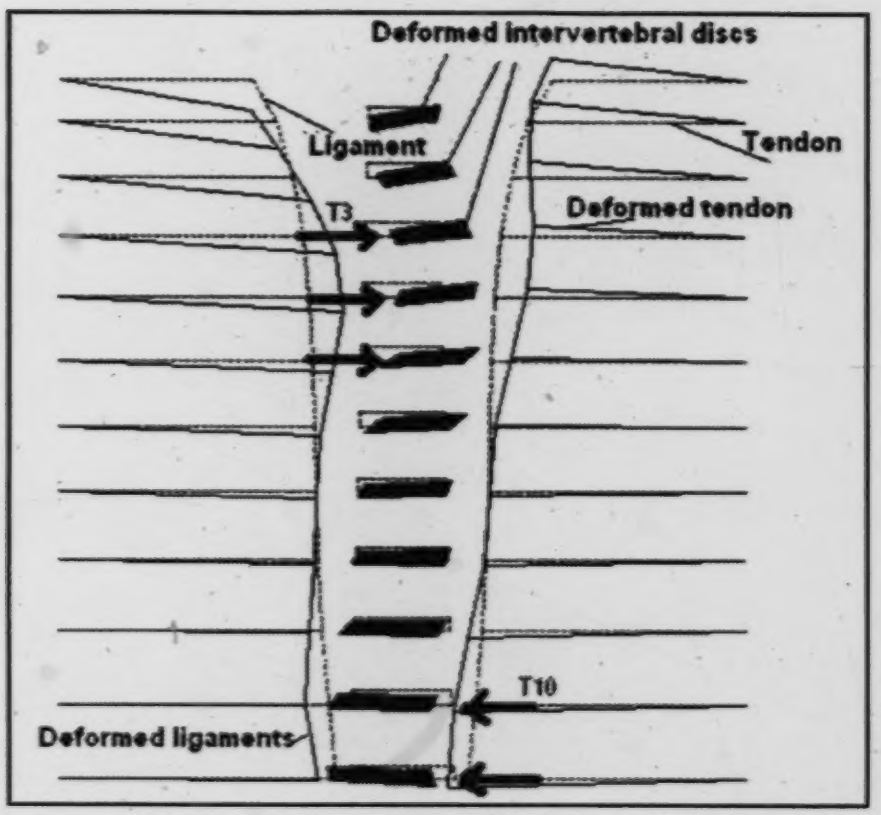

Figure 4-4-5-3 Thoracic model

The above figure shows a particular case of forces of 200 N in the X positive direction applied on T3 to T5 and a load of 150 N in the X negative direction on T10 and T11. The maximum displacement in the model obtained by these forces was 18 mm. According to information found in literature, a load up to 400 N is possible to apply to the spine and obtain corrections in the order of 60 to 70% depending on the severity of the curve. The values obtained by this model gave an idea that the spine is a very stiff element, and, therefore, to correct any deformation, it is necessary to apply forces in different places.

The presented model is a simplification of the thoracic spine in two dimensions. The model can support different loads, such as horizontal and vertical forces. To apply a moment force, it is necessary to use a couple, two parallel forces with apposing

directions and separated by a distance. From the results obtained after the application of loads, the only deformable element was the intervertebral disc form with a plane element. The vertebra constructed with constraint equations, behaved as a rigid body, and, hence, it stayed with no deformation as shown in Figure 4-4-5-1.

The constraint equations simplify the geometry of the models that uses rigid bodies and, hence, reduces the number of degrees of freedom and the computational time. The thoracic model in two dimensions contained a very low number of degrees of freedom compared with any model that used meshed elements. The number of degrees of freedom is about 472 with 59 elements. In the case of the model done by Steven Tong, the thoracic region had 2,136 elements and 12,816 degrees of freedom. Although it was done in three dimensions, the great number of elements and degrees of freedom that the model had is very noticeable.

The program was done with the possibility to be user defined. The geometry and the mechanical properties of the thoracic region can be changed. For instance, in the case of a scoliotic spine, it is possible to collect the geometrical and mechanical data of the thoracic region of the patient in the frontal plane as new input.

The results obtained from this computer model with constraint equations were compared against another one using only elements, and the displacement results for any loading condition were the same. With the CE, it is possible to conclude that constraint equations are a fast and easy way to replace rigid bodies and substantially reduce the computational time.

Chapter 5

5.1 Summary

One of the objectives of the present work was to validate the use of constraint equations to represent rigid bodies in the finite element method. The constraint equations relate the degrees of freedom of the points in the rigid body explained in Section 3.3. To find the constraint equations, three points of a rigid body were selected and subjected to displacements and rotations. The Euler matrix was used to generate the resultant equations. It was found that the constraint equations involved small angles; these angles were less than 10 degrees (see Section 3.3.1).

To establish the validation of these equations in the modeling of the spine, comparison tests of maximum displacements between computational and theoretical models were carried out, as discussed in Section 3.3.1 The validation process started with a simple frame problem composed of three elements. Two vertical beams with small stiffnesses and one horizontal beam with very high stiffness with respect to the vertical ones formed the frame problem. It was found that the horizontal element could be replaced by the constraint equations.

Once, the validation of these equations was done, it was established that the vertebral body of the spine would be modeled with constraint equations. The geometry of the vertebral body at the beginning was built as a rectangle; thereafter, it was changed to a trapezoidal shape that had, on average, geometrical values of the width and height of the vertebral body.

Another objective of this thesis was to validate the computational model by comparing the displacement results from the experimental test with those from the computational modeling, as presented in Chapter Four. This thesis did not attempt to use the experimental results to model the human spine. This thesis attempted to qualify and quantify the relationship between the silicone disks in three dimensions with a model of the intervertebral disc in two dimensions.

Takemura, et al.'s study (1999) simulated the spinal deformation associated with idiopathic scoliosis by applying different patterns of forces to qualify and quantify the scoliotic deformity. Following the same idea, four experimental models were built to find the properties of the silicone disk. Displacements from the experimental and computational model were recorded under different loading conditions. It was found that the experimental tests exhibited similar behavior to the computational ones presented in Section 4.4.3.

The intervertebral disc was modeled using silicone 732. The mechanical properties of silicone 732 were found by compression and shear tests. The results from these two tests were as expected lower values with respect to the ASTM experimental study. The mechanical properties of the silicone were compared against the intervertebral disc properties proved in Section 4.3.

Young's modulus of silicone 732 was 1.5 times less than the value of the intervertebral disc Young's modulus. On the other hand, shear modulus; compression stiffness and shear stiffness values were 8, 9 and 5 times less than the intervertebral disc properties respectively (see Table 4-3-4-1). This difference in the properties is justified due to the structure of the intervertebral disc. The intervertebral disc is capable to increase its properties a great amount under compression and shear forces and be similar or stronger than the vertebra.

Three models were built using silicone 732 as a disk between two wooden square pieces called a physical functional unit. Three similar models were built in ANSYS in order to compare their results with the experimental tests. The averages of the percentage differences for these cases were as follows: between the experimental and the three-dimensional models 11%, and for the experimental and two-dimensional models 4%, as calculated in Section 4.4.2.

Physical functional unit 2 (PFU-2) presented bigger differences with respect to the computational model due to geometry and material problems. The second specimen is the one that has a different thickness at each side of the frontal view (Table 4-3-5-1). Careful measurements found that each face in the experimental PFU-2 contained a different value in thickness. This showed why the 3-dimensional model built in ANSYS

with a symmetric and parallel thickness in each face gave a bigger percentage of difference with respect to the experimental models.

As was mentioned, the models built in three dimensions had bigger percentages of difference than to the experimental ones. It could be alleged to be a geometry and material problem. The three-dimensional model built in ANSYS has a perfect silicone disk while the experimental model, in its volume, contained some small bubbles, different thickness and irregular surfaces in its faces. Therefore, the three-dimensional model is more susceptible to having a larger error than the two-dimensional model.

The two dimensional model showed a closer behavior to the experimental model, because of its simplifications. The model of the silicone disk in two dimensions was a plane element, which used the average lengths and widths of the experimental models discussed in Section 4.4.4. In summary, the three physical functional units compared with the computational programs gave results inside the range of acceptance.

The physical model (ten blocks) had a higher probability of having different displacements than the computational model due to the increase in the number of blocks and disks. The physical model had irregularities in its silicone disks and straightness. Nevertheless, the results showed good values for the first five cases but not for the last four ones. For the first five cases, the mean value of the percentage difference is 13%, a value accepted in this study. In contrast, the last four cases present a mean value of 77%, as calculated in Section 4.4.3.

The last four cases of the physical model gave a clear idea of why the boundary conditions were not achieved as expected and the method used were not useful to measure very small displacements. As a result, the displacement results gave a large amount of variation between the experimental and computational models.

5.2 Conclusions

It is shown that an understanding of the mechanical modeling of the human spine plays and important role in the treatment of any spinal pathology. The start of a surgical planning model in two dimensions was done in the present study. However, a three-dimensional model would be a better representation of what is happening in the human spine.

To obtain constraint equations either in two dimension or three dimensions, the Euler rotation matrix is another way available instead of the geometrical analysis. However, for the three-dimensional case, the Euler rotation matrix is recommended instead of the geometrical analysis because it already has the sine and cosine involved.

The present work achieved the three objectives established for this thesis, namely (i) the use of constraint equations to represent the motion of the rigid body, (ii) the experimental displacement results have a maximum percentage difference with the computational model in the order of 15% and (iii) the modeling of the intervertebral disc done in two dimensions.

The human spine can be simplified using constraint equations because it only used certain selected points that are representative in the overall geometry. For example, in the case of the vertebral body, it was simplified as a trapezoidal shape with average values of end plates and heights. In the same manner, a point that joined the vertebral body using constraint equation represented the tip of the transverse processes.

Constraint equations are a new technique to replace the rigid body motion as well as decrease the number of degrees of freedom. The accuracy of the results obtained with CE are the same as if the modeling is using elements. The advantage of using CE is also noticeable in the decrease of the computational time used to solve the model.

Experimental specimens were useful to obtain the material properties of silicone 732, as well as to prove that the geometry of the silicone disk does not affect its material properties when using a plane element. Nevertheless, it is advised to use the spring set

instead to model the silicone disk, because it reduces more the number of degrees of freedom.

In the case of horizontal and/or combined forces, the displacements were values that could be measured easily by the coordinate measuring system procedure. On the other hand, in the last four cases, is the angle or moment forces were applied; the displacements obtained were very small compared with the previous ones. Therefore measurement difficulty appeared; lack of accuracy of the procedure and boundary conditions contributed to the big percentage differences.

The last four cases did not give the expected results, and it was mainly attributed to the possibility of movement of the block in the constraint holder when the load was applied. The clamps at the ends of the physical model were not perfectly constrained; thus, the physical model had the possibility to move in the Y direction. In addition, the geometry was added to the inaccuracy of the measurement as well as the straightness on the model.

The first five cases of the physical model showed an opposite situation to the last four cases. It gave the confidence to validate the computational model. It was found that in the modeling of the spine model either with the experimental case or the computational case the intervertebral disc parameters significantly affect the final displacement solution. These parameters are the Young's modulus and the height of the disc.

The computational model was successfully validated using the physical model. It is concluded that the importance of having the right boundary conditions, accurate geometrical dimensions, the right material properties and the correct measurement method contributed to the final results when comparisons between experimental and theoretical or computational models are done.

The final product is a program that can use different input data of geometrical values, mechanical properties and load values with very small computational time making it easy to study each particular spine problem.

5.3 Future Work

Spinal deformity in idiopathic scoliosis involves not only vertebral deformation in the frontal plane but also rotation of the vertebral bodies and a decrease in thoracic kyphosis. It has been shown that three kinds of deformity produce the three-dimensional Scoliotic deformities. Hence, a three-dimensional model is required to better study the scoliotic problem.

As was mentioned in Chapter One, Scoliosis is a lateral curvature of the spine associated with vertebral rotation. Therefore, it involves a three-dimensional modeling to study the problem. It is recommended to create a three-dimensional model, in order to analyze the rotational problem of the vertebrae. The two-dimensional program can be used as a preliminary short study of the scoliotic problem in a patient.

The present work is done in the linear range of elasticity using constraint equations to model the spine. A future study in a non-linear field using constraint equations or any other method would allow modeling the three-dimensional physiological movements of the spine with accuracy. This new procedure would also greatly reduce the number of elements that cause long computational time.

A suggested approach for the non-linear problem is the use of substructuring or condensation derivation procedures. These procedures are used to simplify the analysis of very large in size problems with minimal computer resources. The substructuring method considers a condensed stiffness matrix that only retains those degrees of freedom that are necessary to connect the body to the adjoining elements.

The use of the spring set is advised in the present thesis because it greatly reduces the number of degrees of freedom of the intervertebral disc model. However, it was not used for the final thoracic model because of the problem of variation in stiffness due to the geometry and the loading pattern. A further analysis in the stiffness values is advised.

Since the constraint equations are mathematical expressions, they can be implemented in any computer language to create a simulator that medical doctors can use in their pre-operative procedures.

The possibility to create a spine model using synthetic vertebrae attached with silicone disks would allow observing the pattern of motion of the spine in three dimensions. This model would help to clearly identify the intervertebral shifts that are hard to reproduce in a computer model.

6.1 References

1. ANSYS *User's Manual Ansys Revision 5.6.1,* USA, 1999

2. Arkin, Alvin. The Mechanism of the Structural Changes in Scoliosis. *The Journal of Bone and Joint Surgery.* Vol 31 A, Num 3, pp 519-28, 1949

3. Arkin, Alvin. The Mechanism of Rotation in Combination with Lateral Deviation in the Normal Spine. *The Journal of Bone and Joint Surgery.* Vol 32 A, Num 1, pp 180-88, 1950

4. ASTM, *Science and Technology of Building Seals, Sealants, Glazing. And Waterproofing STP 1168.* Charles J. Parise, editor. USA, 1991

4A. ASTM, *Science and Technology of Building Seals, Sealants, Glazing. And Waterproofing: 5th volume STP 1271.* Michael Lacasse, editor. USA, 1996

5. ASTM Standard Test Methods for Rubber Property – Compression Set. Designation D395-98. *Annual Book of ASTM Standards.* Vol 14.02, 1999

6. Avallone and Baumeister III. *Mark's Standard Handbook for Mechanical Engineers 9th edition.* McGraw-Hill Book Company, USA, 1978

7. Berkson et al, Mechanical Properties of Human Lumbar Spine Motion Segments – Part II: Responses in Compression and Shear; Influence of Gross Morphology. *Journal of Biomechanical Engineering.* Vol 101, pp 53 –7, 1979

8. Berry, J. Moran J. et al. A Morphometric Study of Human Lumbar and Selected Thoracic Vertebrae. *Spine.* Vol 12 Num 4, pp 362-67, 1987

9. Brown, T. Hanson, R. And Yorra, A. Some Mechanical Test on the Lumbrosacral Spine with Particular Reference to the Intervertebral Discs. *Bone Joint Surg.* , 39 A ,pp 1135 ,1957

10. Chazal et al, Biomechanical Properties of Spinal Ligaments and Histological Study of the Supraspinal Ligament in Traction. *J. Biomechanics.* Vol 18, No 3 pp 167-76, 1985

11. Clayton, Thomas L. *Taber's Cyclopedic Medical Dictionary Edition 16th Illustrated.* F. A. Davis Company. USA, 1989

12. Dansereau, J., Labelle H., Bellefleur C. Evaluation of the Immediate Effect of Boston Brace on Scoliotic Deformity by Means of Spinal and Rib Cage 3-D Reconstructions. *Orthopaedic Research Society, 37th Annual Meeting.* 1991

13. Dietrich, M., Kedzior K., Zagrajek T., A Biomechanical Model of the Human Spinal System, *Proc. Instn. Mech. Engrs.* Vol. 205, pp 19-26, 1991

14. Dumas, G. A. Some Geometrical Parameters of Spinal Facets. *Personal communication.* Queen's University

15. Duke, Kajsa. *The Design of Instrumentation for Force Measurement During Scoliosis surgery.* M. Sc. Thesis, University of Alberta. Canada, 2001

16. Esses, Stephen I., *Textbook of Spinal Disorders,* J. B. Lippincott Company, Philadelphia, 1995.

17. Etter, D.M. *Structured Fortran 77 for Engineers and Scientist 3rd editon.* The Benjamin/ Cummings Publishing Company, Inc. USA, 1990

18. Galante, J. Tensile Properties of the Human Lumbar Annulus Fibrosis. *Acta Orthop. Sand,* 100 [Suppl], 1967

19. Goel, K., Weinstein J. , *Biomechanics of the Spine: Clinical and Surgical Perspective,* CRC Press, Inc, Boca Raton, Florida, 1990.

20. Goldstein, Herbert. *Classical Mechanics 2nd edition.* Addison Wesley. USA, 1980

21. Howard, S. *Principles and Techniques of Spine Surgery.* Williams & Wilkins Co. USA, 1998

22. Kapandji, I. A., *The Physiology of the Joints,* Churchill Livingston, Edinburgh London and New York, 1974

23. King, H.A., Moe J.H., Bradford D. S. The Selection of Fusion Levels in Thoracic Idiopathic Scoliosis. *J. Bone Joint Surg.* Vol 56 A, pp 1302-13, 1983

24. Labelle, H et al. Three-dimensional Effect of the Boston Brace on the Thoracic Spine and Rib Cage. *Spine.* Vol 21, Num 1 pp 59-64, 1996

25. Lavaste, F., Skalli W., Robin S et al. Three-dimensional Geometrical and Mechanical Modelling of the Lumbar Spine. *J. Biomechanics.* Vol 25, Num 10, pp 1153-64, 1992

26. Moaveni, Saeed. *Finite Element Analysis Theory and Application with ANSYS.* Prentice Hall, USA, 1999

26A. Fyfe, Ken . *Finite Element Analysis Notes, MECE 563.*University of Alberta,1999

27. Mow and Hayes. *Basic Orthopaedic Biomechanics,* Lippincott – Raven Publishers, Philadelphia New York, 1997

28. Myklebust, J. Pintar F. Yoganandan N. et al. Tensile Strength of Spinal Ligaments. *Spine* Vol 13 Num 5, pp 527-31, 1988

29. Panjabi, M.M., Brand R.A., White A.A. Mechanical Propertied of the Human Thoracic Spine as shown by Three-Dimensional Load-Displacement Curves. *J. Bone and Joint Surgery* Vol 58 A, pp 642, 1976

30. Panjabi, M.M., Brand R.A., White A.A. Three-Dimensional Flexibility and Stiffness Properties of the Human Thoracic Spine. *J. Biomechanics* Vol 9, pp 185-92, 1976

31. Panjabi, M., Takata K. Goel V, et al. Thoracic Human Vertebrae Quantitative Three-Dimensional Anatomy. *Spine*. Vol 16 Num 8, pp 888-901, 1991

32. Panjabi, M, Goel, Taketa. Human Lumbar Vertebrae Quantitative Three Dimensional Anatomy. *Spine*. Vol 17 No 3 pp 299-306, 1992

33. Ponsetti, I. Pedrini V. And Dohrman, S. Biomechanical Analysis of Intervertebral Discs in Idiopathic Scoliosis. J. Bone Joint Surg., Vol 56 A, 1973

34. Pope, M., Stokes I., Moreland M., The Biomechanics of Scoliosis, *CRC Critical Reviews in Biomedical Engineering*, Vol. 11, Issue 3, pp 157-88, 1984

35. Popov, Egor. *Engineering Mechanics of Solids*. Prentice Hall, USA, 1990

36. Puno, R.M., Mehta S., Byrd III A. Surgical Treatment of Idiopathic Thoracolumbar and Lumbar Scoliosis in Adolescent Patients. *Spinal Deformities* Vol 25, number 2, pp 275-86, 1994

37. Roaf, Robert. Rotation Movements of the Spine with Special Reference to Scoliosis. *The Journal of Bone and Joint Surgery*. Vol 40 B, Num 2, pp 312-32, 1958

38. Roaf, Robert, The Basic Anatomy of Scoliosis. J. Bone Joint Surg., Vol 48B, pp 786, 1966

39. Roark, R., Young W. *Formulas for Stress and Strain 5th editon*. McGraw-Hill Book Company, USA, 1975

40. Schlenzka, D., Poussa M. Muschik M. Operative Treatment of Adolescent Idiopathic Thoracic Scoliosis. *Clinical Orthopaedics and Related Research*. Vol 297, pp 155-60, 1993

41. Schultz, Albert B. Mechanics of the Human Spine. *Applied Mechanics Reviews*. Vol 27, pp 1487-97, 1974

42. Shultz et al. Mechanical Properties of Human Lumbar Spine Motion Segments – Part I: Responses in Flexion, Extension, Lateral Bending and Torsion. *Journal of Biomechanical Engineering*. Vol 101 pp 46-52, 1979

43. Schultz, Albert B. Biomechanical Factors in the Progression of Idiopathic Scoliosis. *Annals of Biomedical Engineering*, Vol. 12 pp 621-30 , 1984

44. Schultz, A., Galante J. A Mathematical Model for the Study of the Mechanics of the Human Vertebral Column. *J. Biomechanics*. Vol 3, pp 405-16, 1970

45. Scoles et al. Vertebral Body and posterior Element Morphology: The Normal Spine in Middle Life. *Spine* Vol 13 No 10, pp 1082-86, 1988

46. Skalli et al. A Biomechanical Analysis of Short Segment Spinal Fixation Using a Three Dimensional Geometric and Mechanical Model. *Spine*. Vol 18 No 5, pp 536-45, 1993

47. Subbaraj, K., Ghista D.N., Viviani G.R.. Presurgical Finite Element Simulation of Scoliosis Correction. *J. Biomed. Eng*. Vol 11, pp 9-18, 1989

48. Suwito et al. Geometric and Material Property Study of The Human Lumbar Spine using Finite Element Method. *Journal of Spinal Disorders*. Vol 5 No 1 pp 50-9, 1992

49. Takemura, Y. Yamoto H. Tani T. Biomechanical Study of the Development of Scoliosis, Using a Thoracolumbar Spine Model. *Journal of Orthopaedic Science*. Vol 4, pp 439-45, 1999

50. Tong, Steven. *A Mechanical Model of Normal Human Spine*. M. Sc. Thesis, University of Alberta. Canada, 1999

51. Tortora, G., Grabowski S. *Principles of Anatomy and Physiology 8th edition*. Harper Collins College Publishers. USA, 1996

52. Viviani, G.R., Ghista D.N., Lozada P. J. et al. Biomechanical Analysis and Simulation of Scoliosis Surgical Correction. *Clinical Orthopaedics and Related Research*. Num 208, pp 40-47, 1986

53. White, A. A. Kinematics of the Normal Spine as Related to Scoliosis. J. Biomech, Vol 4, pp 405, 1971

54. White, A. A. and Panjabi M.M. *Clinical Biomechanics of the Spine – 2nd Edition*. J.B. Lipincott Co. USA, 1990

55. Worthmann, W., Arnold G., *Mechanical Recovery Properties of Human Tendons*, Abteilung F\r Anatomie, Germany, pp 455-56, 1971

56. Yoganandan et al, Finite Element Applications in Human Cervical Spinae Modeling. *Spine*. Vol 21 No 15 pp 1824-34,1996

57. Zatsiorsky, Vladimir. *Kinematics of Human Motion*. Human Kinematics. USA, 1998

58. Coordinate Measuring Machine, Coordinate Measuring System Manual, 1986

Appendix 1

Nomenclature of the geometry of the vertebrae

UE	upper end plate
LE	lower end plate
PD	pedicle
SP	spinous process
SC	spinal canal
PI	pars interarticularis
VB	vertebral body
W	width
A	area
D	depth
H	height
I	inclination
t	transverse place
p	posterior
IFPD	inferior facet pedicle distance
IFMPL	inferior facet mid pedicle length
PL	pedicle length
HBF	height between facets
LV	length of the vertebra

Name	T1	T2	T3	T4	T5	T6	T7	T8	T9	T10	T11	T12	L1	L2	L3	L4	L5
UE-W	24.5	24.9	24.6	24.5	24.9	26.2	27.8	29.5	30.6	31.9	34.9	39	41.2	42.6	44.1	45.8	47.3
UE-D	18.5	19.6	22.7	23.3	24.3	26	27.4	27.9	29.3	30.5	31.9	32.8	34.1	34.9	35.2	35.5	34.7
LE-W	27.8	27.4	25.9	26	27	28.2	29.1	30.5	33	35.4	39.1	42.1	43.3	45.5	48	49.5	49.4
LE-D	19.7	21.6	23.3	24.5	25.8	26.9	28.5	29.4	31	31.6	31.8	33.4	35.3	34.9	34.9	33.9	33.2
VB-Hp	14.1	15.6	15.7	16.2	16.2	17.4	18.2	18.7	19.3	20.2	21.3	22.7	23.8	24.3	23.8	24.1	22.9
UE-A	300	333	373	381	426	483	547	605	678	727	842	954	1067	1130	1104	1239	1237
LE-A	376	398	412	444	495	552	603	664	755	834	945	1024	1117	1197	1200	1273	1218
UELi(deg)	0.8	1.7	2.4	1.5	2.1	2.1	1.6	1.3	0.9	0.5	2.7	2.2					
LEli(deg)	3.9	1.8	2.1	2	1.8	2	2.3	1.2	1.2	2.2	1.8	2					
SC-W	21.8	19.5	18.3	17	17.1	17.3	17.3	17.7	17.9	18.2	19.4	22.2	23.7	23.8	24.3	25.4	27.1
SC-D	16.4	15.3	15.9	16.2	16.3	16.5	16.1	15.9	15.7	15.5	16	18.1	19	19.2	17.8	18.8	19.7
SC-A	213	200	189	192	201	206	199	194	200	202	220	280	320	281	280	280	339
PD-W	8.2	8.4	7	5.5	6.2	6	6.5	6.7	7.6	8.3	8.8	8.8	8.8	8.3	10.2	14.1	18.8
PD-H	9.3	11.1	11.8	11.9	11.2	12	11.8	12.5	13.9	14.7	16.9	16.5	15.9	15	14.4	18.5	19.8
PD-A	52.2	46.3	38.1	32.5	31.6	3.5	36.8	43.8	52.3	64.8	88.4	90.9	88.8	83.8	84.1	107.8	151.3
PDIa(deg)	28.1	28.9	22.5	21.8	20.2	19.4	23.4	22.5	19.3	14.4	12.9	8	14.5	14.2	18.5	18.8	24.8
PDIt(deg)	4.6	16.5	8.1	6.4	8.6	7	10.9	12.1	8.3	6.8	8.9	4.8	2.3	3.3	2.9	4.8	5.2
SP-L	50.1	52.1	51.7	51.1	52.1	53.8	50.5	52.8	51.3	49.3	45.6	47.4	67.7	71.7	71.7	70.1	68.3
TP-W	75.3	69.4	60.8	56.9	61.1	61.3	60.4	59.9	59.3	58.4	52.2	46.9	71.2	76.1	85.7	79.4	92.5
IFP-D	11.9		12.8			14.5			15			18.8	22		23.5		21.4
IFMPL	16.3		18.4			20			21.3			28.5	29.5		30.5		30.1
PL	7.2		7.7			10.1			11.5			10.1	9.9		9.3		8
HBP		31.7					34					45.4	47.4	45	48.3	48.8	41.9
LV		64.1					63.9					73.4	76.9	85	85.8	83.4	74.1

Based upon data from:
Berry, et all (7), Panjabi, et all (28)
Scales et all (48)
Berry, Moran, Berg and Steffe (7)
Panjabi, Goel, Oxland, et all (28A)

Table 1-1 Geometry of the Vertebra
(Different sources)

Appendix 2

Geometrical Analysis of Constraint Equations

The purpose of this procedure is to find the X and Y coordinates of the unknown points of the plane. It uses three points called: Point 1, Point 2 and Point 3.

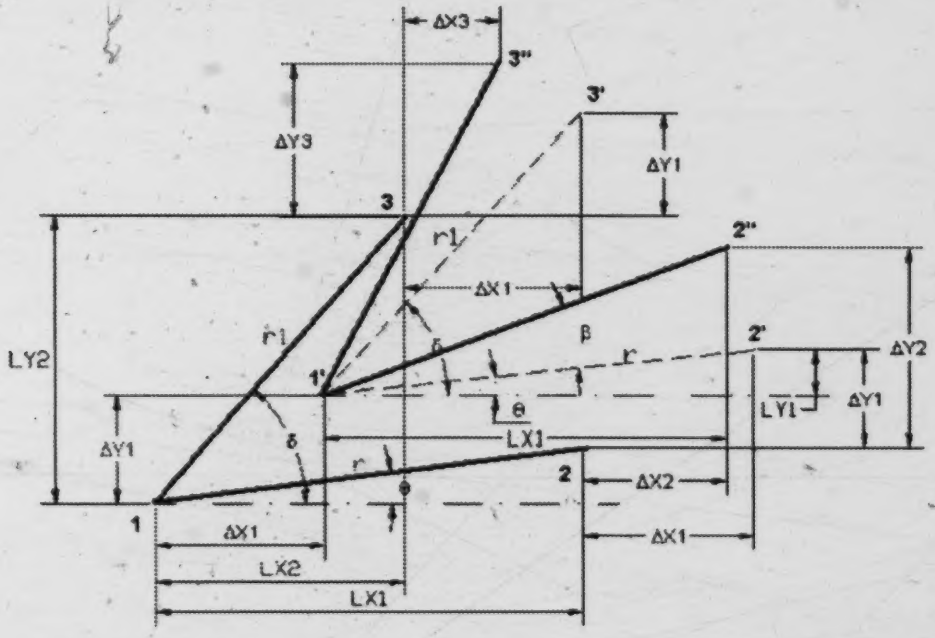

Two lines join the selected three points in the plane forming an angle. The vertex of the angle is point number 1 and it is about this point the rotation was done. The initial coordinates of points 1,2 and 3 ($P_1(X_1,Y_1)$, P_2 (X_2,Y_2) and P_3 (X_3,Y_3))are known as well as the angle respect to the horizontal line θ

Distances between the points were determined using their coordinates. The lengths of r and r_1, were determined using Pythagoras theorem

$$LX_1 = X_2 - X_1$$
$$LY_1 = Y_2 - Y_1$$
$$LX_2 = X_3 - X_1$$
$$LY_2 = Y_3 - Y_1$$

$$\rightarrow$$

$$r = \sqrt{(LX_1)^2 + (LY_1)^2}$$
$$r_1 = \sqrt{(LX_2)^2 + (LY_2)^2}$$

The angle θ was found using the geometry of the points 1 and 2. Similarly the angle δ was found using points 1 and 3.

$$\theta = \tan^{-1}\left(\frac{LY_1}{LX_1}\right)$$
$$\delta = \tan^{-1}\left(\frac{LY_2}{LX_2}\right)$$

$$Cos(\theta + \beta) = \frac{\overline{1'A}}{r} \quad ,then$$

$$\overline{1'A} = r\cos(\theta + \beta)$$

$$\overline{AB} = \overline{1'B} - \overline{1'A} = LX_1 - r\cos(\theta + \beta)$$

The X displacement for Point 2 is:

$$\Delta X_2 = \Delta X_1 - \overline{AB}$$

$$\Delta X_2 = \Delta X_1 - (LX_1 - r\cos(\theta + \beta))$$

$$\Delta X_2 = \Delta X_1 - LX_1 + r\cos(\theta + \beta)$$

$$\sin(\theta + \beta) = \frac{\overline{2''A}}{r} \rightarrow \overline{2''A} = r\sin(\theta + \beta)$$

The next step was to find Y' and then the X coordinate

$$Y' = \overline{2''A} - LY_1$$

$$\Delta Y_2 = \Delta Y_1 + Y'$$

$$Y' = r\sin(\theta + \beta) - LY_1$$

In the expression for ΔY_2, above, substitute the values for Y' and ΔY_1

$$\Delta Y_2 = \Delta Y_1 + r\sin(\theta + \beta) - LY_1$$

Finally the value of ΔX_3 is found from ΔX_1 and the lengths of X

$$\cos(\delta + \beta) = \frac{LX_1}{r_1}$$

$$LX_4 = r_1 \cos(\delta + \beta)$$

$$\Delta X_3 = \Delta X_1 + LX_4 - LX_2$$

Looking for the Y coordinate:

$$\sin(\delta + \beta) = \frac{\overline{3''E}}{r_1} \rightarrow \overline{3''E} = r_1 \sin(\delta + \beta)$$

$$\overline{3'D} = LY_2 = \overline{CE}$$

$$\overline{3''C} = \overline{3''E} - \overline{CE}$$

$$\overline{3''C} = r\sin(\delta + \beta) - LY_2$$

Substitute 3"C into the following expression:

$$\Delta Y_3 = \Delta Y_1 + \overline{3''C}$$

$$\Delta Y_3 = \Delta Y_1 + r_1 \sin(\delta + \beta) - LY_2$$

The displacement of the point 3 in X and Y coordinate are:

$$\Delta X_3 = \Delta X_1 + r_1 \cos(\delta + \beta) - LX_2$$

$$\Delta Y_3 = \Delta Y_1 + r_1 \sin(\delta + \beta) - LY_2$$

Appendix 3

Constraint Equations in Two dimensions with Rotations

Once the range of small angles is set the last equations from Appendix 2 can be simplified.

$$\Delta X_3 = \Delta X_1 + r_1 \cos(\delta + \beta) - LX_2$$

$$\Delta Y_3 = \Delta Y_1 + r_1 \sin(\delta + \beta) - LY_2$$

The first step is to expand each equation in order to obtain the sine and cosine individually. Start with the expression for the X coordinate of point number three

$$\Delta X_3 = \Delta X_1 - (X_3 - X_1) + r_1(\cos\delta\cos\beta - \sin\delta\sin\beta)$$

Because β is a small angle value
The cosine of the angle is equal to one and the sine of the angle is equal to the same angle. In this case angle β which is the rotation angle.

Cos β → 1
Sin β → β

Replacing these values into the last expression for X is obtained:

$$\Delta X_3 = \Delta X_1 - (X_3 - X_1) + r_1\cos\delta - r_1\sin\delta(\beta)$$

$$\Delta X_3 = \Delta X_1 - (X_3 - X_1) + r_1\cos\delta - r_1\sin\delta(RotZ)$$

It is shown that the last expression contains some constant values. Those expressions can be replaced by the constants C_1 and C_2.

$$C_1 = X_3 - X_1 + r_1\cos\delta$$

$$C_2 = r_1 \sin\delta$$

$$\Delta X_3 = \Delta X_1 + C_1 - C_2(RotZ_3)$$

Similar procedure is done for the Y coordinate.

$$\Delta Y_3 = \Delta Y_1 - (Y_3 - Y_1) + r_1 \sin(\delta + \beta)$$

Expand:

$$\Delta Y_3 = \Delta Y_1 - (Y_3 - Y_1) + r_1(\sin\delta\cos\beta + \cos\delta\sin\beta)$$

β is treated as small angle value.

$$\Delta Y_3 = \Delta Y_1 - (Y_3 - Y_1) + r_1 \sin\delta + r_1 \cos\delta\beta$$

$$\Delta Y_3 = \Delta Y_1 - (Y_3 - Y_1) + r_1 \sin\delta + r_1 \cos\delta RotZ_3$$

$$C_3 = Y_3 - Y_1 + r_1 \sin\delta$$

$$C_4 = r_1 \cos\delta$$

$$\Delta Y_3 = \Delta Y_1 - C_3 + C_4 RotZ_3$$

The ultimate position of the point 3 in X and Y direction is:

$$\Delta X_3 = \Delta X_1 + C_1 - C_2 RotZ_3$$

$$\Delta Y_3 = \Delta Y_1 - C_3 + C_4 RotZ_3$$

To represent the motion of the point of a rigid body is necessary to have three equations that represent the three degrees of freedom. Therefore one equation is add to this set and this equation represent the rotation of two point of a rigid body.

$$RotZ_3 = RotZ_1$$

Appendix 4

Constraint Equations in Three dimensions with Rotations

The sequence of rotation is a new factor to be tested to find small angles range for the case of CE in three dimensions. The method used is an analysis with the three studied points from the plane. The rotation matrix is obtained from different combinations of rotations. The XYZ convention is considered the reference of comparison. The figures below show the final position of the same analyzed point anteriorly in X, Y and Z coordinate. The results are shown in the following figures, but only those show the results up to 4 degrees in order to visualize more the tendency of the rotation sequences. The error analysis calculated the maximum value among the combinations up to 10 degrees in increments is in the order of 2.6% for the Y-Z-X sequence of rotation.

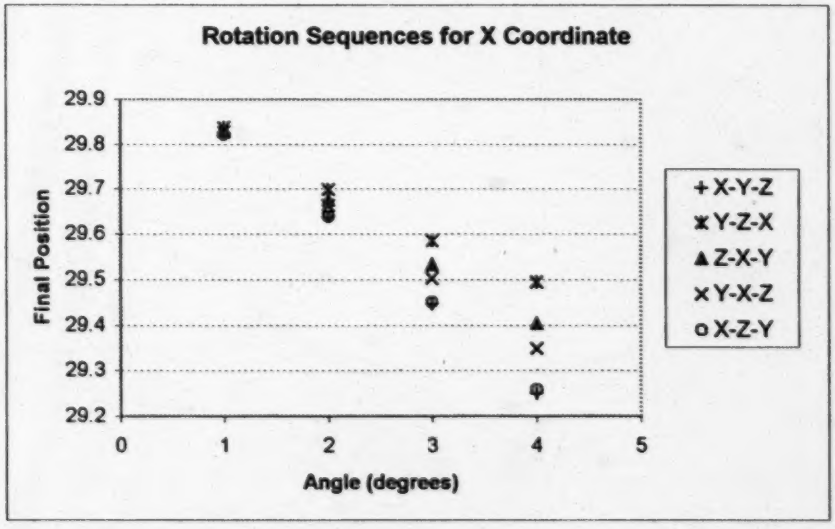

Figure 4-1 Rotation sequences for X Coordinate

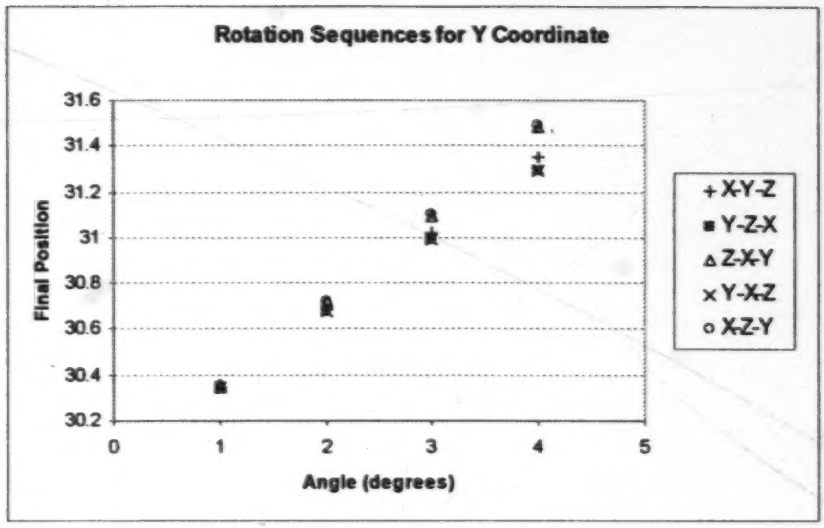

Figure 4-2 Rotation Sequences for Y Coordinate

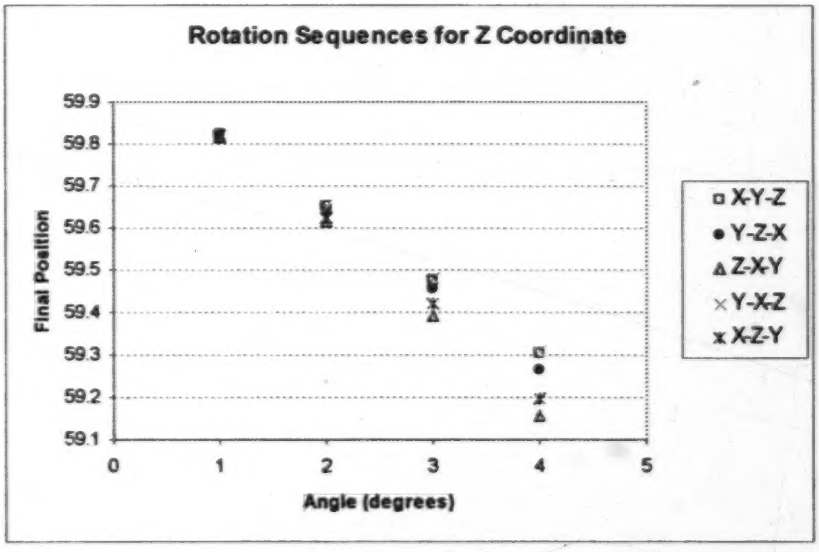

Figure 4-3 Rotation Sequences for Z Coordinate

The results showed that the different sequences to form the rotation matrix with small angles do not vary in great amount as it is shown in the figure above. Therefore the 10 degrees are still working well to define small angles.

Finally one more test is done to the Euler matrix to find the small angle range. The method consisted of comparing the results from the simplified Euler matrix with the Euler matrix with out any manipulation. The simplified Euler matrix assumed small angles, therefore the cosine of the angle is equal to one and sine of the angle is equal to the same angle. The results show the range of rotation angles among 1 and 4 degrees. An error of 8.76% exists when the angle is 4 degrees. Figures 4-4 and 4-5 show the results of the analyzed point in each coordinate.

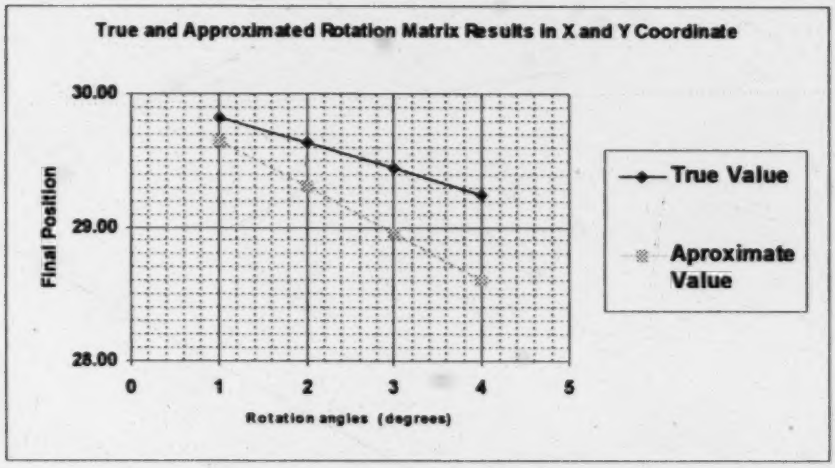

Figure 4-4 True and Approximate Rotation Matrix Results for X and Y Coordinate

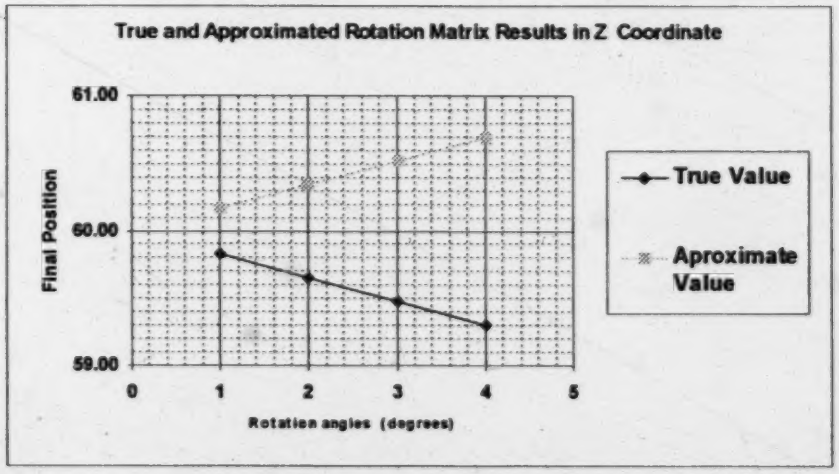

Figure 4-5 True and Approximate Rotation Matrix Results for Z Coordinate

Using the rotation matrix from Euler with XYZ convention

$$\begin{bmatrix} \cos\theta\cos\phi & \cos\theta\sin\phi & -\sin\theta \\ \sin\varphi\sin\theta\cos\phi - \cos\varphi\sin\phi & \sin\varphi\sin\theta\sin\phi + \cos\varphi\cos\phi & \cos\theta\sin\varphi \\ \cos\varphi\sin\theta\cos\phi + \sin\varphi\sin\phi & \cos\varphi\sin\theta\sin\phi - \sin\varphi\cos\phi & \cos\theta\cos\varphi \end{bmatrix} = [R]$$

The motion of a rigid body is given by the following expression:

$$\Delta U_2 = [R]\begin{Bmatrix} \Delta X \\ \Delta Y \\ \Delta Z \end{Bmatrix} + \begin{Bmatrix} UX_1 \\ UY_1 \\ UZ_1 \end{Bmatrix}$$

ΔU_2 = Rotation + Displacement Matrix

As mentioned before, the small angles are used to simplify the expressions that contain sine and cosine.

$\cos\theta \rightarrow 1$	$\sin\theta \rightarrow \theta$
$\cos\varphi \rightarrow 1$	$\sin\varphi \rightarrow \varphi$
$\cos\Phi \rightarrow 1$	$\sin\Phi \rightarrow \Phi$

The rotation matrix with the simplifications given by the use of small angles is transform into:

$$\begin{bmatrix} 1 & \phi & -\theta \\ \varphi\theta - \phi & \varphi\theta\phi + 1 & \varphi \\ \theta + \varphi\phi & \theta\phi - \varphi & -1 \end{bmatrix}$$ The product between the small angles → zero

$$\begin{bmatrix} 1 & \phi & -\theta \\ -\phi & 1 & \varphi \\ \theta & -\varphi & -1 \end{bmatrix}$$

Replacing the new simplified rotation matrix into the initial expression that gives the motion of a rigid body:

$$\Delta U_2 = \begin{bmatrix} 1 & \phi & -\theta \\ -\phi & 1 & \varphi \\ \theta & -\varphi & -1 \end{bmatrix} \cdot \begin{Bmatrix} \Delta X \\ \Delta Y \\ \Delta Z \end{Bmatrix} + \begin{Bmatrix} UX_1 \\ UY_1 \\ UZ_1 \end{Bmatrix}$$

The following angles represent:

θ → Rotation about Y axis → Rot Y_1

φ → Rotation about X axis → Rot X_1

Φ → Rotation about Z axis → Rot Z_1

The new terms are replaced in the last matrix equation:

$$\Delta U_2 = \begin{bmatrix} 1 & RotZ_1 & -RotY_1 \\ -RotZ_1 & 1 & RotX_1 \\ RotY_1 & -RotX_1 & -1 \end{bmatrix} \begin{Bmatrix} \Delta X \\ \Delta Y \\ \Delta Z \end{Bmatrix} + \begin{Bmatrix} UX_1 \\ UY_1 \\ UZ_1 \end{Bmatrix}$$

$$\Delta U_2 = \begin{bmatrix} \Delta X + \Delta Y RotZ_1 - \Delta Z RotY_1 \\ -\Delta X RotZ_1 + \Delta Y + \Delta Z RotX_1 \\ \Delta X RotY_1 - \Delta Y RotX_1 + \Delta Z \end{bmatrix} + \begin{Bmatrix} UX_1 \\ UY_1 \\ UZ_1 \end{Bmatrix}$$

$$\Delta U_2 = \begin{bmatrix} \Delta X + \Delta Y RotZ_1 - \Delta Z RotY_1 + UX_1 \\ -\Delta X RotZ_1 + \Delta Y + \Delta Z RotX_1 + UY_1 \\ \Delta X RotY_1 - \Delta Y RotX_1 + \Delta Z + UZ_1 \end{bmatrix}$$

ΔX, ΔY and ΔZ is the distance between the points of the rigid body (local coordinates)

Expanding the resultant matrix it is obtained:

$$\Delta UX_2 - UX_1 - \Delta Y RotZ_1 + \Delta Z RotY_1 - \Delta X = 0$$

$$\Delta UY_2 - UY_1 + \Delta X RotZ_1 - \Delta Z RotX_1 - \Delta Y = 0$$

$$\Delta UZ_2 - UZ_1 - \Delta X RotY_1 + \Delta Y RotX_1 - \Delta Z = 0$$

The displacement of the point 2 ΔU_2 is also equal to:

$$\Delta U_2 = \begin{Bmatrix} \Delta X + UX_2 \\ \Delta Y + UY_2 \\ \Delta Z + UZ_2 \end{Bmatrix}$$

Equating the last expression with the three equations in the previous page, the resultant equations are:

$$UX_2 - UX_1 - \Delta Y RotZ_1 + \Delta Z RotY_1 = 0$$

$$UY_2 - UY_1 + \Delta X RotZ_1 - \Delta Z RotX_1 = 0$$

$$UZ_2 - UZ_1 - \Delta X RotY_1 + \Delta Y RotX_1 = 0$$

But the degrees of freedom in three dimensions are 6 at each point of the rigid body. Therefore three more equations are added to the last set, representing the rotations between two points of the rigid body.

$$RotX_1 = RotX_2$$

$$RotY_1 = RotY_2$$

$$RotZ_1 = RotZ_2$$

Appendix 5

Constraint Equations in Two dimensions with no rotations

Using the rotation and displacement matrices from the motion of a rigid body

$$\Delta U_2 = \begin{bmatrix} \cos\theta & -\sin\theta \\ \sin\theta & \cos\theta \end{bmatrix} \begin{Bmatrix} \Delta X \\ \Delta Y \end{Bmatrix} + \begin{Bmatrix} Udx_1 \\ Udy_1 \end{Bmatrix}$$

$$A = Ux_2 - Ux_1$$

$$B = Uy_2 - Uy_1$$

$$\sin\theta = \frac{B}{\ell} = \frac{Uy_2 - Uy_1}{\ell}$$

$$\cos\theta = \frac{A}{\ell} = \frac{Ux_2 - Ux_1}{\ell}$$

Since no rotations must be involved in the equations, sine and cosine are replaced by the geometry of the points in the following figure.

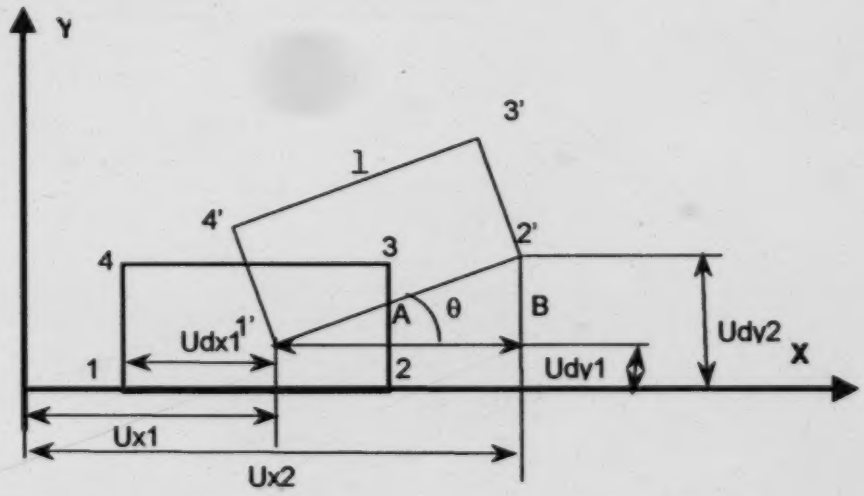

The following steps consist of multiplications of the terms of the transformation matrix with the displacements.

$$\Delta U_2 = \frac{1}{\ell}\begin{bmatrix} Ux_2 - Ux_1 & -(Uy_2 - Uy_1) \\ Uy_2 - Uy_1 & Ux_2 - Ux_1 \end{bmatrix}\begin{Bmatrix} \Delta X \\ \Delta Y \end{Bmatrix} + \begin{Bmatrix} Udx_1 \\ Udy_1 \end{Bmatrix}$$

$$\Delta U_2 = \frac{1}{\ell}\begin{bmatrix} Ux_2 - Ux_1 & -Uy_2 + Uy_1 \\ Uy_2 - Uy_1 & Ux_2 - Ux_1 \end{bmatrix}\begin{Bmatrix} \Delta X \\ \Delta Y \end{Bmatrix} + \begin{Bmatrix} Udx_1 \\ Udy_1 \end{Bmatrix}$$

$$\Delta U_2 = \frac{1}{\ell}\begin{bmatrix} (Ux_2 - Ux_1)\Delta X + (-Uy_2 + Uy_1)\Delta Y \\ (Uy_2 - Uy_1)\Delta X + (Ux_2 - Ux_1)\Delta Y \end{bmatrix}\begin{Bmatrix} \Delta X \\ \Delta Y \end{Bmatrix} + \begin{Bmatrix} Udx_1 \\ Udy_1 \end{Bmatrix}$$

$$\Delta U_2 = \frac{1}{\ell}\begin{bmatrix} Ux_2\Delta X - Ux_1\Delta X - Uy_2\Delta Y + Uy_1\Delta Y \\ Uy_2\Delta X - Uy_1\Delta X + Ux_2\Delta Y - Ux_1\Delta Y \end{bmatrix} + \begin{Bmatrix} Udx_1 \\ Udy_1 \end{Bmatrix}$$

$$\Delta U_2 = \frac{1}{\ell}\begin{bmatrix} Ux_2\Delta X - Ux_1\Delta X - Uy_2\Delta Y + Uy_1\Delta Y \\ Uy_2\Delta X - Uy_1\Delta X + Ux_2\Delta Y - Ux_1\Delta Y \end{bmatrix} + \begin{Bmatrix} Udx_1 \\ Udy_1 \end{Bmatrix}$$

$$\Delta U_2 = \begin{bmatrix} Ux_2\left(\frac{\Delta X}{\ell}\right) - Ux_1\left(\frac{\Delta X}{\ell}\right) - Uy_2\left(\frac{\Delta Y}{\ell}\right) + Uy_1\left(\frac{\Delta Y}{\ell}\right) + Udx_1 \\ Uy_2\left(\frac{\Delta X}{\ell}\right) - Uy_1\left(\frac{\Delta X}{\ell}\right) + Ux_2\left(\frac{\Delta Y}{\ell}\right) - Ux_1\left(\frac{\Delta Y}{\ell}\right) + Udy_1 \end{bmatrix}$$

The final equations that relate the displacement and rotation of two points of the rigid body are:

$$\Delta Ux_2 = Ux_2\left(\frac{\Delta X}{\ell}\right) - Ux_1\left(\frac{\Delta X}{\ell}\right) - Uy_2\left(\frac{\Delta Y}{\ell}\right) + Uy_1\left(\frac{\Delta Y}{\ell}\right) + Udx_1$$

$$\Delta Uy_2 = Uy_2\left(\frac{\Delta X}{\ell}\right) - Uy_1\left(\frac{\Delta X}{\ell}\right) + Ux_2\left(\frac{\Delta Y}{\ell}\right) - Ux_1\left(\frac{\Delta Y}{\ell}\right) + Udy_1$$

Appendix 6

Physical Functional Unit Displacements

Load (N)	Disp. Specimen1 (mm)	Disp. Specimen 2 (mm)	Disp. Specimen 3 (mm)
1.96	0.190	0.127	0.221
2.94	0.304	0.228	0.342
3.92	0.419	0.304	0.451
4.9	0.495	0.364	0.589
5.88	0.609	0.4408	0.693
6.86	0.711	0.508	0.806
7.84	0.800	0.576	0.933
8.82	0.889	0.654	1.097
9.8	0.965	0.712	1.240

Table 6.1 Experimental results from the physical functional unit

Appendix 7

Coordinate Measuring System Specifications

PERFORMANCE

Accuracies [@68°F ±2°F]			
Linear Accuracy (B89 – Bandwidth)		0.006mm	0.00024"
Repeatability (B89 – Bandwidth)		0.004mm	0.00015"
Resolution		0.002mm	0.00010"
Display Range		± xxxx.xxx	±xxx.xxxx

DIMENSIONS

Measuring Range	X-Axis	356mm	14.00"
	Y-Axis	406mm	16.00"
	Z-Axis	305mm	12.00"
Work Capacity	X-Axis	457mm	18.00"
	Y-Axis	610mm	24.00"
	Z-Axis	381mm	15.00"
Overall Dimensions	Length (X)	743mm	29.25"
	Width (Y)	730mm	28.75"
	Height (Z)	1340mm	52.75"
Weights	Machine Only	149 kg	330 lbs
	Complete System	168 kg	370 lbs
	Shipping	220 kg	485 lbs
	Max. Part Weight	68 kg	150 lbs

OPERATIONAL REQUIREMENTS

Operating Temperature Range		10-40°C	50-104°F
Minimum Air Input		70 PSI	
Air Consumption		3.5 SCFM	
Regulator Setting		55 PSI	
Power		110/220 VAC, 50/60 Hz	
Power Consumption	Electronics	60 Watts	
	CRT Display	26 Watts	

From Coordinate Measuring System Manual, 1986

Appendix 8

Physical Model Results

The following drawing presents the numbering that is used in the physical model.

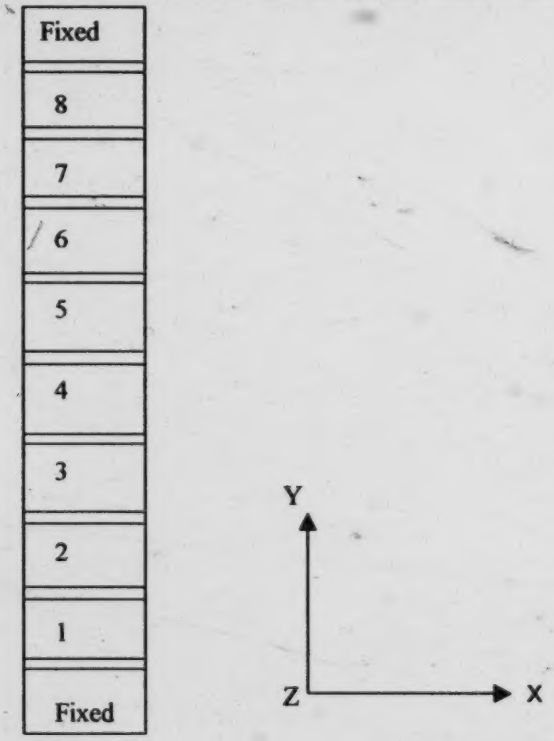

The following tables contain the results from the different loading conditions with the maximum load apply to the physical model for each case.

Type of load	Force (N)	# Block	X (Left)	Y (Left)	X (Right)	Y (Right)
Horizontal to the blocks 7 and 3	18.62	1	1.013	0.371	0.991	-0.434
		2	2.432	0.328	2.425	-0.473
		3	3.337	-0.01	3.336	-0.084
		5	1.388	-0.542	1.375	0.47
		6	-0.061	-0.402	-0.067	0.416
		7	-0.997	-0.122	-1.009	0.079
		8	-0.571	0.124	-0.585	-0.184

Table 8.1 Horizontal Forces in block 7 and 3 of the Physical Model

Type of load	Force (N)	# Block	X (Left)	Y (Left)	X (Right)	Y (Right)
Horizontal Left force at block 7	19.6	1	-0.372	-0.225	-0.389	0.202
		2	-1.182	-0.325	-1.172	0.292
		3	-2.147	-0.369	-2.133	0.334
		5	-3.731	-0.208	-3.743	0.123
		6	-3.848	0.213	-3.877	-0.041
		7	-3.184	0.473	-3.253	-0.421
		8	-1.280	0.455	-1.351	-0.629

Table 8.2 Horizontal Force in block 7 of the Physical Model

Type of load	Force (N)	# Block	X (Left)	Y (Left)	X (Right)	Y (Right)
Horizontal Right force at block 3	19.6	1	1.450	0.594	1.416	-0.631
		2	3.714	0.610	3.6884	-0.796
		3	5.629	0.226	5.621	-0.439
		5	4.864	-0.456	4.862	0.372
		6	3.487	-0.566	3.476	0.522
		7	1.894	-0.565	1.880	0.481
		8	0.580	-0.303	0.577	0.294

Table 8.3 Horizontal Force in block 3 of the Physical Model

Type of load	Force (N)	# Block	X (Left)	Y (Left)	X (Right)	Y (Right)
Horizontal Right force at block 4	18.62	1	1.305	0.602	1.290	-0.591
		2	3.558	0.747	3.507	-0.842
		4	7.142	0.112	7.157	-0.201
		5	6.475	-0.276	6.451	0.440
		6	4.797	-0.666	4.757	0.707
		7	2.742	-0.747	2.692	0.672
		8	0.859	-0.458	0.849	0.415

Table 8.4 Horizontal Force in block 4 of the Physical Model

Type of load	Force (N)	# Block	X (Left)	Y (Left)	X (Right)	Y (Right)
Horizontal Right force at block 4 and angle force of 5 degrees at block 7	19.6	1	1.008	0.498	0.993	-0.425
		2	2.719	0.604	2.686	-0.551
		4	5.247	0.079	5.243	-0.017
		5	4.412	-0.260	4.415	0.52
		6	2.957	-0.369	2.956	0.607
		7	1.597	-0.107	1.590	0.444
		8	0.590	-0.187	0.590	0.345

Table 8.5 Horizontal Force in block 4 and angle force at block 7 of the Physical Model

Type of load	Force (N)	# Block	X (Left)	Y (Left)	X (Right)	Y (Right)
Angle force of 4 degrees at block 7	19.6	1	0.203	0.026	0.193	-0.147
		2	0.543	0.040	0.560	-0.203
		3	0.920	0.033	0.934	-0.191
		5	1.304	-0.187	1.311	-0.120
		6	1.113	-0.300	1.118	0.016
		7	0.519	-0.314	0.518	0.311
		8	0.046	-0.146	0.040	0.012

Table 8.6 Angle Force of 4 degrees at block 7 of the Physical Model

Type of load	Force (N)	# Block	X (Left)	Y (Left)	X (Right)	Y (Right)
Moment at block 3	18.62	1	-0.039	0.044	-0.039	-0.073
		2	0.254	0.213	0.259	-0.227
		3	1.147	0.519	1.120	-0.510
		5	2.035	-0.015	2.051	0.087
		6	1.612	-0.193	1.601	0.219
		7	0.944	-0.212	0.932	0.246
		8	0.303	-0.133	0.301	0.178

Table 8.7 Moment at block 3 of the Physical Model

Type of load	Force (N)	# Block	X (Left)	Y (Left)	X (Right)	Y (Right)
Moment at block 7	18.62	1	0.332	0.201	0.335	-0.158
		2	0.986	0.264	1.002	-0.241
		3	1.777	0.238	1.771	-0.25
		5	2.62	-0.037	2.681	0.015
		6	2.412	-0.271	2.404	0.246
		7	1.333	-0.647	1.284	0.602
		8	0.238	-0.247	0.231	0.240

Table 8.8 Moment at block 7 of the Physical Model

Type of load	Force (N)	# Block	X (Left)	Y (Left)	X (Right)	Y (Right)
Moment at block 7	18.62	1	-0.314	-0.247	-0.322	0.033
		2	-0.816	-0.301	-0.793	-0.018
		3	-1.081	-0.223	-1.119	-0.137
		5	-2.209	-0.355	-2.227	0.042
		6	-2.629	-0.042	-2.640	-0.014
		7	-2.369	0.370	-2.414	-0.142
		8	-1.033	0.300	-1.078	-0.506

Table 8.9 Vertical angle of 4 degrees at block 3 and Horizontal force at block 7 of the Physical Model

Appendix 9

Computational Physical Functional Unit Results

Load (N)	Disp. Specimen1 (mm)	Disp. Specimen 2 (mm)	Disp. Specimen 3 (mm)
1.96	0.202	0.141	0.236
2.94	0.303	0.210	0.354
3.92	0.404	0.283	0.472
4.9	0.505	0.352	0.59
5.88	0.606	0.420	0.708
6.86	0.707	0.491	0.826
7.84	0.808	0.564	0.944
8.82	0.909	0.630	1.062
9.8	1.01	0.700	1.180

Table 9.1 Computational results from the physical functional unit

Appendix 10

Computational Results of Physical Model

Type of load	Force (N)	# Block	X (Left)	Y (Left)	X (Right)	Y (Right)
Horizontal to the blocks 7 and 3	18.62	1	0.899	0.313	0.893	-0.313
		2	2.251	0.323	2.251	-0.323
		3	3.239	0.045	3.239	-0.0456
		5	1.311	-0.418	1.311	0.418
		6	-0.082	-0.361	0.0826	0.361
		7	-1.045	-0.104	-1.045	0.110
		8	-0.589	0.093	-0.589	-0.093

Table 10.1 Horizontal Forces in block 7 and 3 of the Computational Model

Type of load	Force (N)	# Block	X (Left)	Y (Left)	X (Right)	Y (Right)
Horizontal Left force at block 7	19.6	1	-0.328	-0.160	-0.328	0.160
		2	-1.004	-0.252	-1.004	0.252
		3	-1.836	-0.274	-1.836	0.274
		5	-3.200	-0.112	-3.214	0.112
		6	-3.36	0.072	-3.378	-0.072
		7	-2.938	0.326	-2.926	-0.326
		8	-1.244	0.388	-1.244	-0.388

Table 10.2 Horizontal Force in block 7 of the Computational Model

Type of load	Force (N)	# Block	X (Left)	Y (Left)	X (Right)	Y (Right)
Horizontal Right force at block 3	19.6	1	1.291	0.490	1.276	-0.490
		2	3.360	0.598	3.378	-0.598
		3	5.243	0.324	5.241	-0.324
		5	4.581	-0.334	4.580	0.334
		6	3.280	-0.458	3.290	0.458
		7	1.830	-0.442	1.836	0.442
		8	0.614	-0.290	0.614	0.29

Table 10.3 Horizontal Force in block 3 of the Computational Model

Type of load	Force (N)	# Block	X (Left)	Y (Left)	X (Right)	Y (Right)
Horizontal Right force at block 4	18.62	1	1.144	0.486	1.144	-0.486
		2	3.214	0.672	3.214	-0.673
		4	6.796	0.133	6.796	-0.132
		5	6.180	-0.330	6.180	0.330
		6	4.580	-0.574	4.596	0.574
		7	2.62	-0.602	2.636	0.602
		8	0.904	-0.410	0.904	0.410

Table 10.4 Horizontal Force in block 4 of the Computational Model

Type of load	Force (N)	# Block	X (Left)	Y (Left)	X (Right)	Y (Right)
Horizontal Right force at block 4 and angle force of 5 degrees at block 7	19.6	1	1.018	0.442	1.018	-0.419
		2	2.853	0.613	2.85	-0.57
		4	5.971	0.136	5.971	-0.0513
		5	5.321	-0.260	5.320	0.366
		6	3.853	-0.437	3.838	0.562
		7	2.179	-0.387	2.179	0.535
		8	0.771	-0.294	0.771	0.368

Table 10.5 Horizontal Force in block 4 and angle force at block 7 of the Computational Model

Type of load	Force (N)	# Block	X (Left)	Y (Left)	X (Right)	Y (Right)
Angle force of 4 degrees at block 7	19.6	1	0.044	0.009	0.044	-0.031
		2	0.130	0.007	0.131	-0.05
		3	0.220	-0.005	0.226	-0.061
		5	0.330	-0.064	0.330	-0.047
		6	0.276	-0.110	0.330	0.234
		7	0.112	-0.166	0.276	0.011
		8	-0048	-0.068	0.112	-0.008

Table 10.6 Angle Force of 4 degrees at block 7 of the Computational Model

Type of load	Force (N)	# Block	X (Left)	Y (Left)	X (Right)	Y (Right)
Moment at block 3	18.62	1	-0.003	0.031	-0.003	-0.031
		2	0.117	0.091	0.117	-0.091
		3	0.448	0.183	0.448	-0.182
		5	0.756	-0.013	0.756	0.014
		6	0.598	-0.060	0.598	0.060
		7	0.359	-0.074	0.359	0.074
		8	0.127	-0.053	0.127	0.054

Table 10.7 Moment at block 3 of the Computational Model

Type of load	Force (N)	# Block	X (Left)	Y (Left)	X (Right)	Y (Right)
Moment at block 7	18.62	1	0.114	0.051	0.114	-0.052
		2	0.336	0.077	0.336	-0.077
		3	0.590	0.076	0.590	-0.076
		5	0.906	-0.006	0.906	0.0062
		6	0.818	-0.088	0.818	0.088
		7	0.467	-0.197	0.467	0.197
		8	0.098	-0.091	0.098	0.089

Table 10.8 Moment at block 7 of the Computational Model

Type of load	Force (N)	# Block	X (Left)	Y (Left)	X (Right)	Y (Right)
Moment at block 7	18.62	1	-0.275	-0.153	-0.277	0.091
		2	-0.796	-0.239	-0.796	0.112
		3	-1.368	-0.254	-1.368	0.065
		5	-2.527	-0.186	-2.542	0.058
		6	-2.813	-0.022	-2.813	-0.072
		7	-2.557	0.228	-2.557	-0.290
		8	-1.100	0.317	-1.098	-0.349

Table 10.9 Vertical angle of 4 degrees at block 3 and Horizontal force at block 7 of the Computational Model